Gondwana Research 109 (2022) 460–492

Contents lists available at ScienceDirect

Gondwana Research

journal homepage: www.elsevier.com/locate/gr

GR Focus Review

The North Sistan orogen (Eastern Iran): Tectono-metamorphic evolution and significance within the Tethyan realm

Michael Jentzer [a,*], Philippe Agard [a], Guillaume Bonnet [a], Patrick Monié [b], Marc Fournier [a], Hubert Whitechurch [c], Jafar Omrani [d], Mohammad Hossein Zarrinkoub [e], Mohammad Mahdi Khatib [e], Reza Kohansal [d], Damien Do Couto [a], Camille Godbillot [a], Dia Ninkabou [a]

[a] Sorbonne Université, CNRS, Institut des Sciences de la Terre de Paris (iSTeP), 4 Place Jussieu, 75005 Paris, France
[b] Université de Montpellier, CNRS, Université des Antilles, Montpellier, France
[c] Université de Strasbourg, Ecole et Observatoire des Sciences de la Terre, Institut de Physique du Globe, Institut de Géologie, 1 rue Blessig, 67084 Strasbourg, France
[d] Geological Survey of Iran, Mehraj Bd., Tehran, Iran
[e] Department of Geology, University of Birjand, University Bd., Birjand, Southern Khorasan, Iran

ARTICLE INFO

Article history:
Received 23 March 2021
Revised 25 March 2022
Accepted 4 April 2022
Available online 26 April 2022
Handling Editor: R.D. Nance

Keywords:
Sistan orogen
Geodynamics
Ophiolite
Obduction
Metamorphic sole
Pull-apart ocean
Iran

ABSTRACT

The Sistan orogen (Eastern Iran) separates the Afghan and Lut continental blocks and stretches along ~700 km from north to south, at a high angle with respect to other, dominantly E-W trending Alpine-Himalayan orogens. This study reappraises the tectono-metamorphic evolution of the northern part of the orogen, as well as its significance within the Neotethyan realm. Detailed inspection of the Sistan ophiolite indicates that the Sistan Ocean was of a slow-spreading type and that, given its structural patterns, petrological characteristics and age, it opened in a transtensional setting ~125 Ma ago. Closure of the Sistan Ocean took place through a major NE-dipping subduction zone, formed no later than 90 Ma, as shown by the location and age of bimodal juvenile arc magmatism, the SW vergence of the orogen and the location and age of subducted fragments. The discovery of a metamorphic sole at the base of the ophiolite (~750 °C–0.65 GPa) argues for the onset of an additional intra-oceanic thrust/subduction zone around 74–72 Ma, which resulted in the south-westward obduction and preservation of the ophiolite onto the continental Lut block. The Sistan Ocean therefore appears to have recorded two major geodynamic events that accompanied the closure of the Neotethys, i.e. the major change in kinematics at ~105 ± 5 Ma and the northward migration of India from ~75 to 70 Ma onwards. Subsequent collision, likely started during the Paleocene and mostly completed by the Oligocene, was accompanied by a drastic change of the Eocene sedimentation yet by only moderate shortening (~30–50 km in total). Since the Late Miocene onwards, post-collisional deformation is dominated by far-field stresses related to the Zagros collision.
© 2022 International Association for Gondwana Research. Published by Elsevier B.V. All rights reserved.

Contents

1. Introduction . . . 461
2. Sistan orogeny: State of the art and major unknowns. . . . 462
   2.1. Overall structure . . . 462
   2.2. Overview of the main tectonic events since the Mesozoic . . . 464
3. Reappraisal of the North Sistan structural organization and major rock types . . . 465
   3.1. New tectonic map for the northern Sistan orogen . . . 465
   3.2. Sedimentary features . . . 466
   3.3. Ophiolitic rocks . . . 466
   3.4. Metamorphic rocks from the Neh Complex and the Lut Block. . . . 469
4. Sections across the northern branch of the Sistan orogen. . . . 474
   4.1. Sections across the HP-LT zone . . . 475
   4.2. Sections across the Neh Complex. . . . 475

* Corresponding author.
E-mail address: michael.jentzer@sorbonne-universite.fr (M. Jentzer).

https://doi.org/10.1016/j.gr.2022.04.004
1342-937X/© 2022 International Association for Gondwana Research. Published by Elsevier B.V. All rights reserved.

5. P-T-t estimates in the western part of the north Sistan orogen . . . 475
5.1. Neh ophiolite and associated sediments . . . 475
5.2. Metamorphic rocks of the Neh Complex . . . 477
5.3. Metamorphic rocks of the Lut Block . . . 477
6. Discussion . . . 478
6.1. Overall structure of the northern Sistan orogen . . . 478
6.2. Geodynamic significance of metamorphic rocks . . . 478
6.2.1. Neh Complex: Evidence for metamorphic sole formation and intra-oceanic slicing during the onset of obduction . . . 478
6.2.2. Lut Block: Contact metamorphism and regional metamorphism . . . 479
6.3. Tectonic evolution of the northern Sistan orogen . . . 481
6.4. Tectonic significance of the Sistan orogen within the Neotethyan realm . . . 484
7. Conclusions . . . 484
Declaration of Competing Interest . . . 485
Acknowledgements . . . 485
Appendix A. Logs of the Sefidabeh basin and the Neh Complex . . . 485
Appendix B. Analytical methods . . . 485
B.1. Mineral chemistry . . . 485
B.2. RAMAN spectroscopy and mineral determination . . . 485
B.3. Thermometric methods used . . . 485
B.3.1. Raman spectroscopy on carbonaceous material: Tmax estimation . . . 485
B.3.2. Ti in biotite: empirical thermometry . . . 485
B.4. Thermobarometric methods used . . . 486
B.4.1. Plagioclase-amphibole . . . 486
B.4.2. Ti-Al amphiboles . . . 486
B.4.3. GB and GBAQ: empirical thermobarometry . . . 486
B.4.4. Thermodynamic modelling . . . 486
B.5. Geochronology methods . . . 486
B.5.1. Ar-Ar . . . 486
B.5.2. U-Pb in titanite . . . 487
Appendix C. Mineral chemistry . . . 487
C.1. Ophiolitic rocks . . . 487
C.2. Birjand metasediments . . . 487
C.3. Amphibolite . . . 487
C.4. Metamorphic rocks of the Lut Block . . . 487
C.5. Metamorphic rocks of the Lut Block: Deh-Salm Complex . . . 487
Appendix D. Supplementary material . . . 488
References . . . 488

1. Introduction

The long-lived convergence between Laurussia/Laurasia and the continental fragments derived from Gondwana has resulted in the formation of the extensive, mostly E-W trending Alpine–Himalayan mountain belts. Two suture zones, outlined by ophiolite belts, subduction-related high-pressure low-temperature (HP-LT) metamorphic relics, magmatic arcs and flexural basins, mark the former location of two major oceans (Fig. 1). The Paleotethys Ocean, in the north, disappeared through N-dipping subduction below Laurussia, from the Upper Carboniferous onwards, leading to the Late Triassic 'Early-Cimmerian' continental collision (e.g., Dercourt et al., 1986; Stampfli and Borel, 2002; Barrier et al., 2018). The Neotethys Ocean, in the south, formed on the northern edge of Gondwana in the Upper Carboniferous or Early Permian, while the Paleotethys Ocean was still several thousand kilometers wide (Stampfli and Borel, 2002; Torsvik and Cocks, 2017). Closure of the Neotethys started during the lowermost Jurassic through N-dipping subduction below Laurasia (Fig. 1b) and was followed, in Iran, by the Zagros collision from the Eo-Oligocene onwards (e.g., Berberian and Berberian, 1981; Sengor et al., 1988; Agard et al., 2011). However, owing to the discontinuity of tectono-sedimentary markers and the diachronicity of tectonic events along strike (Stampfli and Borel, 2002), many uncertainties still remain on the exact location of each suture or the number of intervening continental domains, particularly the so-called Cimmerian blocks (e.g. Gaina et al., 2015; Mattei et al., 2015). These Cimmerian blocks, well preserved in Iran, Afghanistan and Pakistan, are separated by ophiolite belts branching off the two main E-W Tethyan sutures (Fig. 1a), that are mostly Mesozoic in age and commonly interpreted as former back-arc basins located within the upper plate of the Neotethys subduction system (Agard et al., 2011; Shafai Moghadam and Stern, 2015). Yet, their geodynamic evolution and mutual relationships are still puzzling (e.g., McQuarrie and van Hinsbergen, 2013; Ajirlu et al., 2016; Richards and Sholeh, 2016), and whether the Cimmerian blocks once formed a continuous continental domain is unknown (Fig. 1b; Mattei et al., 2015).

This study focuses on the ~700 km long, north-south trending Sistan orogen separating the Afghan and Lut Cimmerian blocks (Figs. 1a, 2), for which key geological features are still debated: the nature of the vanished ocean, with hypotheses ranging from fast- to ultraslow-spreading (Moazzen et al., 2006; Saccani et al., 2010; Zarrinkoub et al., 2012); the unclear relationships between the Sistan orogen, the main Tethyan sutures and the neighbouring inner ophiolite belts (e.g., Berberian and King, 1981; Saccani et al., 2010; Barrier et al., 2018); the timing of oceanic closure, ranging from the Late Cretaceous to the Oligocene (Tirrul et al., 1983; Arjmandzadeh et al., 2011; Pang et al., 2013); the processes leading to the emplacement and preservation of the easternmost inner ophiolite belt of Iran (Moghadam and Stern, 2015, and references therein); the tectonic style, amount of overall shortening and duration of the collisional process (Tirrul et al., 1983). The present study aims at answering some of these questions through a combination of structural, metamorphic and geochronologic investigations across the northern part of the Sistan orogen.

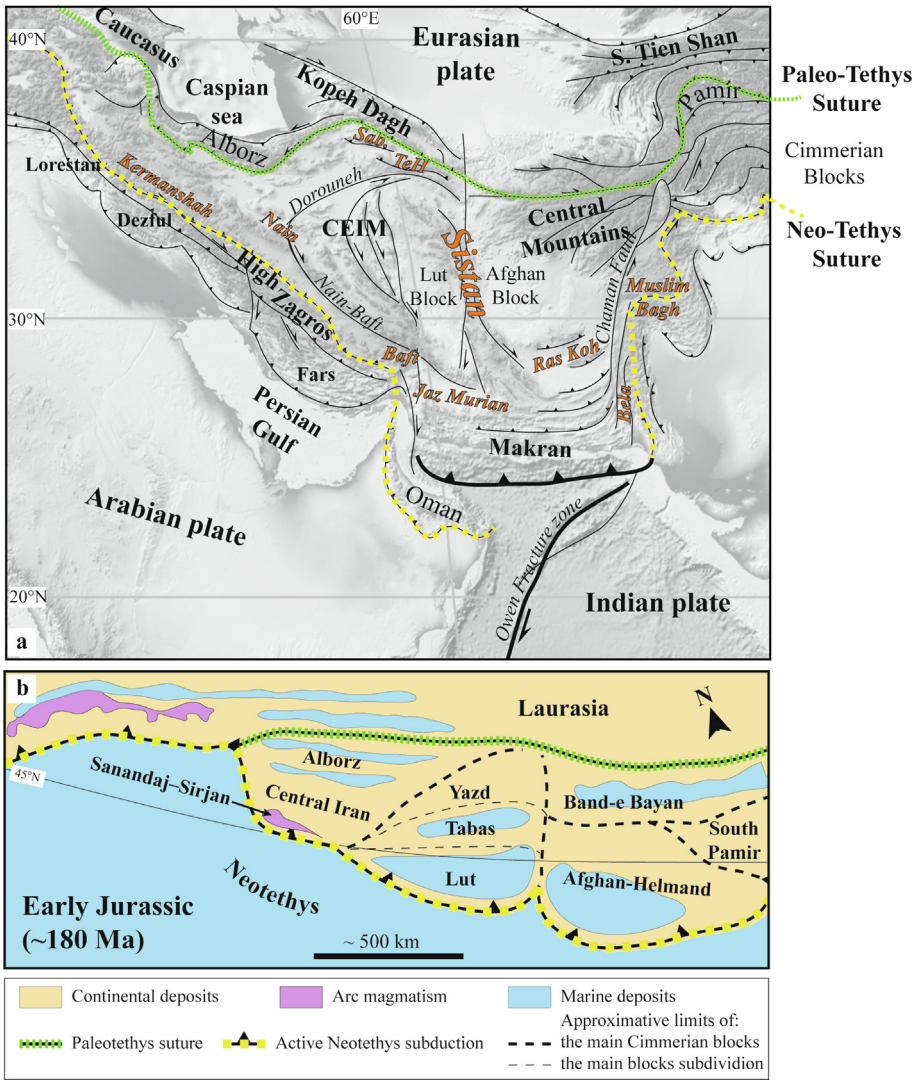

Fig. 1. Geological setting of the Sistan in the Tetyan realm. **a)** Shaded relief map from ETOPO1 (http://www.ngdc.noaa.gov/mgg/global/relief/ETOPO1) centred on the Sistan with the main Paleo- and Neo-Tethyan sutures, the main faults (in *italic*), the orogenic belt (in **bold**) and the main Mesozoic ophiolites (in orange). **b)** Early Jurassic (~180 Ma) paleogeographic reconstruction of the Tethyan realm with the approximative limits of the Cimmerian blocks (modified after Masoodi et al., 2013; Barrier et al., 2018).

2. Sistan orogeny: State of the art and major unknowns

2.1. Overall structure

Tirrul et al. (1983) divided the Sistan belt into five main domains, mostly on the basis of lithostratigraphy (Fig. 2b; Supplementary Figs. 1, 2). The Lut Block to the W and the Afghan Block to the E are characterized by Neoproterozoic to Paleozoic basement rocks. Sediments deposited on top are mildly deformed Jurassic phyllites and Early Cretaceous (Barremian-Aptian) Orbitolina limestones. Between these two continental blocks, three domains form the Sistan Suture Zone proper:

- The Neh Complex is made of an Aptian to Albian weakly metamorphosed ophiolite and/or ophiolitic mélange with radiolarian cherts, marls and/or deep-sea carbonates immediately deposited on top of it or interbedded with ophiolitic pillow basalts. The sedimentary sequence contains Late Cretaceous and Paleocene fine-grained turbidites, interbedded with limestone in places, and then Eocene Red Beds conglomerates. A major angular unconformity marks the limit between the Eocene and Oligo-Miocene conglomerates. Pliocene continental conglomerates rework all previous lithologies. The thickness of the sedimentary sequence reaches ~4 km.
- The Ratuk Complex is characterized by highly deformed ophiolitic material and sediments metamorphosed under HP-LT conditions. These metamorphic units are unconformably overlain by a Maastrichtian conglomerate grading upwards into turbidites. In places, Eocene Red Beds overly unconformably the Maastrichitain sequence. Plio-quaternary polygenic conglomerates terminate the sequence.
- The ~8 km thick fore-arc Sefidabeh Basin, which overlies both the Ratuk and Neh Complexes, starts with Aptian to Senonian calci-turbidites. Coeval magmatic activity is attested by the presence of intrusions and interbedded lava flows. Locally, Maastrichtian sediments comprise a basal polygenic breccia reworking ophiolite pebbles and grading upwards into a fine grained turbiditic sequence interbedded in places with a ten-meter-thick Hyppuritic and Orbitoid bearing limestone. An Early Paleocene reefal limestone, with large thickness variations

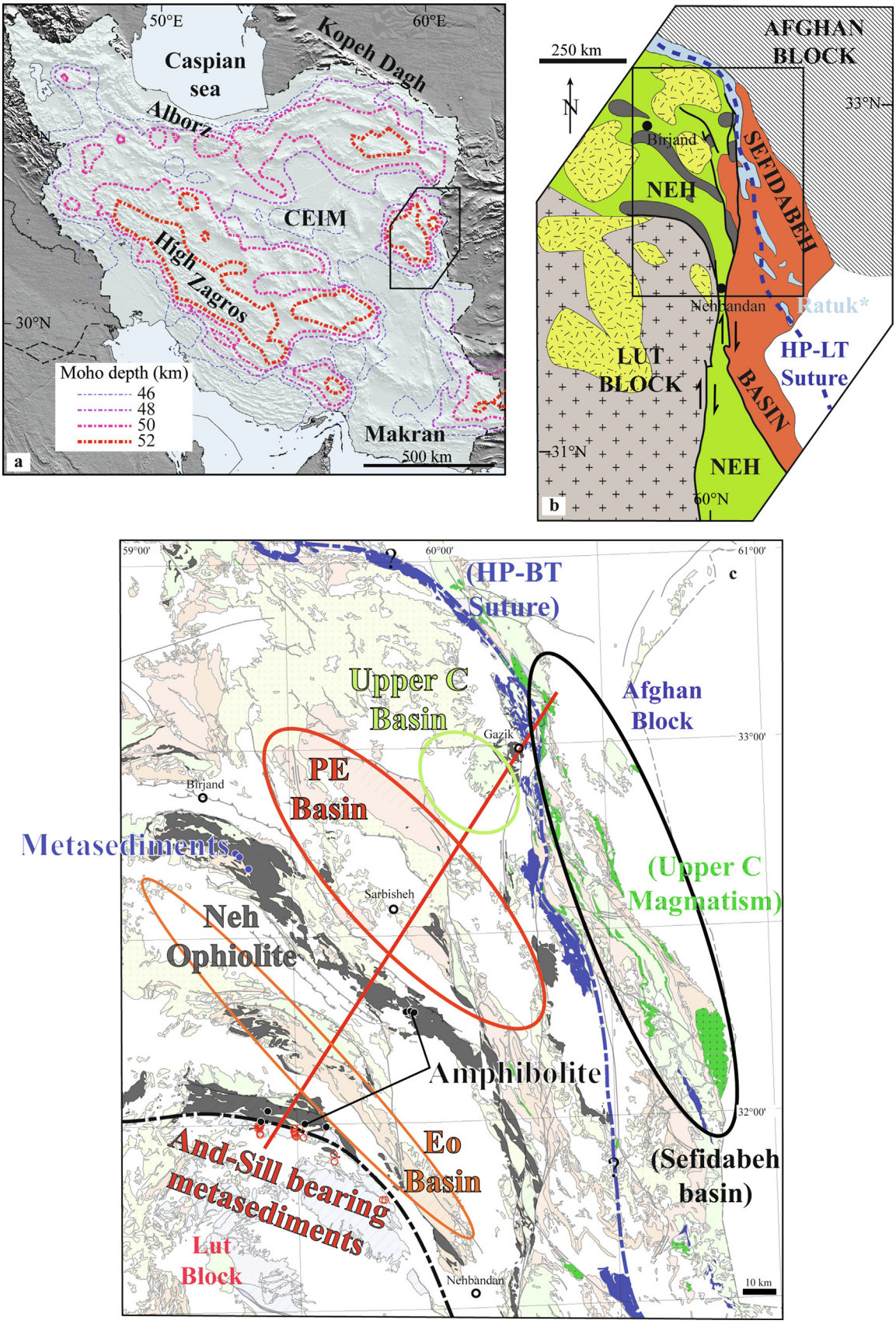

Fig. 2. The Sistan orogen **a)** Elevation map (modified after Paul et al., 2010) with contours of the depth of the Moho in Iran (modified after Mousavi and Ebbing, 2018). **b)** Schematic structure of the North Sistan belt (modified after Tirrul et al., 1983). **c)** Structural map of the North Sistan belt with the targets of this study.

from ~0 to >600 m, unconformably overlies the Late Cretaceous deposits. This formation is in turn overlained by a Late Paleocene channelized turbiditic sequence. The younger, Eocene to Plio-Quaternary sequence resembles that of the Neh Complex.

Gravimetric data suggest that Moho depths reach up to ~52 km below the Sistan mountain belt, hence somewhat deeper than the 40–45 km depth reported for the adjacent Central East Iran Microcontinent (CEIM; i.e. the Yazd, Tabas and Lut blocks in Fig. 2a; Mousavi and Ebbing, 2018; Eshagh et al., 2019). In contrast, heat flow and magnetic data suggest that the lithosphere is relatively thin below Sistan (Davies, 2013; Mousavi and Ebbing, 2018; Lucazeau, 2019). Paleomagnetic data indicate that the CEIM experienced several counter-clockwise rotations through time: ~65° between the Late Triassic and the Middle Jurassic, ~30° between the Late Jurassic and the Late Cretaceous and ~35° since the Miocene (Davoudzadeh et al., 1981; Soffel and Förster, 1984; Soffel et al., 1996; Besse et al., 1998; Mattei et al., 2012, 2015; Fig. 3). Data also suggest that the Yazd, Tabas and Lut blocks have remained close to each other at least since the Mesozoic.

2.2. Overview of the main tectonic events since the Mesozoic

While the timing of rifting is ill-constrained for the Sistan Ocean, ocean spreading is attested during the Aptian-Albian by K-Ar and U-Pb dating of oceanic gabbros, and by the biostratigraphic dating of radiolarites (Delaloye and Desmons, 1980; Babazadeh and De Wever, 2004; Zarrinkoub et al., 2012; Ozsvárt et al., 2020; Fig. 3). The Sistan ophiolitic sequence comprises a variably serpentinised, dominantly harzburgitic mantle section, together with N-MORB gabbros and basalts and rarer E-MORB basalts (Delaloye and Desmons, 1980; Moazzen et al., 2006; Saccani et al., 2010; Zarrinkoub et al., 2012). Contrasting degrees of partial melting of the mantle have been proposed to explain the formation of its crustal section (Moazzen et al., 2006; Saccani et al., 2010; Zarrinkoub et al., 2012). Less common mafic rocks bearing a calc-alkaline affinity have also been taken as evidence for a supra-subduction origin (Saccani et al., 2010). Although Berberian and Berberian (1981) first proposed that the Sistan oceanic basin opened as a back-arc basin above the retreating Zagros subduction zone, its paleogeographic orientation remains largely speculative, ranging from N100 to N160°E (e.g., Saccani et al., 2010; Barrier et al., 2018).

The subduction of the Sistan Ocean beneath the Afghan margin is attested since at least the Turonian by (i) eclogites in the Ratuk Complex, with peak P-T conditions ranging between 1.9–2.4 GPa, 435–650 °C and ages between ca. 89 and ca. 83 Ma (Fotoohi Rad et al., 2005; Angiboust et al., 2013; Bröcker et al., 2013; Kurzawa et al., 2017; Bonnet et al., 2018; Fig. 3); (ii) thick deposits of Senonian deep-sea turbidites representing trench infill in both the Neh Complex and the Sefidabeh Basin (Tirrul et al., 1983; Fig. 3); (iii) low-K calc-alkaline and adakitic magmatic rocks mainly intruding or interbedded with the Sefidabeh Senonian turbidites (Jentzer et al., 2020; Fig. 3).

The onset of collision in the Sistan orogen is loosely defined by the deformation of Eocene deposits, the increase of clastic coarse-grained sediments during Eocene time (Tirrul et al., 1983; Fig. 3) and the existence of mildly deformed, calc-alkaline Paleogene magmatism (ca. 46–25 Ma) into both the Lut Block and the Sistan Suture Zone. This magmatism was ascribed to delamination of the lithosphere following collision (Camp and Griffis, 1982; Pang et al., 2013; Mohammadi et al., 2016; Omidianfar et al., 2020; Fig. 3).

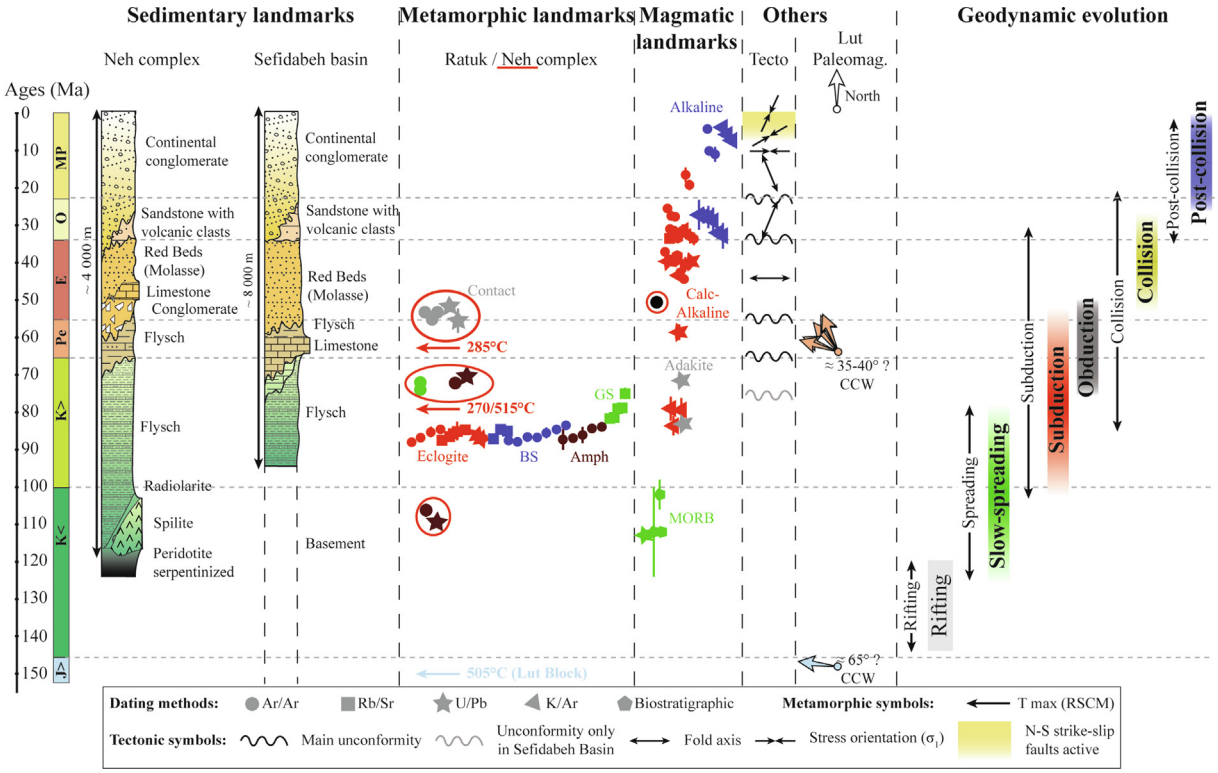

Fig. 3. Review of the main data available for the Sistan Orogen, with new data provided by this study inside circles: synthetic logs modified from Tirrul et al. (1983), metamorphic landmarks from Bonnet et al. (2018 and references therein; Amph: amphibolite facies; BS: blueschist facies; GS: greenschist facies), magmatic landmarks from Jentzer et al. (2020 and references therein), tectonic landmarks from Jentzer et al. (2017 and references therein), paleomagnetic data from Mattei et al. (2015 and references therein; CCW: counterclockwise rotation). Previously assumed geodynamic evolution (black arrows: for rifting stage Babazadeh and De Wever, 2004; for spreading stage Delaloye and Desmons, 1980; Babazadeh and De Wever, 2004; Saccani et al., 2010; and Zarrinkoub et al., 2012; for Subduction stage Tirrul et al., 1983; Fotoohi Rad et al., 2009; Arjmandzadeh et al., 2011; Angiboust et al., 2013; Bröcker et al., 2013; Pang et al., 2013; Kurzawa et al., 2017; Bonnet et al., 2018; and Jentzer et al., 2020; for collision stage Tirrul et al., 1983; Zarrinkoub et al., 2012; Pang et al., 2013; Mohammadi et al., 2016; for post-collision stage Pang et al., 2012; Jentzer et al., 2017) is compared to the one inferred from our data (coloured rectangles).

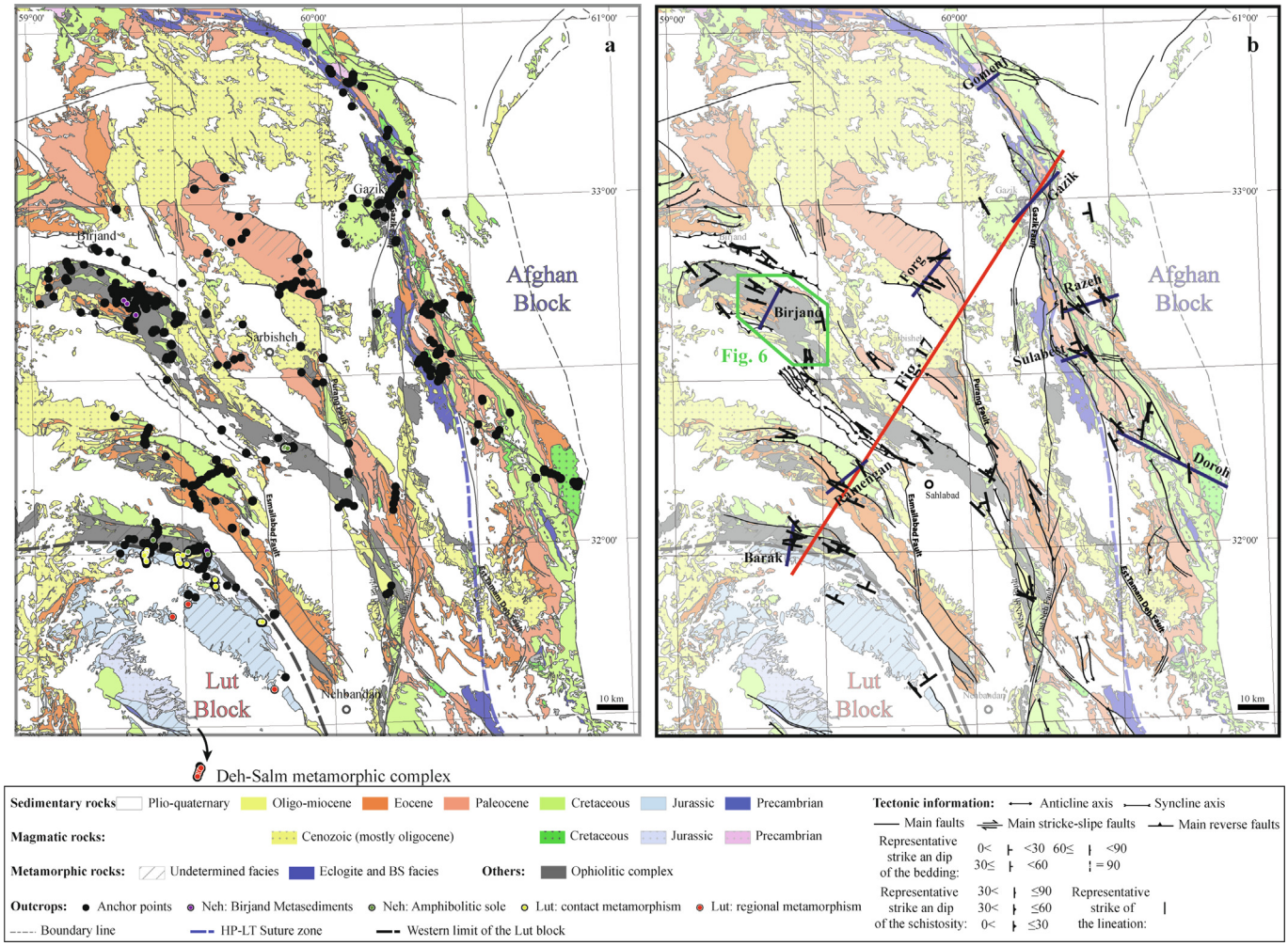

Fig. 4. Structural map of the North Sistan belt. **a)** Locations of the geological anchor points (in black) and metamorphic rocks samples. **b)** Representative structural measurement and position of cross-sections (blue and red lines) and structural map of Fig. 6 (green polygon).

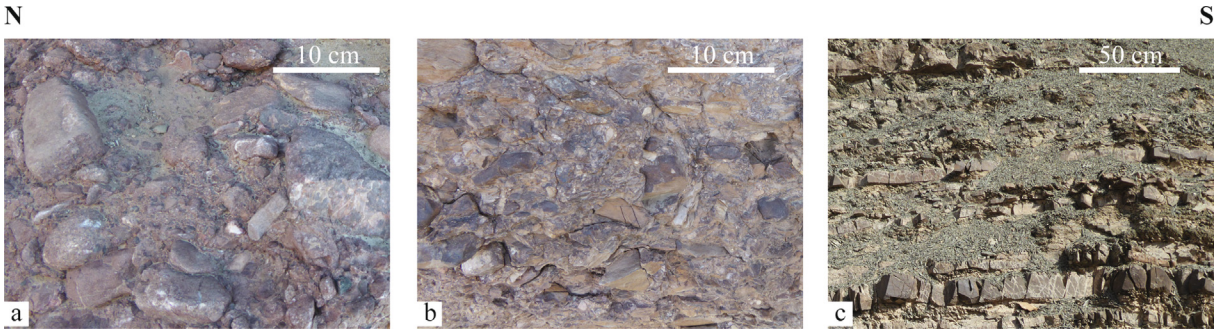

Fig. 5. Evolution from North to South of representative Eocene sedimentary rocks of the Neh Complex (GPS coordinates in supplementary Table 2).

The present-day seismic activity is distributed along hundred-kilometer-long N-S right-lateral faults, and along their conjugate left-lateral and reverse faults (Berberian et al., 2000; Walker and Khatib, 2006). This deformation is compatible with a N025 orientation of the main horizontal stress, most probably induced by far field compression in the Zagros collision (Jentzer et al., 2017; Fig. 3). These strike-slip faults act as major pathways for late Cenozoic intraplate alkali-basalts (ca. 27 to 2 Ma), which were ascribed to asthenospheric upflow following collisional delamination of the lithosphere (Camp and Griffis, 1982; Walker et al., 2009; Pang et al., 2012; Fig. 3).

3. Reappraisal of the North Sistan structural organization and major rock types

3.1. New tectonic map for the northern Sistan orogen

The six 1:250 000 scale maps of the North Sistan belt (Qayen, Shahrakht, Birjand, Gazik, Dehsalm, and Zabol) were combined to produce a comprehensive and consistent structural map (Fig. 4). Some simplifications and specific groupings were necessary. For example, exposures of ultramafic rocks and magmatic and sedimentary crustal rocks of the Sistan Ocean, as well as the "colored

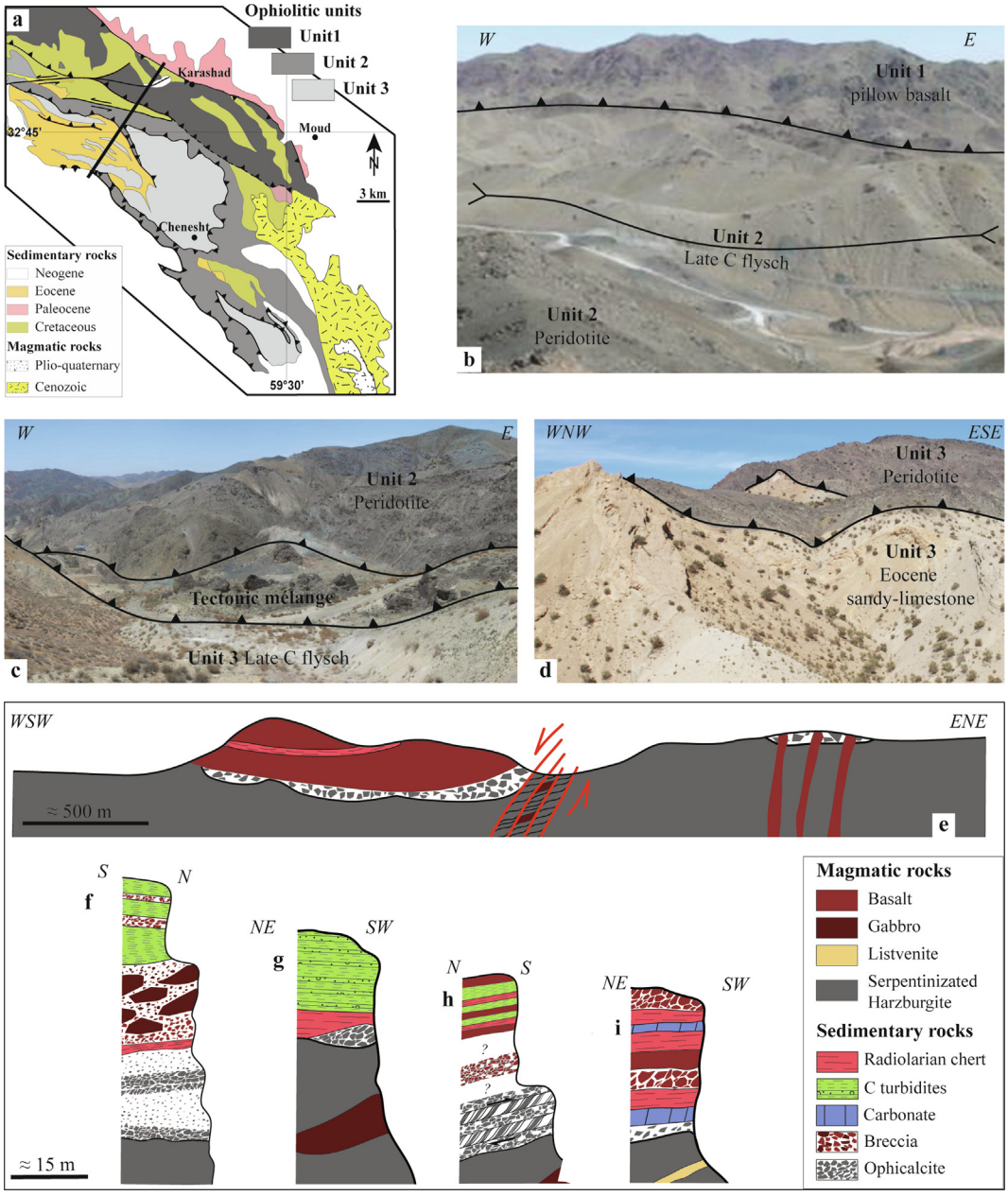

Fig. 6. Overall structure of Birjand ophiolitic ridge. **a)** Structural map of Birjand ophiolite ridge; **b-d)** Field exposures of the main tectonic contacts; **e-i)** Lithological columns of representative outcrops (GPS coordinates available in supplementary Table 2).

mélange", were merged into 'ophiolite' (Fig. 4). Magmatic rocks associated with tuff, volcanic breccia, and ignimbrite are shown by age. Sedimentary rocks are separated by age, except for the scarce Oligocene and Miocene continental deposits which were grouped together. Metamorphism is indicated by hatching. The already extensively studied HP-LT metamorphism of the Ratuk complex is highlighted but not studied here. This map shows that the mutual relationships between the five main domains defined by Tirrul et al. (1983) are still largely unclear.

3.2. Sedimentary features

We complemented the study of Tirrul et al. (1983) centered on the Sefidabeh Basin, the Ratuk Complex and the easternmost part of the Neh Complex. The Neh Complex exibits a fisrt order SW younging of the sediment sequence, with Late Cretaceous deposits in the NE, Paleocene sediments in its central part and Eocene deposits in the S. Eocene sediments are coarser in the NE, where massive polygenic continental puddingstone contain several centimeter-large jointed clasts (Fig. 5a). In the central part, a conglomerate contains centimeter-large jointed clasts (Fig. 5b). In the S, Eocene sediments are thin silici-clastic turbidites with alternation of centimenter-thick sandstone and schistosed argillite (Fig. 5c). All these lithologies are interbedded with a several meter-thick layer of Nummulite-bearing sandy limestone (Appendix A).

3.3. Ophiolitic rocks

New detailed mapping shows that the Birjand ophiolitic ridge comprises three kilometer-thick tectonic units (Figs. 6, 7, 8), with variable metamorphic degree and/or lithologies (Fig. 7; Appendix B): (i) variably serpentinized peridotites, which are dominantly harzburgites with olivine, orthopyroxene, rare clinopyroxene, Fe-Ti oxide and occasional amphibole and titanite (Fig. 7d); (ii) gab-

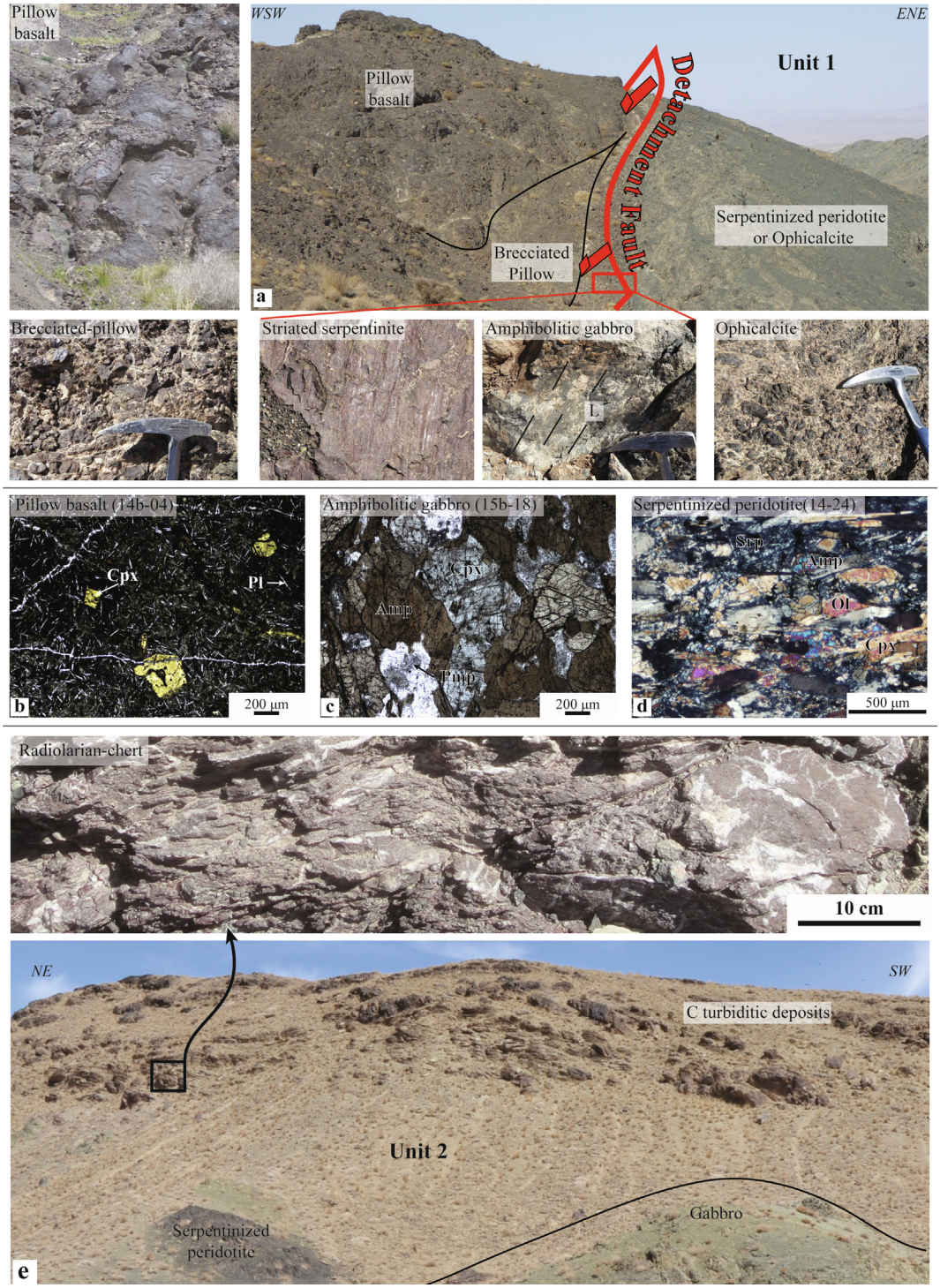

Fig. 7. Lithologies of the unmetamorphosed units 1 and 2 of the Birjand ridge. **a)** Representative outcrops of the Unit 1; **b-d)** Representative thin section of unmetamorphosed pillow basalt (b), gabbro (c) and serpentinized peridotite (d; Abbreviations are from Whitney and Evans, 2010); **e)** Representative outcrops of Unit 2 (all GPS coordinates are available in supplementary Table 2).

broic intrusions, with clinopyroxene and plagioclase commonly altered to prehnite, and with a weak foliation marked by amphibole in some samples (Fig. 7c); (iii) basalts, with clinopyroxene, plagioclase and Fe-Ti oxide phenocrysts (Fig. 7b), epidote and/or pumpellyite as secondary minerals, and occasional calcite veins.

– Unit 1 is characterized, from bottom to top, by serpentinized peridotites with scarce gabbroic intrusions, an almost continuous horizon of pillow-lavas and brecciated basalts, rare radiolarites and Cretaceous turbidites. This unit exhibits a hectometer- to kilometer-length normal fault zone, outlined

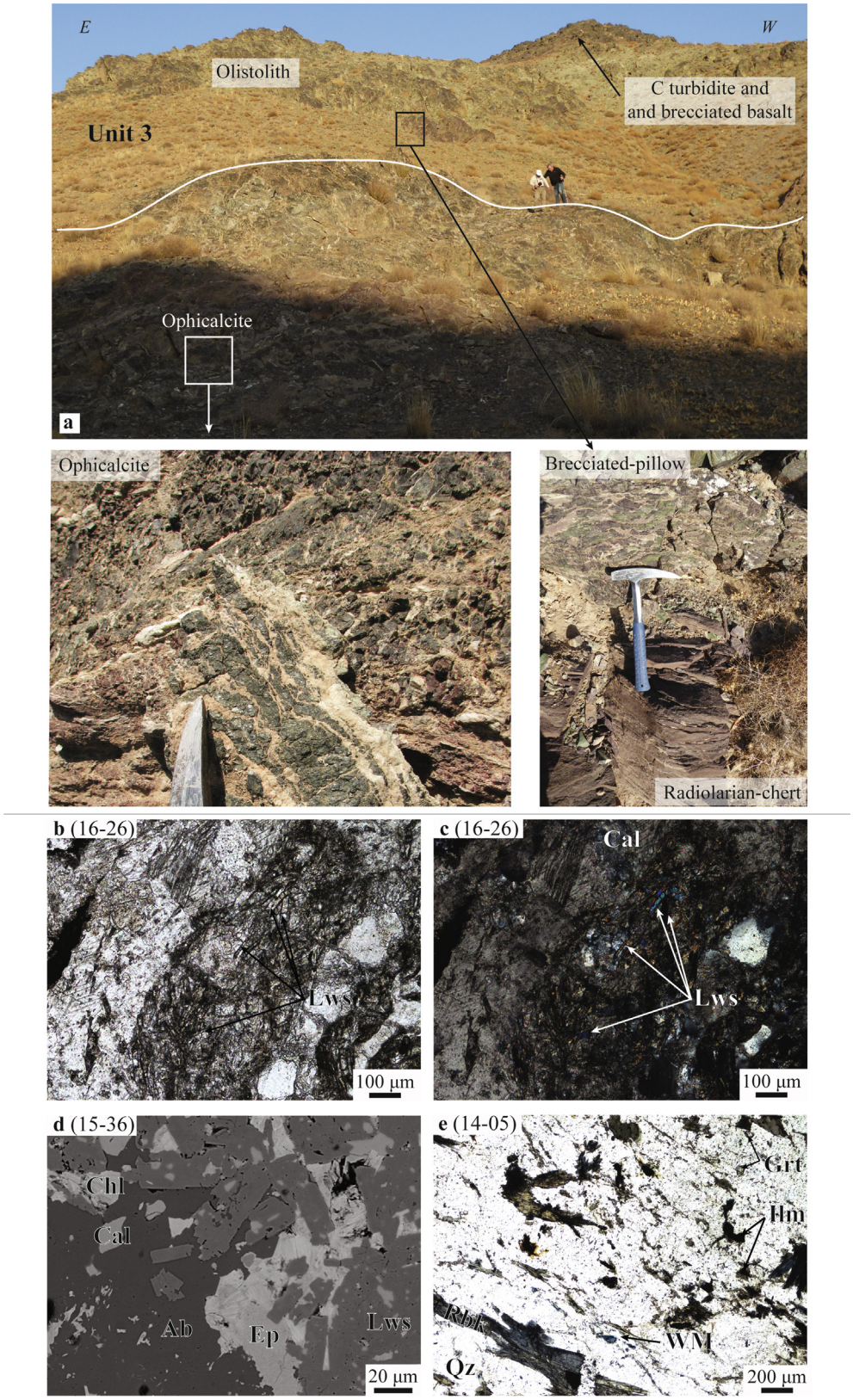

Fig. 8. Representative lithologies of the Birjand ridge metamorphic Unit 3. **a**) Representative outcrops of the Unit 3; **b-e**) Representative thin sections (b, c, e) or SEM (d) photomicrographs of brecciated pillow basalt (b-d) and metachert (e; Abbreviations are from Whitney and Evans, 2010; all GPS coordinates are available in supplementary Table 2).

by striated peridotite and foliated amphibolite facies gabbro (Figs. 6e, 7a). Thrusting of Unit 1 over Unit 2 is marked by a crushed zone with various dismembered materials (Fig. 6b).

– Unit 2 (Figs. 6c, 7e) comprises massively serpentinized peridodite with dunitic channels, cross-cut by scarce rodingites and plagiogranites. Gabbroic intrusions are more common than

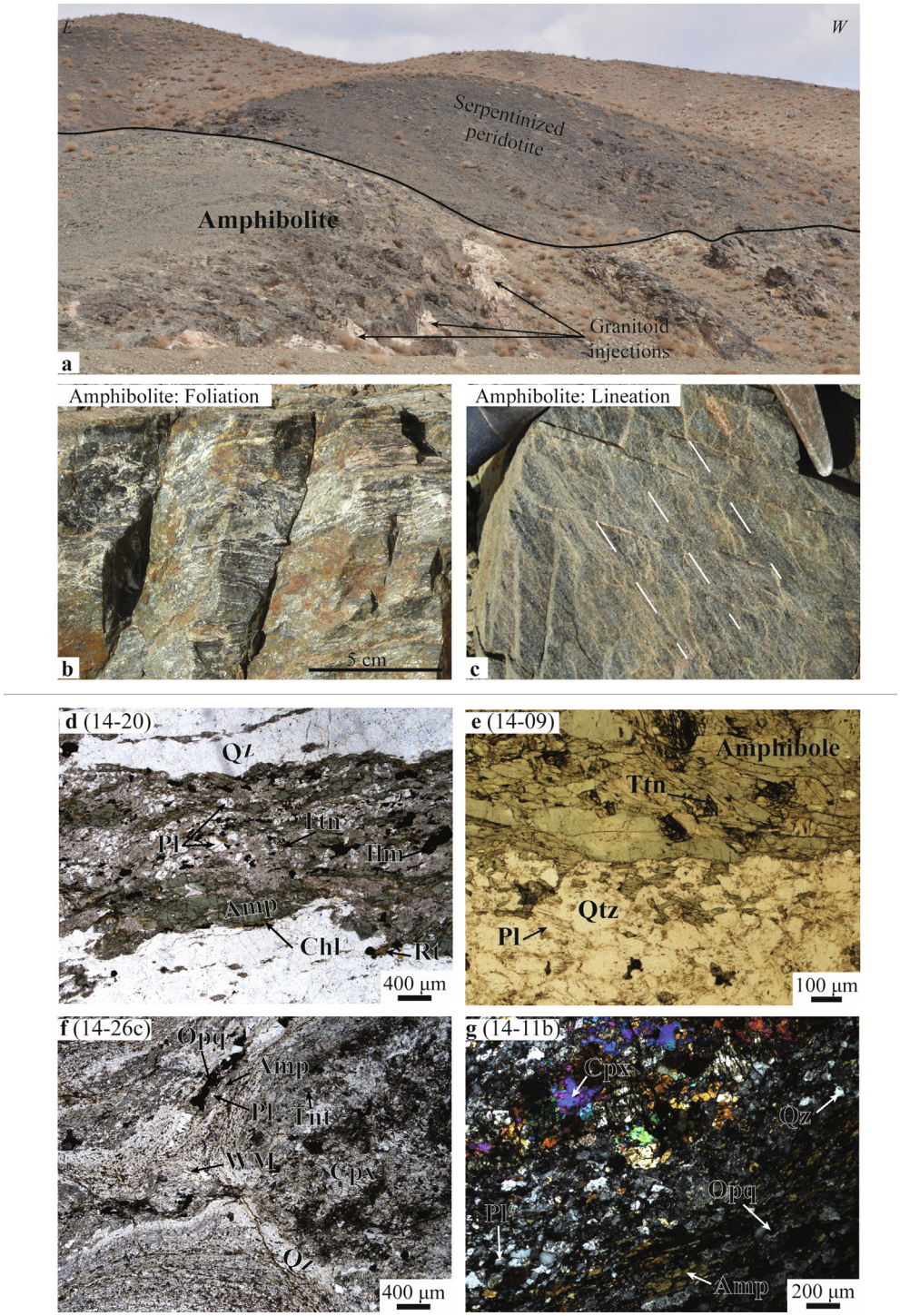

Fig. 9. Representative lithologies of the amphibolite. **a**) Structural position of the amphibolite at the base of serpentinized peridotite; **b-c**) Deformation visible in amphibolite: foliation and lineation (N150); **d-g)** Thin section of foliated amphibolite (d-e) and clinopyroxene-bearing amphibolite (f: porphyric clinopyroxene; g: tiny clinopyroxene in foliation; abbreviations are from Whitney and Evans, 2010; all GPS coordinates are available in supplementary Table 2).

in Unit 1. Ophicarbonates directly overlie the serpentinized peridotite (Fig. 6g-h-i). At the base of Unit 2, the contact onto Unit 3 is outlined by a tectonic mélange (Fig. 6c).

– Unit 3 crops out as a tectonic window below Unit 2 (Fig. 6c). It consists of serpentinized peridotite, intruded by large masses of gabbro and dolerite, overlain by ophicalcite and centimeter- to meter-large clasts in sedimentary breccia/olistostrome (Figs. 7f, 8a). Scarce pillow-lavas, radiolarian cherts and Cretaceous turbidites crop out discontinuously. An unconformable Eocene Nummulitic sandy limestone, overlying either the Cretaceous turbidite or the peridotite, is affected by large-scale asymmetric drag folds and locally overthrust by peridotites (Fig. 6d). Metasedimentary rocks are found only in Unit 3 (see below; Fig. 8b-d).

3.4. Metamorphic rocks from the Neh Complex and the Lut Block

(A) Two types of metamorphic suites were found at the base of the Neh Complex ophiolite (Appendix B; Fig. 4 for location). In the

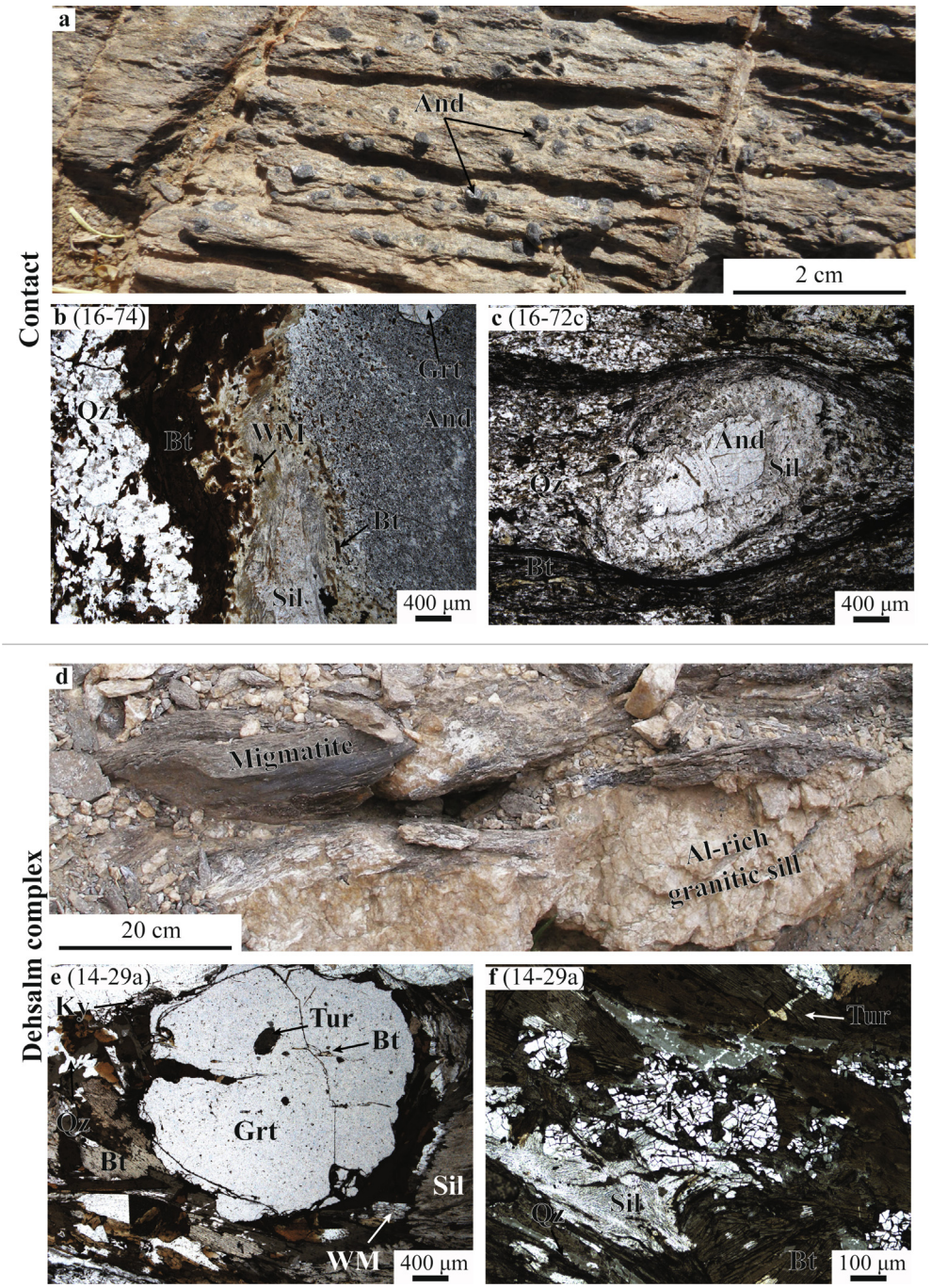

Fig. 10. Representative lithologies of the Lut block metamorphic rocks. **a-c**) Representative outcrop of andalusite-bearing micaschist close to the Neh Complex (a); Thin sections of andalusite-bearing micaschist exhibit the replacement of andalusite by sillimanite (b-c); **d-f**) Representative outcrop of the Deh-Salm migmatite (a); Thin sections of migmatite exhibit the main mineral assemblage: (1) kyanite, garnet, biotite, and white mica; (2) quartz, plagioclase and fibrous sillimanite parallel to the main foliation marked by (e, f; abbreviations are from Whitney and Evans, 2010; all GPS coordinates are available in supplementary Table 2).

Birjand ridge, metasediments were found in Unit 3 and within the tectonic slice separating Units 2 and 3 (Fig. 6c, 8). In Unit 3, metasediments comprise (i) ophicalcite composed by primary serpentine, magnetite, calcite, and by secondary garnet and lawsonite; (ii) basalt-rich breccia made of primary amphibole, titanite, calcite veins and lawsonite; (iii) gabbro-rich breccia, with gabbroic clasts containing plagioclase, clinopyroxene and metamorphic lawsonite locally retrogressed in epidote in a matrix made of calcite and lawsonite. The presence of lawsonite in the clasts and in the matrix indicates that brecciation occurred prior to the metamorphic event. In the tectonic slice separating Units 2 and 3, metamorphic rocks are meter-long boudins of meta-cherts containing quartz, scarce plagioclase and ilmenite, and less abundant blue amphibole, garnet, phengite, epidote, rare pyroxene and retrograde chlorite (Fig. 8e). Amphibole and phengite define a crude schistosity.

In the south and south-west of the Neh Complex, south of Barak and NE of Sahlabad (Fig. 4), amphibolites and associated metasediments are found in 10–20-meter-thick horizons located immediately below variably serpentinized peridotite (Fig. 9). Amphibolites comprise amphibole, plagioclase, accessory ilmenite (Appendix B; samples 14-01, 16-45b; Fig. 9b-e), and secondary

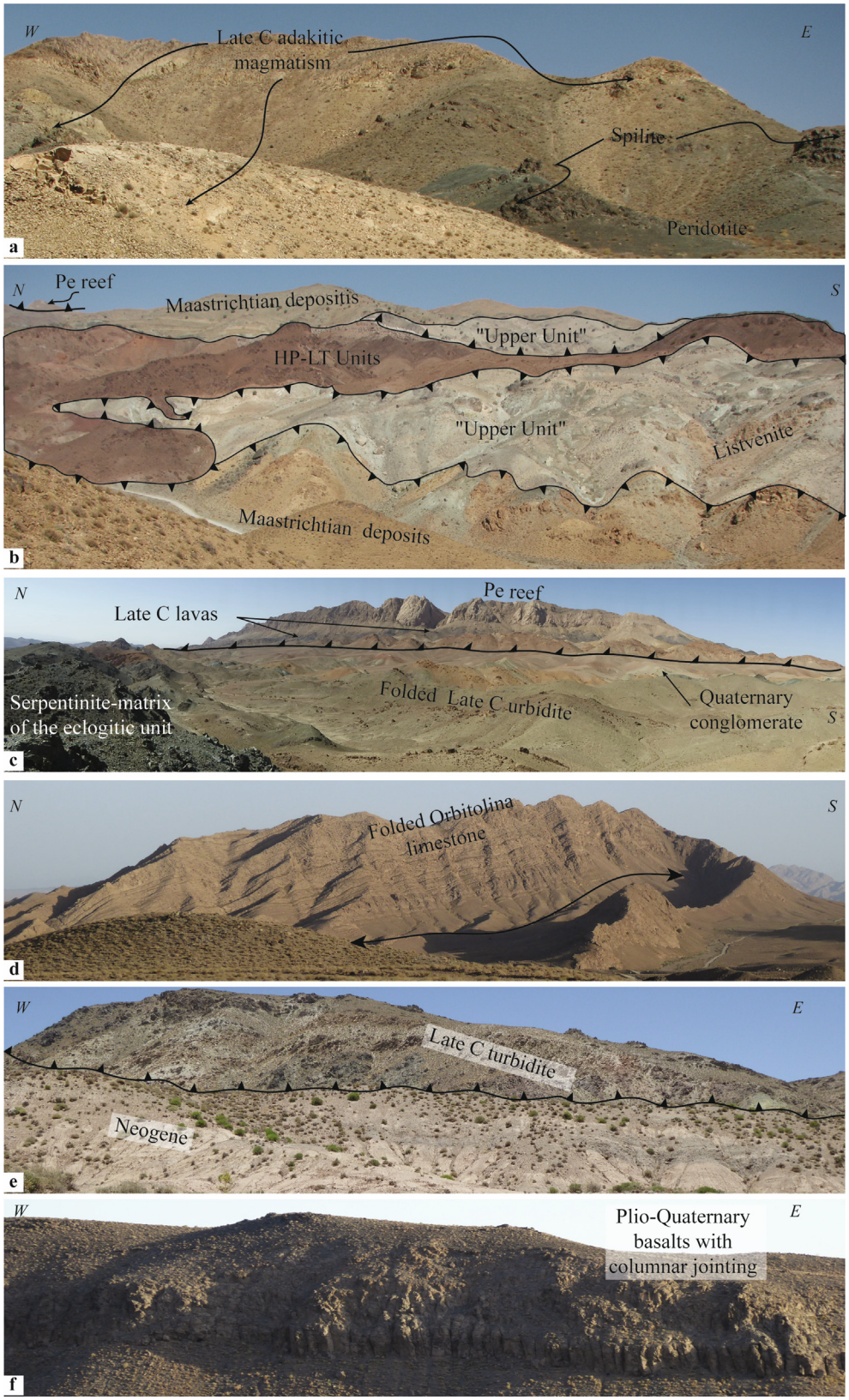

Fig. 11. Representative outcrops and landscapes of the eastern part of the Sistan orogen. **a)** Western Unit with Late Cretaceous adakitic dykes intruded into peridotite and spilite; **b)** Structure of the HP-LT domain; **c)** Contact between the Sefidabeh Basin and the HP-LT domain; **d)** Fold in the Afghan Block Orbitolina limestone; **e)** Contact between Late Cretaceous turbidite and Neogene deposits in the Gomenj area; **f)** Plio-Quaternary basalts with columnar jointing (all GPS coordinates are available in supplementary Table 2).

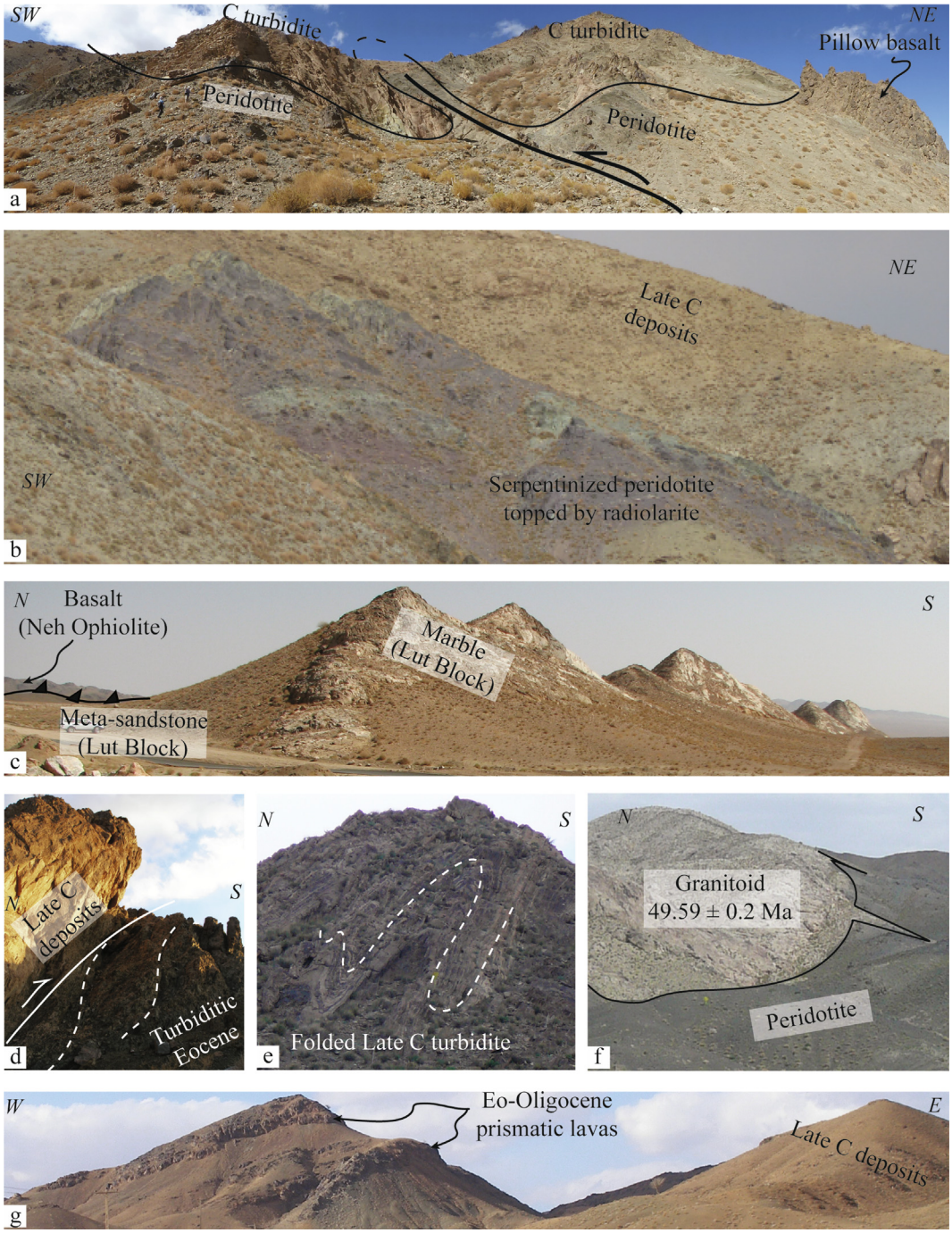

Fig. 12. Representative outcrops and landscapes of the Neh Complex. **a-b)** Outcrops of ophiolitic material; **c)** Contact between the Neh Complex and the Lut Block; **d-e)** Internal deformation of the Neh Complex: thrust and fold; **f-g)** Eo-Oligocene magmatic rocks in the Neh Complex (all GPS coordinates are available in supplementary Table 2).

minerals such as titanite, epidote and quartz. Some amphibolites additionally contain clinopyroxene (samples 14-11b2 to 17-18; Fig. 9f-g), either in the foliation or as boudins (in association with Ca-rich garnet in the latter case). All of them exhibit a pervasive schistosity and a stretching lineation marked by the N150 orientation of amphibole (Fig. 9). No clear shear senses could be identified. Associated metasediments (samples 14-07, 14-23a, 16-80) resemble metacherts and comprise quartz, white micas or biotite and retrograde chlorite.

(B) Two types of metamorphic suites were found in the Lut Block: one located close to the contact with the Neh Complex, and one in the northern part of the Lut Block, in the Deh-Salm Complex (Appendix B and Fig. 10). Near the Neh Complex, andalusite-bearing metasediments (Fig. 10a) exibit three types of mineral assemblages: one with biotite and occasional garnet inclusions in andalusite (sample 16–74; Fig. 10b); one showing the destabilization of andalusite into sillimanite, associated with white mica and biotite (Fig. 10b-c); the last type consists of biotite defining the main foliation, quartz and occasionally plagioclase (Fig. 10b-c). Accessory phases are tourmaline, Fe-Ti oxide, zircon and organic matter (Appendix B).

In the Deh-Salm Complex, metamorphic rocks evolve from amphibolite facies micaschists in the N to migmatites in the S (Fig. 10d). Micaschists comprise quartz and biotite in association with less abudant plagioclase, white mica, sillimanite and scarce orthoclase, together with tourmaline, rutile and titanite as accessory

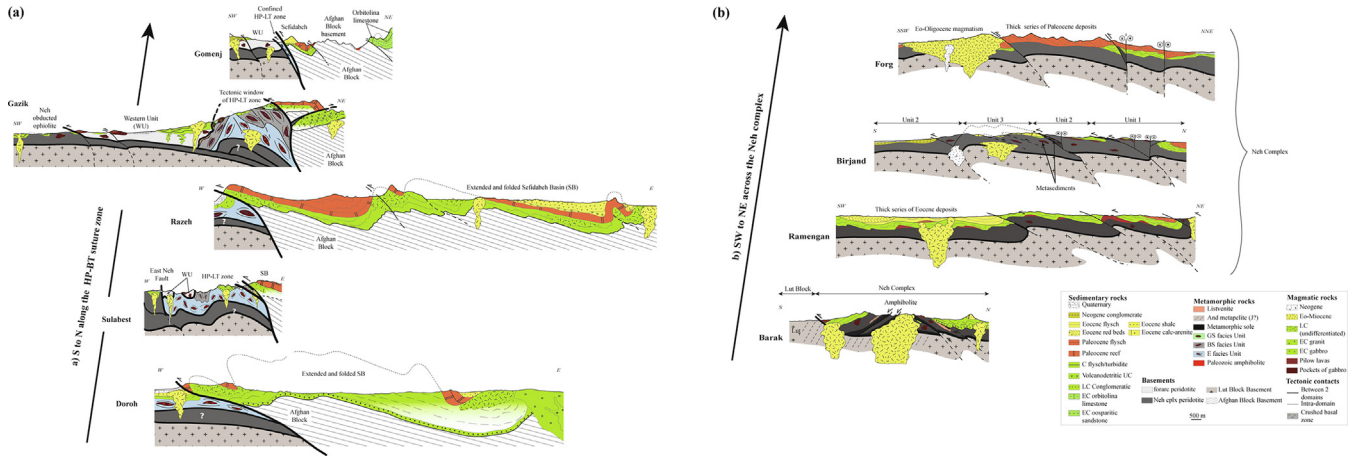

Fig. 13. Cross-sections across the Sistan orogen. **a)** Across de HP-LT domain; **b)** Across the Neh Complex (And: Andalusite; BS: Blueschist facies; E: Eclogitic facies; GS: Greenschist facies; J: Jurassic; C: Cretaceous; LC: Lower Cretaceous; UC: Upper Cretaceous; SB: Sefidabeh basin; WU: Western Unit).

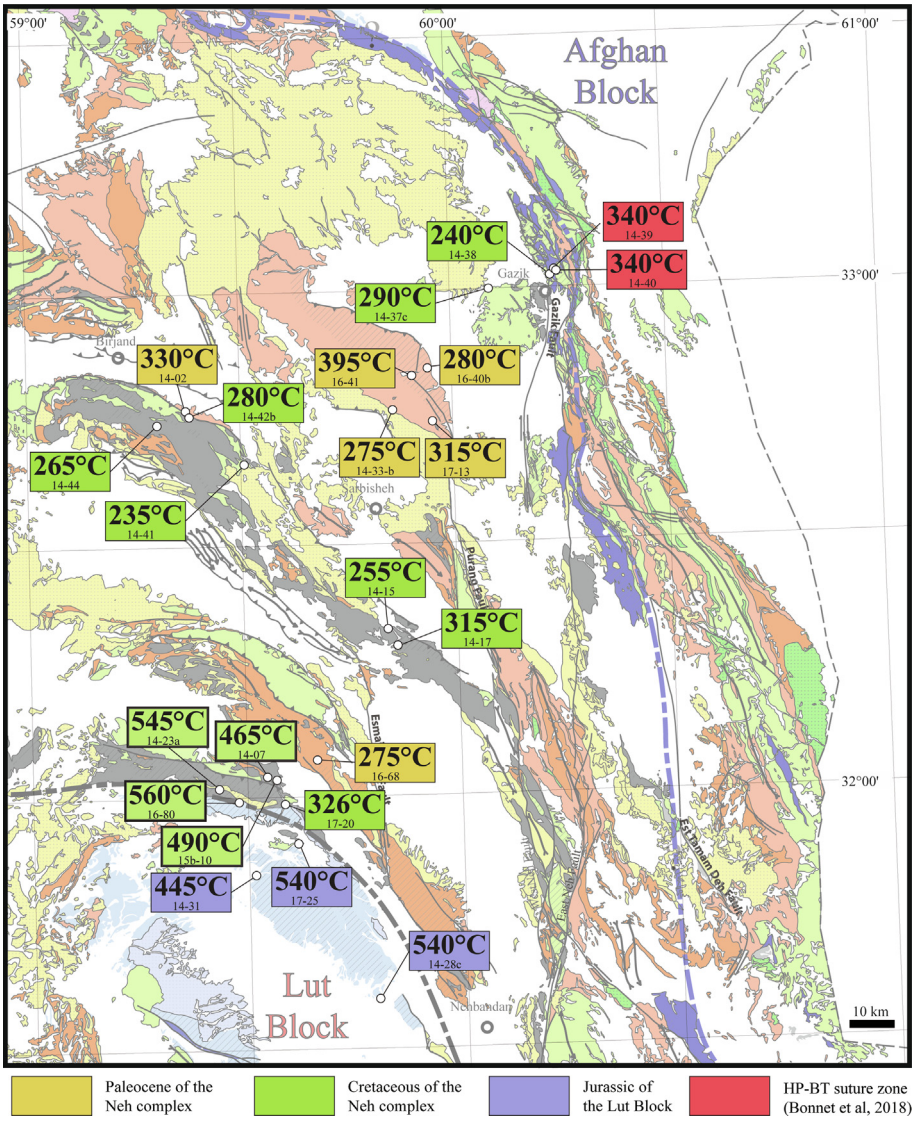

Fig. 14. Structural map with maximum temperatures recorded by sedimentary rocks (obtained by RSCM, details in supplementary Table 3).

phases. Micaschists are commonly associated with marble, metasandstone and amphibolite lenses comprising metamorphic amphiboles associated with minor epidote and occasional titanite and clinopyroxene porphyroclasts. Migmatites show three successive parageneses (Fig. 10d-f). The earliest paragenesis is made of kyanite, garnet, biotite, and white mica (Fig. 10e). The second one comprises quartz, plagioclase and fibrous sillimanite parallel to the main foliation, and appears contemporaneous with the formation of the leucosome (Fig. 10f). The latter comprises an association of prismatic sillimanite associated with white mica, and later biotite cutting across the main foliation and likely postdating melting. Accessory minerals include tourmaline and Fe-Ti oxide (Appendix B).

4. Sections across the northern branch of the Sistan orogen

Two sets of sections across the North Sistan are presented, one along the HP-LT zone and one across the Neh Complex (Figs. 11-13).

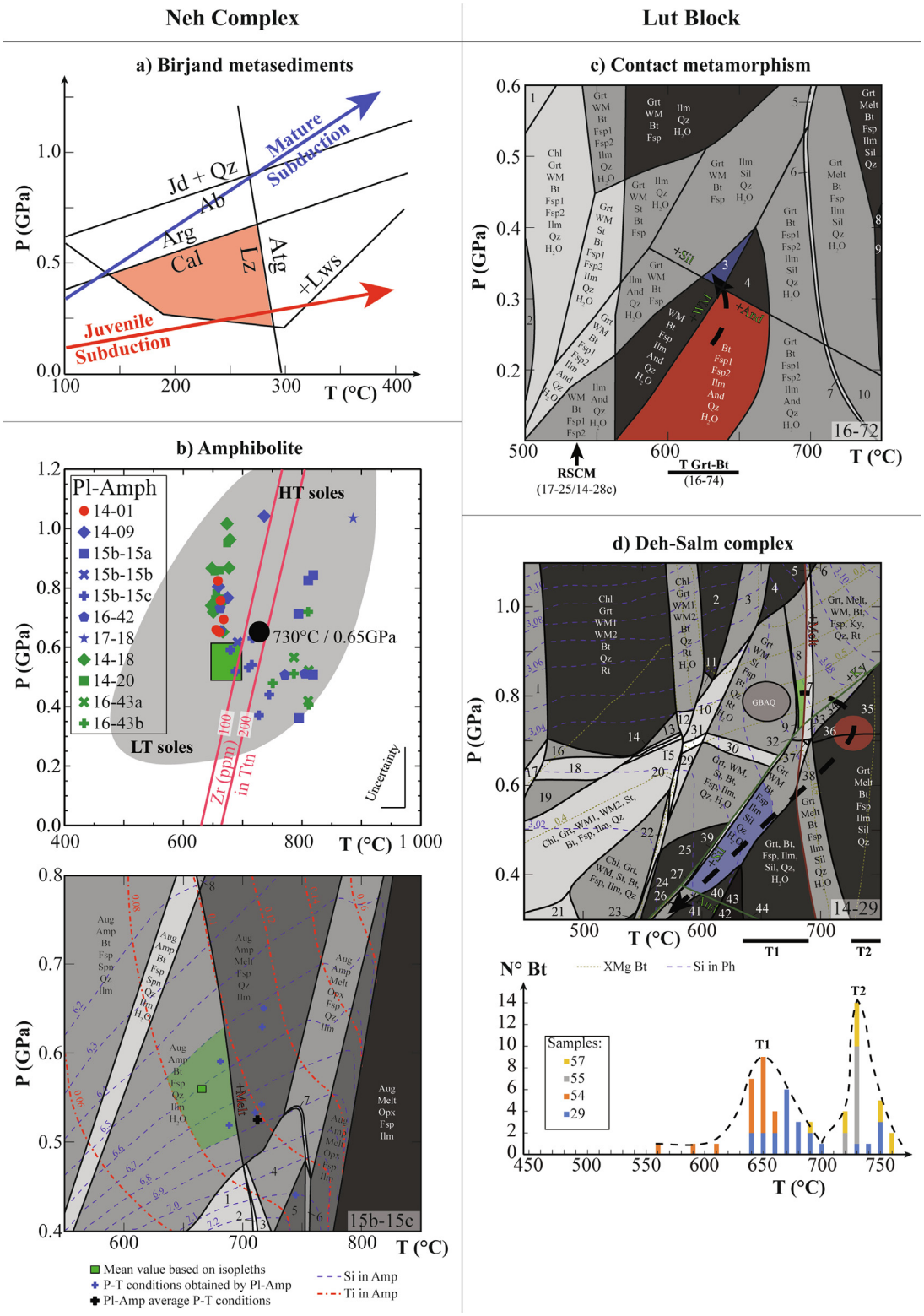

4.1. Sections across the HP-LT zone

The E-W sections across the HP-LT zone allow to refine the relationships between five main domains (Fig. 11a):

- The Neh Complex is recognized, in the Gazik and Sulabest sections, by serpentinite exposures hosting meter- to hectometer-large gabbroic intrusions, which are covered by rare radiolarite or basalt and overlain by folded Late Cretaceous turbidite.
- The Western Unit represents the westernmost domain related to the Afghan Block. It is made of serpentinized peridotite locally intruded by gabbro and covered by pillow basalt and/or radiolarite and by Maastrichtien turbidite at the top. Contrary to the Neh Complex, however, the Western Unit is cut across by Senonian arc magmatism (Fig. 11a). The thrust contact between the Neh Complex and the Western Unit steepens towards the S and connects to the strike-slip East Neh Fault.
- The HP-LT domain crops out in tectonic windows and comprises three main units (Fig. 11b): (i) the structurally lowest unit is a serpentinite-matrix mélange made of a fine-grained to locally massive matrix surrounding metamorphosed pillow-lava and metatuff. In the Gazik area, this mélange can be sub-divided into eclogitic and upper blueschist portions; (ii) the intermediate "upper unit" is a mélange comprising blocks of marl, radiolarite, serpentinite, sandstone or basalt, metamorphosed in the greenschist to epidote blueschist facies at most, embedded within a tuffaceous matrix. The amount of blocks is lower in the S (Sulabest) than in the N (Gazik); (iii) the uppermost unit is a Maastrichtian basal conglomerate grading upwards into a turbiditic sequence, which unconformably overlains the two previous units. To the N (Gomenj), these units cannot be distinguished and the HP-LT domain is restricted to a ~100 m-thick crushed zone with amphibolitized blocks in a serpentinite matrix and with abundant listvenite.
- The Sefidabeh Basin (see § 2.1) shows west-vergent asymmetric folds outlined by Paleocene reefal limestone, and significantly widens southward (Fig. 11c). Its present-day contact with the HP-LT domain is tectonic. It accommodated part of the exhumation of the HP-LT units and was reworked into a major thrust (Doroh, Sulabest, Razeh and Gomenj) or a right-lateral strike-slip fault (Gazik). In the Gazik area, steep faults and back-thrusts hint to the existence of a flower structure along the contact.
- The Afghan Block forms the basement of the Sefibadeh basin. To the N of the study area, along the Gomenj section, this basement is made of Paleozoic granodiorite, amphibolites and an Early Cretaceous sedimentary cover (i.e., oosparitic sandstone older than Orbitolina limestone). In the western part of the Afghan Block, basement rocks are thrusted over the Sefidabeh Basin. In its eastern part, large-scale folds affect the sedimentary cover (Fig. 11d).

All sections testify to the existence of recent to ongoing tectonic activity, as shown by the deformation of Neogene deposits (Fig. 11e). Pliocene to Quaternary alkali-basalts with columnar joints are present close to the East Neh Fault and in the vicinity of major faults (Fig. 11f). Eo-Miocene magmatism is also widespread (Fig. 4).

4.2. Sections across the Neh Complex

Ophiolitic rocks are found only locally along the Forg and Ramengan sections, whereas they form a kilometer-wide stack of units along the Birjand and Barak sections (Fig. 12a, b, 13b). The basement of the Neh Complex, in all sections, is made of mostly unmetamorphosed ophiolite. The scarce metamorphic rocks found in the Neh ophiolite are always located at the base of ophiolitic sheets or in the basal unit (Unit 3, § 3.4; Figs. 8, 9).

The Neh Complex is overthrusted by the Western Unit to the NE, whereas it is thrusted over the Lut Block to the SW (Fig. 12c). Likewise, all internal deformation patterns exibit a southwest vergence (Fig. 12d, e). The Birjand section shows that Neogene deposits are deformed by recent tectonic activity, as observed along sections across the HP-LT zone.

In the NE, along the Forg section, the sedimentary cover is mainly made of Cretaceous and Paleocene deposits while in the southwest, along the Ramengan section, the sedimentary cover is mainly made of Eocene deposits. The Neh Complex is pervaded by Eo-Miocene magmatism (Fig. 12f, g). Pliocene to Quaternary alkali-basalts are locally present.

5. P-T-t estimates in the western part of the north Sistan orogen

The P-T conditions experienced by each type of metamorphic suite are summarized in Figs. 14 and 15. Radiometric ages are shown in Fig. 16. For the sake of readability, analytical and thermobarometric methods are described in Appendix B and mineral chemistry is given in Appendix C (see Supplementary Table 3 for microprobe analyses).

5.1. Neh ophiolite and associated sediments

- Ophiolitic material: For the amphibolitized gabbro of the Birjand ridge normal fault zone (Unit 1; Fig. 8e), semi-quantitative amphibole geothermobarometry (Ernst and Liu, 1998) indicates a temperature between 625 °C and 775 °C and a pressure between 0.3 GPa and 0.7 GPa. $^{40}Ar/^{39}Ar$ step-heating of amphiboles from this gabbro provided a plateau age of 106.3 ± 3.1 Ma (100% of released ^{39}Ar; Fig. 15a). Elsewhere, ophiolitic material shows metamorphic conditions in the prehnite-pumpellyite to greenschist facies at most.

Fig. 15. P-T conditions estimates for the Neh Complex and Lut Block metamorphic rocks. **a)** P-T conditions estimates for the calcite-lizardite-lawsonite assemblage from the Birjand ridge metasediments (after Bonnet et al., 2019). Initiation or mature subduction gradient are from Agard et al. (2018, 2020); **b)** P-T conditions estimates for the amphibolite of the Neh Complex. Top: coupled amphibole-plagioclase thermobarometry (samples in green come from the N, samples in blue come from the S and sample in red was remorked in Eocene deposit) and Zr content in titanite (grey areas corresponds to P-T conditions observed in metamorphic sole worldwide Agard et al., 2016). Bottom: results of thermodynamic modelling on sample 15b–15c (method available on Appendix B; mineral assemblage for the fields 1 to 8 are on supplementary Table 4); **c)** Estimates of P-T conditions for the micaschist of the Lut Block by garnet-biotite thermometry and thermodynamic modelling on sample 16–72 (3: WM, Bt, Fsp, Ilm, Sil, Qz, H_2O; 4: Bt, Fsp_1, Fsp_2, Ilm, Sil, Qz, H_2O; method available on Appendix B, and all mineral assemblage for the fields 1 to 10 are available on supplementary Table 4); **d)** P-T conditions estimates for migmatite of Deh-Salm complex by Ti-in biotite thermometry, garnet-biotite-aluminosilicate-quartz thermobarometry, and thermodynamic modelling on sample 14–29 (method available on Appendix B, 7: Grt, Melt, WM, Bt, Fsp, Ky, Qz, Rt, H_2O; 8: Grt, WM, Bt, Fsp, Ky, Qz, Rt, H_2O; 9: Grt, WM, St, Bt, Fsp, Ky, Qz, Rt, H_2O; 33: Grt, Melt, WM, Bt, Fsp, Sil, Qz, Rt, H_2O; 34: Grt, Melt, WM, Bt, Fsp, Sil, Qz, Rt; 35: Grt, Melt, Bt, Fsp, Sil, Qz, Rt; 36: Grt, Melt, Bt, Fsp, Ilm, Sil, Qz, Rt, H_2O; 37: Grt, Melt, WM, Bt, Fsp, Ilm, Sil, Qz, Rt, H_2O; 38: Grt, Melt, WM, Bt, Fsp, Ilm, Sil, Qz, H_2O; 39: Grt, WM, St, Bt, Fsp, Ilm, Sil, Qz, H_2O; 40: WM, Bt, Fsp, Ilm, Sil, Qz, H_2O; all mineral assemblage for the fields 1 to 44 are available on supplementary material 3). Grey shades on pseudosection indicate the field variance from 2 in white to 6 in black.

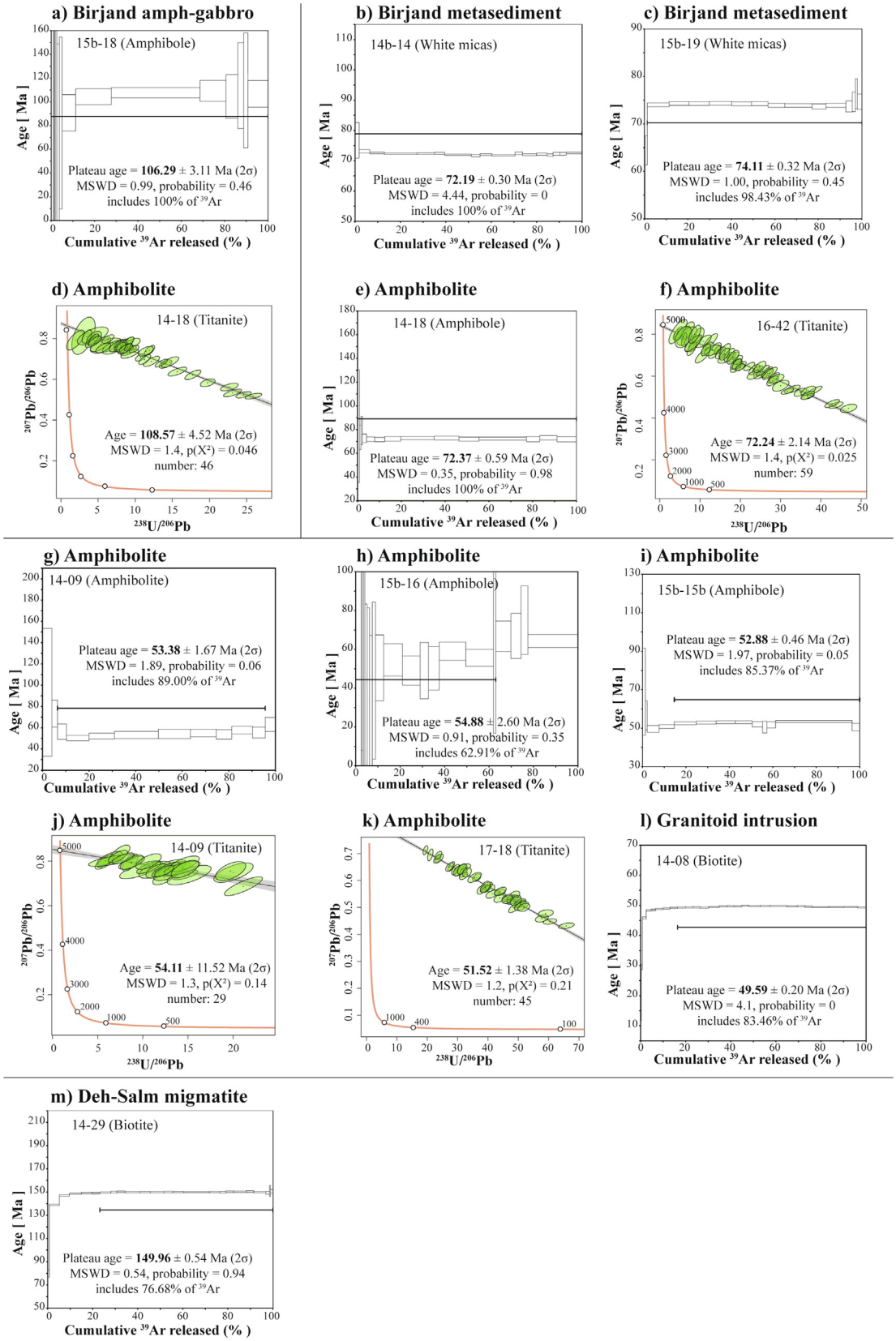

Fig. 16. Tera-Wasserburg diagrams showing results of U-Pb dating of titanite with 95%-confidence error ellipses and ^{40}Ar-^{39}Ar age degassing spectra for amphibole, biotite or white mica (methods available on Appendix B). **a)** ^{40}Ar-^{39}Ar age for an ophiolitic gabbro; **b-c)** ^{40}Ar-^{39}Ar age for samples of the Birjand ridge metachert; **d-k)** U-Pb and ^{40}Ar-^{39}Ar age for the amphibolites of the Neh Complex; **l)** ^{40}Ar-^{39}Ar age for the granitoid intrusion; **m)** ^{40}Ar-^{39}Ar age for the Deh-Salm migmatite.

– Sediments: The Raman spectroscopy of carbonaceous material method (RSCM) was used to determine the maximum temperatures (Tmax) experienced by the sedimentary sequence of the Neh Complex. Results were obtained for thirteen Late Cretaceous turbidites and five Paleocene ones (Fig. 14; Supplementary Table 3). None of the Eocene samples yielded results due to a too low or oxidized organic content. Most Tmax lie in the range 230–330 °C (average value: 275 °C ± 50 °C), except in the southern part of the Neh Complex (Fig. 14). Late Cretaceous and Paleocene samples appear undistinguishable in terms of Tmax. The higher Tmax of sample 16–41 (395 °C, Fig. 14) may result from the presence of nearby intrusions, which are known to affect Tmax estimates (e.g., Chen et al., 2017). Except for sample 17–20 (326 °C), samples from the S of the Neh Complex (14-07; 14-23a, 15b-10 and 16-80), which belong to the basal unit of the ophiolitic stack (Barak section in Fig. 13b), have a higher Tmax (515 °C on average), close to that obtained for the Lut Block Jurassic rocks (i.e. 508 °C on average, Fig. 14).

5.2. Metamorphic rocks of the Neh Complex

For the Birjand metasediments, the presence of lawsonite, calcite and lizardite allow to estimate P-T conditions between 150 and 300 °C and 0.2 to 0.6 GPa (Fig. 15a). $^{40}Ar/^{39}Ar$ step-heating of phengite from two metacherts yielded plateau ages of 72.2 ± 0.3 and 74.1 ± 0.3 Ma (with 100% and 98.43% of released ^{39}Ar, respectively; Fig. 16b, c).

Plagioclase-amphibole geothermobarometry (Holland and Blundy, 1994; Molina et al., 2015; Fig. 15b) on eleven amphibolites gave a large range of metamorphic peak conditions, with an average value at 730 °C ± 40 °C and 0.65 GPa ± 0.2 GPa. No significant difference exists between samples from the S or from the N. Thermometry based on the Zr content in titanite (~150–200 ppm; Hayden et al., 2008) yielded temperature estimates in the range 650–750 °C (Fig. 15b), consistent with results of plagioclase-amphibole thermobarometry. Thermodynamic modelling was performed for sample 15b–15c using Perple_X (Connolly, 2005; see Appendix B and Supplementary Table 4). Based on the Ti and Si isopleths of amphibole and the absence of melting, peak P-T conditions are estimated at around 700 °C and 0.6 GPa (Fig. 15b). They are thus undistinguishable from the average P-T conditions estimated by plagioclase-amphibole thermobarometry on this sample (714 ± 40 °C, 0.54 ± 0.2 GPa; Fig. 15b). The predicted modes of the main phases also agree with the observed mineralogy: between 40 and 45 vol% of plagioclase, 40 to 45 vol% of amphiboles. Thermodynamic modelling predicts the presence of biotite < 2 vol% and augite < 7 vol%, which have not been observed in the thin-section, possibly due to low abundance and/or potential retrogression. Dating of these amphibolites reveals three age populations. In-situ U-Pb dating of titanite yielded a Tera-Wasserburg isochron age of 108.6 ± 4.5 Ma (sample 14–18; Fig. 16d). Two intermediate ages were obtained on two different samples: one at 72.4 ± 0.6 by $^{40}Ar/^{39}Ar$ step heating of amphibole (sample 14–18; Fig. 16e) and another at 72.2 ± 2.1 Ma by in-situ U-Pb dating of titanite (sample 16–42; Fig. 16f). The five undistinguishable younger ages were obtained on four samples: three by $^{40}Ar/^{39}Ar$ step heating method on amphibole at 53.4 ± 1.7, 54.9 ± 2.6, 52.9 ± 0.5 Ma (with 89%, 63% and 85% of released ^{39}Ar, respectively; Fig. 16g-i), and two by in-situ U-Pb on titanite at 54.1 ± 11.4 and 51.5 ± 1.4 Ma (Fig. 16g-k). Dating by Ar-Ar and U-Pb on sample 14–09 gave undistinguishable ages, respectively at 53.4 ± 1.7 and 54.1 ± 11.4 Ma. In contrast, the same two methods provided significantly different ages for sample 14–18, at 72.4 ± 0.6 and 108.6 ± 4.5 Ma, respectively. Amphibolites from the S (Fig. 15b) were collected close to a deformed granitoid which was dated by the $^{40}Ar/^{39}Ar$ step heating method on biotite at 49.6 ± 0.2 Ma (with 83% of released ^{39}Ar; Fig. 16l).

5.3. Metamorphic rocks of the Lut Block

The P-T conditions experienced by the micaschists located immediately to the S of the Neh Complex were estimated by comparing the observed parageneses with their predicted field stability (sample 16–72; Fig. 15c; see Appendix B and Supplementary Table 4). The biotite-andalusite assemblage is stable between 600 ± 40 °C and 0.2 ± 0.1 GPa (Fig. 15c), whereas the later white mica-sillimanite-biotite assemblage is stable between 635 ± 15 °C and 0.35 ± 0.03 GPa (Fig. 15c). These P-T estimates are consistent with the results of the garnet-biotite thermometry performed on sample 16–74 (600–650 °C ± 25 °C) and advocate for a slight increase in pressure with time.

The Deh-Salm migmatite was studied by three independent methods. Thermometric estimates based on the Ti content of biotite (Henry, 2005) reveal two clusters of temperature at 670 °C ± 30 °C and 740 °C ± 20 °C (Fig. 15d). Garnet-Biotite-Alumi nosilica-Quartz geobarometry coupled with Garnet-Biotite geothermometry (GBAQ/GB; Holdaway, 2000; Wu, 2017) show that the P-T conditions of the kyanite-garnet-biotite-phengite-bearing assemblage of sample 14–29a lies between 640–670 °C ± 25 °C and 0.75–0.85 GPa ± 0.2 GPa (Fig. 15d). Thermodynamic modelling was performed for the migmatitic sample 14–29a (Fig. 15d, see Appendix B and Supplementary Table 4). Caution is needed with peak P-T estimates since the overall chemistry may have been

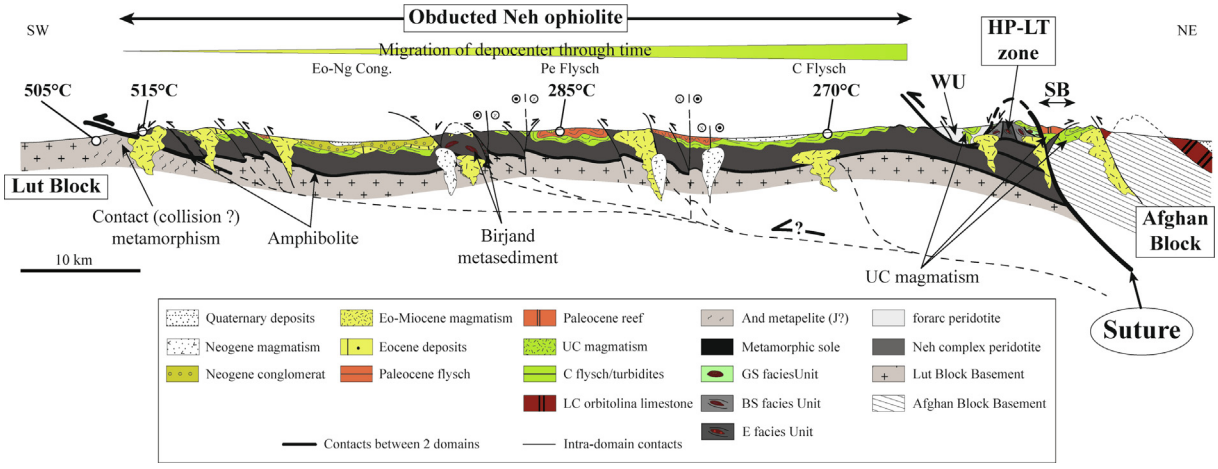

Fig. 17. Synthetic cross-section of the North Sistan orogen located on Fig. 4 (And: Andalusite; BS: Blueschist facies; Cong.: Conglomerate; E: Eclogitic facies; Eo: Eocene; GS: greenschist facies; J: Jurassic; C: Cretaceous; LC: Lower Cretaceous; UC: Upper Cretaceous; Ng: Neogene; Pe: Paleocene; SB: Sefidabeh Basin; WU: Western Unit).

modified by partial melting. This does not apply to the paragenesis postdating melting (i.e., with prismatic sillimanite, white mica, and biotite), which yields conditions between 590–670 °C, and 0.35–0.6 GPa (Fig. 15d). Less than 2% of garnet is predicted but not observed in the thin-section. Conditions for the quartz-plagioclase-sillimanite leucosome are modelled above 690 °C, in agreement with the results of Ti-in-biotite thermometry at ~740 °C. A rough estimate for the pressure is 0.7 GPa (Fig. 15d). The quartz-biotite-sillimanite-garnet-kyanite-plagioclase ± rutile paragenesis is stable at ~670 °C, 0.8 GPa, close to the P-T conditions determined using GBAQ/GB geothermobarometry, which may suggest only minor modification of the overall chemistry by partial melting. The succession of these mineral assemblages suggests a clockwise P-T path (Fig. 15d). Sample 14–29 was also dated by $^{40}Ar/^{39}Ar$ step heating method on biotite at 150.0 ± 0.5 Ma (with 77% of released ^{39}Ar; Fig. 16m).

6. Discussion

6.1. Overall structure of the northern Sistan orogen

The structural and petrological data of this study are summarized on a synthetic SW-NE crustal-scale section across the N Sistan orogen (Fig. 17, located on Fig. 4). The Afghan Block occupies the highest structural position in the Sistan orogen. We propose that the adjacent, unmetamorphosed ophiolitic sequence of the Western Unit, which was intruded by subduction-related Late Cretaceous magmatism (~86–71 Ma; Zarrinkoub et al., 2012; Jentzer et al., 2020), represents either the stretched ocean continent transitional domain of the Afghan Block or a forearc domain accreted to it. The HP-LT rocks crop out as a tectonic window and mark the location of the suture zone. Early tectonic stacking and later doming characterize this domain, which pinches out towards the N. The suture zone contact is presently reworked by steeply dipping faults.

In contrast to this strongly reworked and steepened portion of the orogen, the Neh Complex preserves a relatively continuous obducted ophiolite, 50 to 80 km large across the studied profile (and > 100 km along strike; Fig. 16). The Neh ophiolite is thrust over the Lut Block and overthrust by both the Ratuk Complex and the Western Unit (which we relate to the Afghan Block). It is characterized by discontinuous pillow-lava sequences up to a few hundred meters thick and isolated gabbros intruding serpentinized peridotite. No sheeted dyke complex was found. Ophicalcite or mass wasting deposits of brecciated basalt and/or gabbro directly overlie serpentinized peridotite. The Neh ophiolite therefore suggests that the Sistan Ocean resembled modern-day slow-to ultra-slow-spreading oceans (e.g. Cannat et al., 2009, Picazo et al., 2012; Escartín et al., 2017). This is consistent with the finding of a normal fault zone (Unit 1, Birjand ridge; § 3.3) hosting a 106 Ma amphibolitized gabbro deformed at 700 ± 75 °C and 0.5 ± 0.2 GPa, which we tentatively interprete as an oceanic detachment fault. Evidence for Early Cretaceous or earlier normal faulting in the Afghan Block could also reflect thinning of the continental margin during the rifting stage of the Sistan Ocean.

The overall tectonic vergence, which is marked by major contacts dipping towards the NE, top to the SW thrusts and underthrusting of the Neh Complex below the Afghan Block, strengthens the view that subduction dipped to the NE, as proposed by Tirrul et al. (1983). This interpretation is also consistent with the location of a Late Cretaceous magmatic arc to the E of the suture zone (Jentzer et al., 2020). The southwestward shift of depocenters in the Neh Complex with time, from the Cretaceous to Paleocene and finally Eocene, suggests an "en sequence" migration of the flexure in the lower plate with respect to the suture zone. The thrust contact of the Neh Complex onto the Lut Block is cut by lowermost Eocene acidic intrusions (~50 Ma), indicating that final closure of the Sistan basin was completed by then.

Collisional shortening is relatively modest (Fig. 17). Structures associated with early shortening, such as the distinct ophiolite sheets (i.e., Units 1–3 of the Birjand ridge; Figs. 6, 13), are still preserved. The continental basement of the Lut Block is not exposed below the Neh Complex (Fig. 17), suggesting that it is not strongly affected by deformation and that thick-skin tectonics are insignificant. The maximum temperature experienced by the Neh Complex sediments (~275 °C on average) may therefore reflect a warm thermal gradient without much tectonic burial. While the presence of the Lut Block below the Neh Complex cannot be ascertained from field observations alone, gravimetric data show an increase of Moho depth below the Sistan orogen (Fig. 2a; Mousavi and Ebbing, 2018; Eshagh et al., 2019). The Sr and Nd isotopic ratios of Eo-Oligocene magmatic rocks, which indicate a continental crust component (Mohammadi et al., 2016; Pang et al., 2013), also support the presence of the Lut continental basement below the Neh ophiolite.

The northward increase of deformation of the Sefidabeh and Ratuk domains indicate that shortening varies along strike. In the absence of clear stratigraphic markers allowing to perform balanced cross-sections, estimating the amount of shortening in the North Sistan orogen is fraught with large uncertainties. A crude unfolding of ophiolite sheets and deformed basins (Fig. 17) suggests ~30–50 km of shortening since closure of the oceanic realm, and a minimum estimate of 80–100 km for the obduction- and/or collision-related overthrusting of the Neh Complex onto the Lut Block.

6.2. Geodynamic significance of metamorphic rocks

6.2.1. Neh Complex: Evidence for metamorphic sole formation and intra-oceanic slicing during the onset of obduction

In addition to mineral transformations associated with oceanic deformation and/or hydrothermal alteration (Tirrul et al., 1983; Saccani et al., 2010; Zarrinkoub et al., 2012), two other types of metamorphic rocks were found at the base of some tectonic contacts in the Neh Complex. The fist type corresponds to strongly foliated and lineated amphibolite facies metabasalts and metasedimentary rocks (Fig. 9) found as 10–20 m thick horizons underlying peridotites, exclusively at the base of ophiolitic sheets. These characteristics, together with their metamorphic peak at 700 °C ± 50 and 0.6–0.7 GPa (Fig. 15b, 18a), suggest that they represent a former metamorphic sole (Wakabayashi and Dilek, 2003; Agard et al., 2016). Their mineralogy and estimated P-T conditions are similar to those described in Armenia (Rolland et al., 2009; Hässig et al., 2013), Egypt (Farahat, 2011), Albania (Gaggero et al., 2009) or Alaska (Harris, 1998) and range between granulite facies HT (i.e., clinopyroxene-garnet bearing soles; Soret et al., 2017) and greenschist facies LT soles. Since metamorphic soles mark the initiation of intra-oceanic subduction (e.g., Wakabayashi and Dilek, 2003; Agard et al., 2016; Plunder et al., 2016; Guilmette et al., 2018; Dubacq et al., 2019), their age is an important constraint for the geodynamic evolution of the Sistan orogen.

Three age populations were obtained for this metamorphic sole (Fig. 16d-k). The ca. 108 Ma age is undistinguishable from the one obtained for the 106 ± 3 Ma amphibolitized gabbro (Fig. 16a) and therefore interpreted as inherited from the oceanic activity. Five ages, obtained for samples collected in the vicinity of the large granitoid intrusions cross-cutting the metamorphic sole, cluster between ca. 52 and 55 Ma. These ages correspond within error to the ca. 50 Ma ages obtained for granitoids (Fig. 16l) and are thus interpreted as reflecting recrystallization of amphibole or titanite during the magmatic event. The two ~72 Ma ages (Fig. 16e-f), obtained by the two different methods on distinct samples, are inferred to date the peak of the metamorphic sole. This constrains the onset of intra-oceanic subduction and therefore the start of the obduction of the Neh Com-

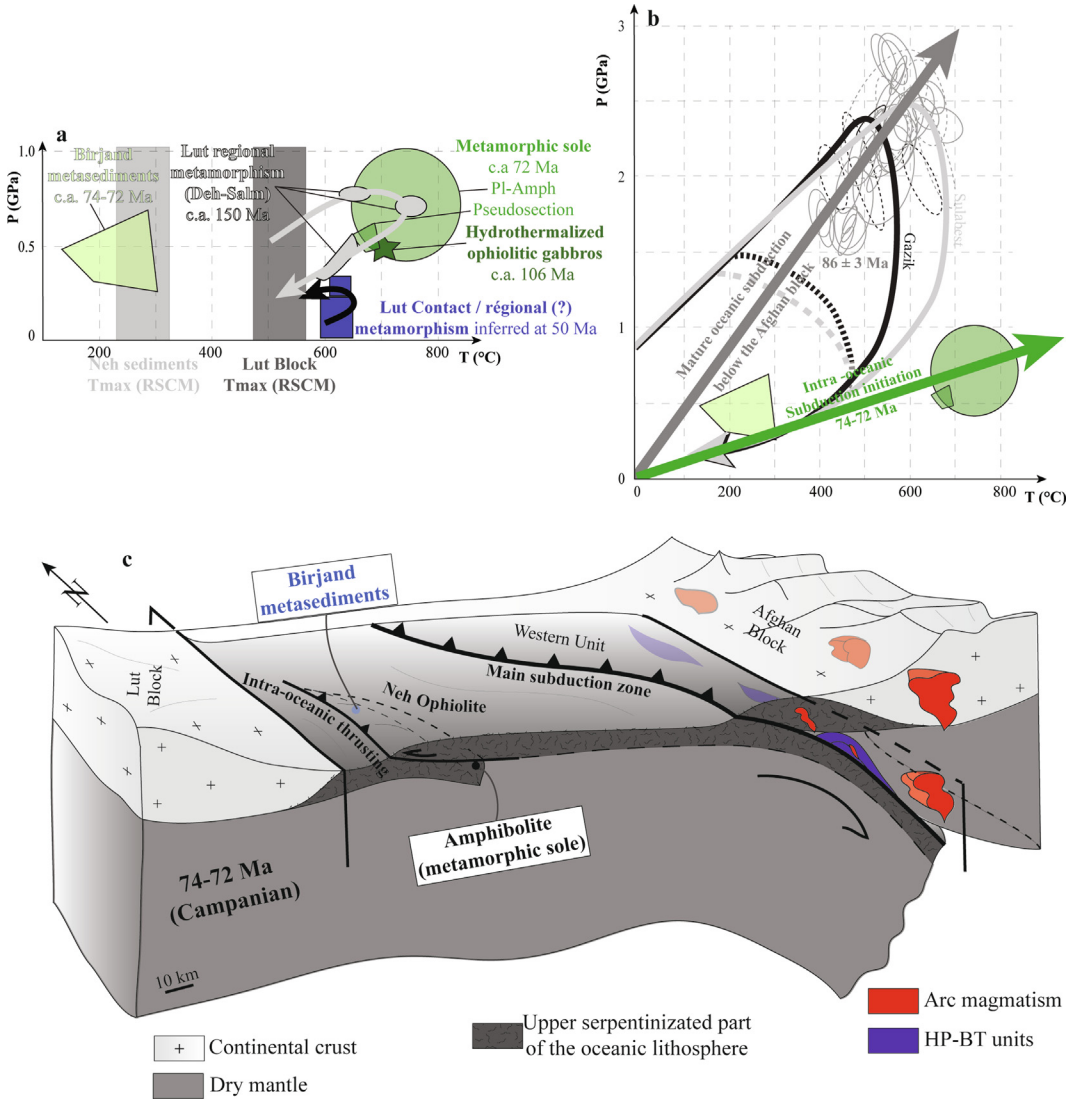

Fig. 18. Major metamorphic events associated with the Sistan orogeny. **a)** Results provided by this study; **b)** Comparison between the HP-LT metamorphism in the Ratuk complex (Fotoohi Rad et al., 2009, 2005; Angiboust et al., 2013; Bonnet et al., 2018;) and greenschist- to amphibolite-facies metamorphism in the Neh complex; **c)** 3D block diagram emphasizing the interpretation of the Neh complex metamorphic rocks: an asymmetric initiation of intra-oceanic thrusting/subduction around 74–72 Ma.

plex. This age lies between those for the Ratuk Complex eclogites (peaking at 86 ± 3 Ma; Bröker et al., 2013; Bonnet et al., 2018; Fig. 18b), and the closure of the Sistan oceanic realm at ~50 Ma (Fig. 16l).

The second type corresponds to lawsonite-bearing rocks that were found below the ophiolitic Unit 2, south of Birjand (Figs. 6, 8). Their P-T estimates lie at the transition between greenschist and blueschist facies (Fig. 15a, 18a). Further evidence for metamorphic recrystallization and equivalent burial is provided by the presence of phengite, spessartine-rich garnet, ferric blue amphibole, and Al-bearing pyroxene assemblage in nearby meta-cherts dated between 74.1 ± 0.3 Ma and 72.2 ± 0.3 (Fig. 16b, c). These ages are similar to the ~72 Ma ages obtained for the metamorphic sole.

These metamorphic rocks collectively provide evidence for a specific deformation event occurring within the Sistan Ocean during the Upper Campanian (Fig. 18c). We propose that this tectono-metamorphic event reflects the onset of intra-oceanic subduction and/or thrusting. If correct, its amplitude was larger in the S than in the N, as indicated by the presence of metamorphic soles and lawsonite-bearing samples, respectively. The presence of the lawsonite-bearing rocks can be used to estimate th thickness of the overlying ophiolitic material at around 12–15 km. We tentatively relate the presence of the intermediate temperature metamorphic soles and lawsonite-bearing rocks to the slow-spreading character of the Sistan ophiolite (as in Armenia): strain localization into a serpentinized mantle, mechanically weaker and cooler than that of a fast-spreading ocean, may have hampered the formation of HT metamorphic soles and promoted thrusting at shallower depths than for other obducted ophiolites (e.g., Oman: 15–20 km; Boudier et al., 1988; Rioux et al., 2016; Soret et al., 2017).

6.2.2. Lut Block: Contact metamorphism and regional metamorphism

In the N of the Lut Block, immediately S of the Neh Complex (Fig. 4), metapelitic rocks exibit two types of mineral assemblages (Fig. 10a-c). The most common assemblage contains quartz, biotite, plagioclase and andalusite equilibrated between 600 and 650 °C, at P lower than 0.3 GPa (Fig. 15c). These rocks are only slightly deformed and preserve some sedimentary layering, and are located near granitoid intrusions. This assemblage therefore likely reflects contact metamorphism and growth during granitoid emplacement at 49.6 ± 0.2 Ma (Fig. 16l). The second mineral assemblage comprises sillimanite overgrowing andalusite, white mica, plagioclase, biotite, and quartz, and reflects slightly higher P conditions (Fig. 15c). This second episode may reflect increased burial associ-

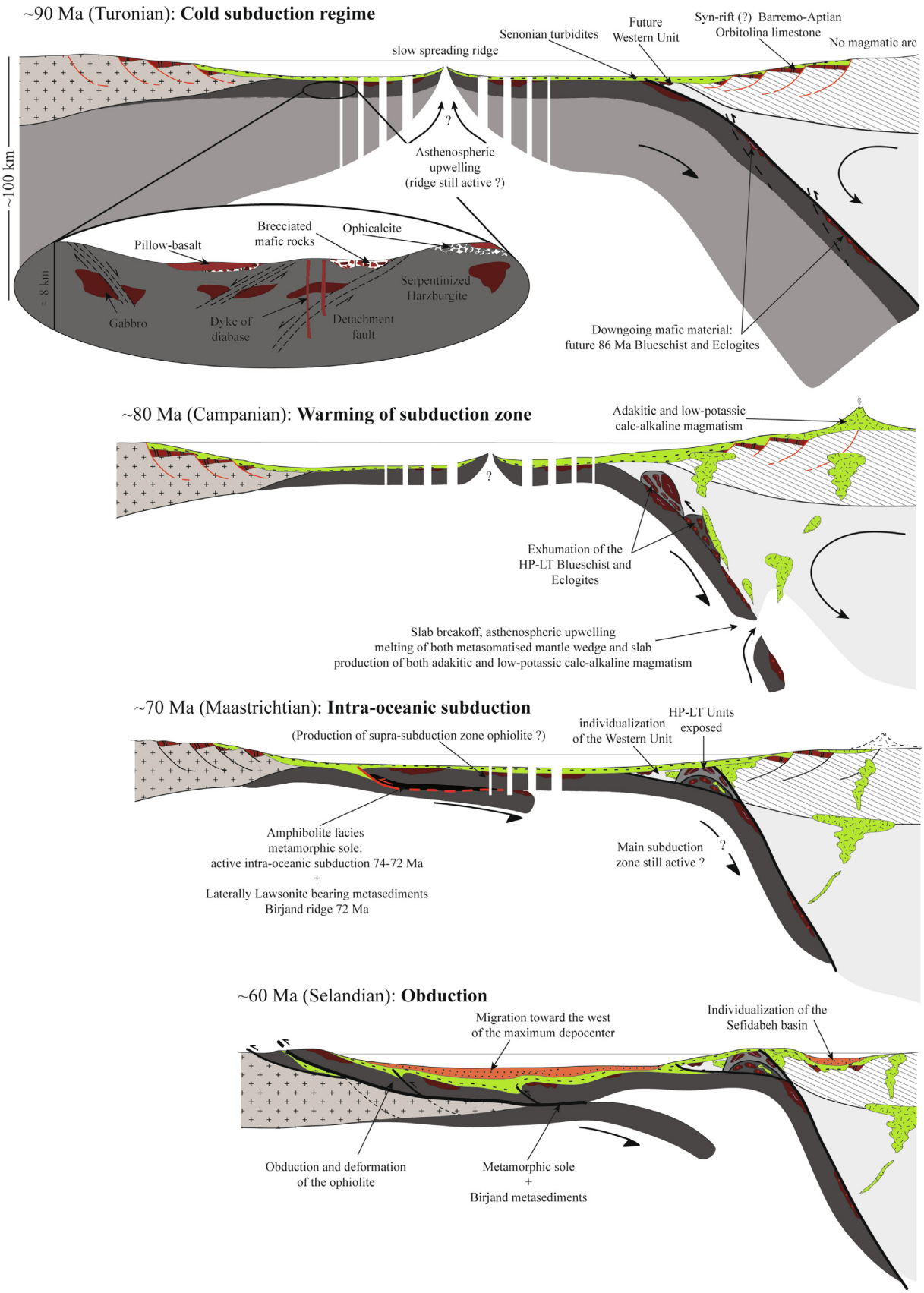

Fig. 19. Tectonic reconstruction from Turonian to present day of the North Sistan orogen along NNE-SSW profile (located on Fig. 4).

ated with collision. This interpretation is consistent with the development of a discrete greenschist facies schistosity in the granitoid intrusions, marked by sub-grain formation and rotation (Stipp et al., 2002). However, in the absence of age constraints for these metamorphic rocks, we cannot rule out the possibility that this metamorphism predates the granitoid intrusions, especially

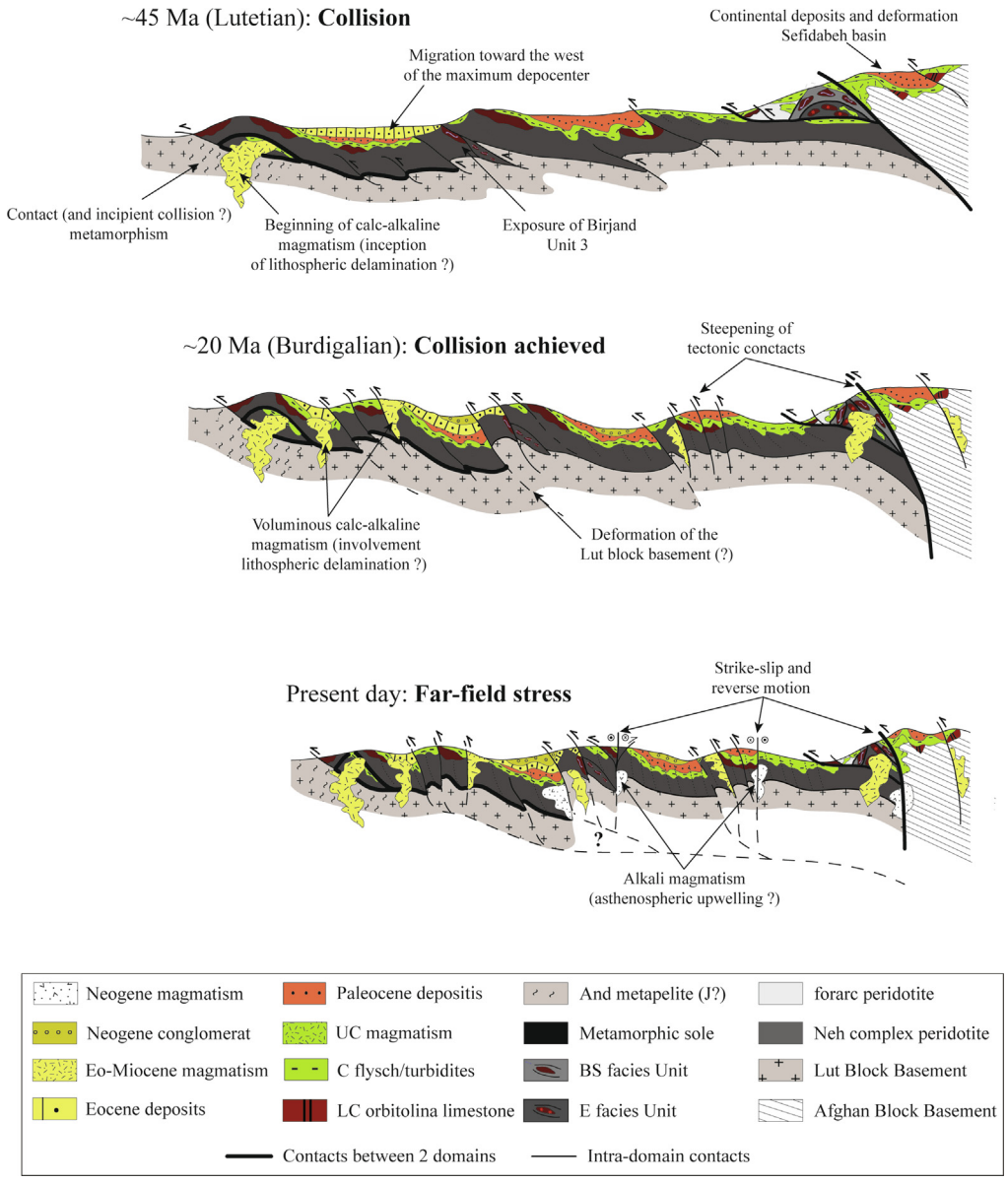

Fig. 19 (*continued*)

because of their similarity with some Jurassic metamorphic rocks of Anjul or Deh-Salm (Bröcker et al., 2014).

The Deh-Salm metamorphic complex exhibits amphibolite facies micaschists and migmatites, whose metamorphic evolution (Fig. 15d) and age (149.6 ± 0.5 Ma Ar-Ar age on biotite; Fig. 16m) resemble that described by Masoudi et al. (2006; the somewhat higher estimated pressure for sample 14–29a is consistent with the presence of kyanite). The protolith is inferred to be the Upper Triassic to Middle Jurassic siliciclastic Shemshak formation, which covered most of northern Iran after Paleotethys closure (Mahmoudi et al., 2010; Masoudi et al., 2006). This regional metamorphism was constrained between ca. 165 and 160 Ma (Mahmoudi et al., 2010), coeval with the ca. 165–163 Ma nearby granitic intrusions (Esmaeily et al., 2005; Mahmoudi et al., 2010), whose Nd and Sr isotopes signatures support derivation from partial melting of metasediments (Esmaeily et al., 2005). In this framework, our 149.6 ± 0.5 Ma Ar-Ar dating of biotite appears somewhat younger. Although further age determinations are needed, this plateau age precludes mixing of different biotite populations and thus seems to reflect a distinct thermal event. We propose that this ~150 Ma event either represents cooling of regional metamorphic rocks or, since age constraints on gabbros and radiolarites indicate that the Sistan Ocean was already open by ~125–110 Ma, a thermal event associated with the onset of rifting.

6.3. Tectonic evolution of the northern Sistan orogen

Based on our synthetic cross-section of the northern Sistan orogen (Fig. 17) and our tectono-metamorphic results (Fig. 18), as well as on the constraints from previous studies (summarized in Fig. 3), we propose a tentative reconstruction of the main geodynamic stages of the Sistan orogeny, from the onset of subduction to the present (Fig. 19).

The slow- to ultra-slow-spreading Sistan Ocean is opening from 125 Ma (and possibly earlier) to about 90 Ma. This allows to place crude constraints on the maximum ocean width, probably no larger than 600 km assuming a slow accretion rate < 2 cm/yr for ~30 Ma. Since 90 Ma at least (Fig. 19a; Bröcker et al., 2013; Bonnet et al., 2018), NE-dipping subduction of the Sistan Ocean below the Afghan margin (comprising the Western Unit and the Afghan Block) is

Table 1
Comparison between the main inner ophiolites of Iran.

Location	Name	Size (km^2)	Protolith ages (biostrat./ radiometric)	Structural organization	Mantle lithology	Crustal Lithology	Chemistry	Intepretation	Metamorphism	Intepretation	Post-ophiolite magmatism	Oldest unconformable sediments	References
E CEIM	**Sistan**	20,000	124–106 Ma	Kilometer scale slices	Harzburgite	Gabbroic intrusions Pillowed or massive basalts	N-MORB E-MORB OIB CA	Mid oceanic ridge activity; enriched mantle; SSZ	1) Amphibolite: 700 °C-0.65GPa 74–72 Ma; Lws bearing metasediments: 250 °C-0.4GPa 72 Ma 2) HP-LT rocks at 86 Ma	1) Metamorphic sole or latteral equivalent 2) Subudtion	1) CA and adakite Upper Cretaceous 2) CA Eo-Oligocene 3) Alcaline Miocene	Eocene conglomerate or sandy-limestone	Delaloye and Desmons, 1980 Saccani et al., 2010 Zarrinkoub et al., 2012 Pang et al., 2012 Pang et al., 2013 This study
NW CEIM	**Sabzevar; Torbat-e-Heydarieh**	7,000	Late Jurasic; 101–75 up to 52.4 (?) Ma	Kilometer scale slices and colored mélange	Harzburgite Wherlite	Gabbros Dykes of diabase Basaltic lavas	N-MORB E-MORB OIB IAT CA	SSZ	1) Blueschist: 420–500 °C 1.3–1.55 GPa 54–51 Ma; 2) Granulite: 780 °C-1.1–1.2 GPa 105 Ma	1) Blueschist subduction related (age?) 2) Granulite: metamorphic sole	CA and adakite at 45 Ma (flare up?) High Silica Adakite at 58 Ma (partial melting of slab, age?)	Eocene nummulitic limestone	Lindenberg and Groler, 1984 Ghazi et al., 2004 Nasrabady et al., 2011 Khalatbari Jafari et al., 2013 Moghadam et al., 2014 Rossetti et al., 2014 Moghadam and Stern, 2015 Omrani, 2017 Kazemi et al 2019 Mazhari et al., 2019
SW CEIM	**Nain; Ashin**	600	145–67 Ma or older up to 188 Ma (?)	Small tectonic slices and colored mélange	Harzburgite Lherzolite Dunite	Gabbro Dykes of diabase massive and pillowed basalt	N-MORB IAT CA	SSZ	Amphibolite 113 Ma	Metamorphic sole	CA Cenozoic	Paleocene limestone	Sharkovski et al., 1984 Ghazi et al., 2004, 2012 Moghadam et al., 2009, 2013 Shirdashtzadeh et al., 2015, 2020 Moghadam and Stern, 2015 Pirnia, 2020
SW CEIM	**Deshir; Shahr-e-Babak**	150	101–67	Small tectonic slices and colored mélange	Harzburgite Lherzolite Pyroxenite	Gabbro Dykes of diabase Massive and pillowed basalt	N-MORB IAT CA	SSZ			CA Cenozoic	Maastrichtian limestone	Ghazi et al., 2004 Moghadam et al., 2009, 2010 Moghadam and Stern, 2015
SW CEIM	**Balvard; Baft; Esfandagheh**	3,000	103–72	Small tectonic slices and colored mélange	Harzburgite	Gabbro Dykes of diabase Basaltic lavas	E-MORB CA IAT	SSZ			CA Cenozoic	Maastrichtian limestone	Moghadam et al., 2009, Moghadam and Stern, 2011, Moghadam et al., 2013 Moghadam and Stern, 2015
N Makran	**Band-e-Zeyarat; Dar Anar**	20,000	145–111	Kilometer scale slices	Harzburgite	Gabbro Dykes of diabase Pillowed basalt	N-MORB E-MORB	SSZ	Blueschist: 300–380 °C 0.9–1.4 Gpa 100–95 Ma CCW PT path	Blueschist: cold subduction related regime after amphibolitic metamorphism		Maastrichtian limestone	Ghazi et al., 2004 McCall, 1997, 2002 Hunziker et al., 2015, 2017 Omrani, 2017 Burg, 2018 Sepidbar et al., 2020
N Makran	**Fannuj; Maskutan**	2,800	<140	Kilometer scale slices	Lherzolite Harzburgite	Gabbro Dykes of diabase Basaltic lavas	IAT (S) E-MORB (N)	SSZ				Maastrichtian limestone	McCall, 1997, 2002 Hunziker et al., 2015 Burg, 2018 Saccani et al., 2018 Sepidbar et al., 2020

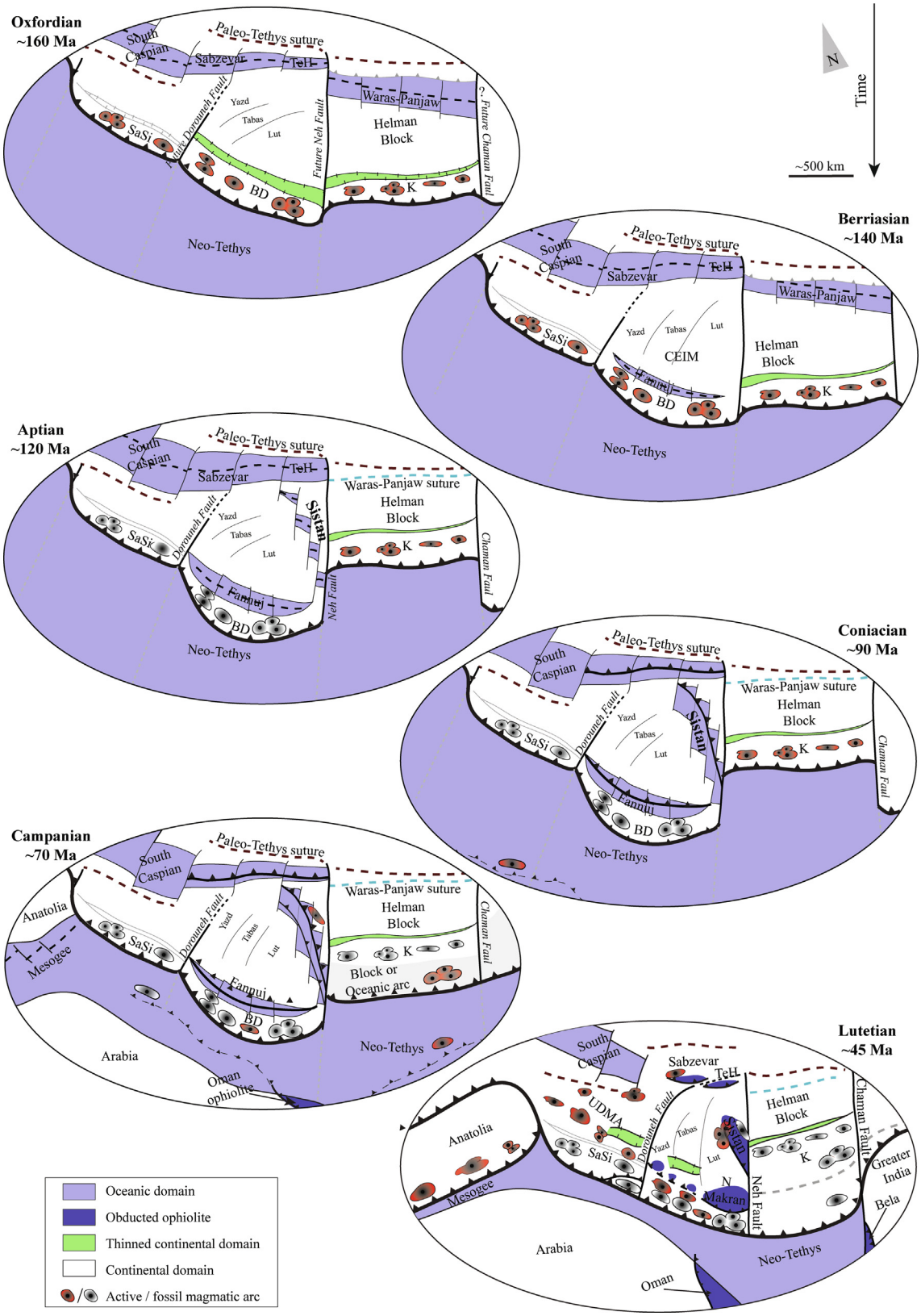

Fig. 20. Tectonic evolution of the Sistan in the Tethyan realm from Late Jurassic to Eocene. BD: Bajgan-Durkan; K: Kandahar; TeH: Torbat-e-Heydarieh; SaSi: Sanandaj-Sirjan.

active and leads to the disappearance of the oceanic domain. Subduction is responsible for the flexural subsidence associated to the deposition of Senonian turbidites (see Appendix A), for the formation and later exhumation of blueschists and eclogites at 86 ± 3 Ma (Fig. 19b; Bonnet et al., 2018 and references therein), and for the emplacement of low-K calc-alkaline and adakitic arc magmatism mainly in the Sefidabeh basin (Jentzer et al., 2020).

Between 74 and 72 Ma (Figs. 18c, 19c), a NE-dipping intra-oceanic subduction/thrusting develops, as documented by the formation of a metamorphic sole, which ultimately leads to the obduc-

tion of the Neh Complex. At the same time Maastrichtien conglomerates are being deposited on top of the already exhumed HP-LT metamorphic rocks. By then, the exposure and doming of the HP-LT rocks appears to have separated the Western Unit from the rest of the Afghan continental margin. Two separate basins start forming: the Sefidabeh basin, and the one on top of the Neh Complex, whose depocenter progressively migrates south-westward.

The obduction of the Neh ophiolite onto the continental Lut Block is largely completed by 50 Ma, as attested by the age of the granitoid intrusion. The onset of collision, which must therefore have started during the Late Paleocene and/or Early Eocene, is marked by a drastic change in sedimentation. The collision-related horizontal shortening is only moderate (~30–50 km) and rather short-lived (<~20 My), since Oligocene deposits are only slightly deformed. Later, post-collisional shortening is limited (~10–20 km) and associated with far-field stresses from the Zagros collision zone (Jentzer et al., 2017 and references therein). Primary contacts, steepened by later deformation, are used as pathways by the Plio-Quaternary alkaline magmatism.

6.4. Tectonic significance of the Sistan orogen within the Neotethyan realm

The Sistan ophiolite differs from the other inner Iranian ones (Table 1; Shafai Moghadam and Stern, 2015) in that it is the only one exposing subduction-related HP-LT metamorphic rocks and arc magmatic rocks, km-thick unmetamorphosed slices of ophiolite from a former slow-spreading ocean and extensive metamorphic soles. A qualitative paleotectonic reconstruction is proposed below (Fig. 20) to account for those differences and for the better preservation of the oceanic fragments. It is then set back within the larger frame of the Neotethyan realm, notwithstanding large uncertainties on the initial orientation of the Sistan Ocean.

During the Mid-Jurassic, at ~175 Ma, following Paleotethys closure and inception of the Neotethys subduction at ~200 Ma, a magmatic arc starts forming along the Sanandaj-Sirjan and Bajgan-Durkan domains (Fig. 20a; e.g. Stampfli and Borel, 2002; Agard et al., 2011; Seton et al., 2012; Burg, 2018). Fragmentation of the upper plate starts in the Mid-Jurassic to the E of the future Sistan domain, with the opening of the back-arc Waras-Panjaw basin, which separates the Band-e Bayan and Helmand Blocks. A similar yet slightly younger (Mid- to Late Jurassic) evolution affects the Iranian region, as shown by the opening of the South Caspian basin, possibly extending eastward into the Sabzevar and Torbat-e-Heydarieh, and by the existence of extensional movements in the Kopeh-Dagh (Stöcklin, 1974; Brunet et al., 2003; Robert et al., 2014; Omrani, 2017). To the S of the CEIM, the magmatic evolution advocates for back-arc extension at the rear of the Neotethyan subduction zone, in the future Makran region (Hunziker et al., 2015; Burg, 2018), in the Kandahar basin (Siehl, 2017) and possibly along the Sanandaj-Sirjan zone (Azizi and Stern, 2019).

During the Early Cretaceous (Fig. 20), the Fannuj ocean starts forming between the CEIM and Bajgan-Durkan, coincident with dominantly extensional tectonics (e.g. Pirnia, 2020; Sepidbar et al., 2020), and extends to the NW into the future Nain-Baft domain, up to the Dorouneh-Great Kavir fault which was active at the time (e.g. Mattei et al., 2015). In contrast, on the Afghan side, the Waras-Panjaw ocean is progressively closing (Montenat, 2009), while the Sistan Ocean starts forming. In order to explain the contrasting evolution between the Lut and Afghan transects, as well as the present-day N-S orientation of the Sistan Ocean, we propose that its formation results from the existence of an oblique transtensional setting (Fig. 20c).

Between 115 and 85 Ma (Fig. 20d), the Arabia-Eurasia convergence rate steadily increases and changes orientation (e.g. Agard et al., 2006; DeMets et al., 2010; Matthews et al., 2012). The subsequent geodynamic reorganization leads to the initiation of intra-oceanic subduction in the S of the Neotethys at 105–95 Ma, and to the formation and emplacement of several ophiolites and intra-oceanic arcs (i.e. Guilmette et al., 2018; Bonnet et al., 2020; Rodriguez et al., 2020, 2021). We propose that these kinematic changes triggered the onset of closure of the Iranian marginal basins: to the N, the metamorphic evolution in the Sabzevar domain (through the presence of granulites similar to metamorphic soles; Rossetti et al., 2010) likely advocates for the onset of subduction, and the Waras-Panjaw ocean is closed (Montenat, 2009; Siehl, 2017). In the Nain-Baft domain, metamorphic soles marking the initiation of an intra-oceanic subduction were dated at 100–90 Ma (Moghadam et al., 2009). In the S, in the Makran region, arc magmatism is still active and blueschists are exhumed at 100–95 Ma (Burg, 2018), as along the southern Sanandaj-Sirjan zone (Agard et al., 2006; Angiboust et al., 2016). In the Sistan region, peak burial of blueschists and eclogites at ~86 Ma (Bröcker et al., 2013; Bonnet et al., 2018) indicates that subduction was active since a few million years at least.

During the Campanian (~75 Ma; Fig. 20e), most of the Iranian marginal basins are actively closing. The Sistan ocean records the onset of intra-oceanic shortening at ~73 Ma, contemporaneous with the northward migration of India, with changes in subduction dynamics and with obduction marked by the emplacement of the Masirah, Muslim Bagh, Bela and Spontang ophiolites (Corfield et al., 2001; Festa et al., 2019; Gaina et al., 2015; Gnos et al., 1997; Mahmood et al., 1995).

The Sistan Ocean, possibly due to its central location in the Neotethyan realm, therefore recorded the plate reorganizations at 100–90 Ma and 75–70 Ma, which led to the main obduction events in the Neotethys (Gnos et al., 1997; Agard et al., 2007; Gaina et al., 2015). To the E of the Sistan domain, several magmatic arcs (Kandahar, Chagai Hills; Ras Koh, where small ophiolitic remnants are also found) may represent accreted forearcs or lateral equivalents of the microcontinental Kabul Block (Siehl, 2017; Burg, 2018). Maastrichtian sediments unconformably overlying the Ras Koh, Makran, Baft and Deshir ophiolites indicate that these had been obducted by then (the later Paleocene sediments in the Nain ophiolite may indicate diachronous closure, younging towards the NW; Table 1).

During the Lower Eocene, the obduction of the Sistan (this study) and Sabzevar ophiolites is completed (Bröcker et al., 2021) and all Iranian marginal basins are closed, except for the South Caspian basin. From the Eocene onwards, calc-alkaline magmatism affects most of Iran, along the Urumieh–Dokhtar arc, from the Alborz to Kopeh Dagh, and in the Lut Block. This episode reflects large-scale distributed extension triggered by lithospheric delamination and/or Neotethyan slab retreat (Omrani et al., 2008; Agard et al., 2011; Verdel et al., 2011; Rossetti et al., 2014).

7. Conclusions

Our tectonic, petrological and radiochronological data reveal that the closure of the Sistan Ocean proceeded through two major NE-dipping subduction zones. The first one developed below the Afghan margin from at least 90 Ma onwards, as shown by the presence of HP-LT metamorphic rocks, arc-magmatism and flysch deposits. It was coeval with the 105–85 Ma kinematic changes that affected the western part of the Tethyan realm. An additional NE-dipping intra-oceanic thrusting developped after 73 Ma, as shown

by the presence of extensive metamorphic sole rocks at the base of the ophiolite. This second event coincided with regional-scale geodynamic changes and ophiolite emplacement in the eastern part of the Tethyan realm between 75 and 65 Ma, when India started migrating northward. With its central position in the Tethyan realm, the Sistan domain therefore appears to have echoed the main geodynamic reorganizations experienced by the Neotethys.

Our results indicate that, following intra-oceanic subduction, obduction of the unmetamorphosed Neh ophiolite onto the Lut Block was achieved by ~50 Ma. The ensuing collision was short-lived (~20 Myr) and limited, with at most 40 km of shortening and no significant deformation of the basement. Results also indicate that the Sistan Ocean was a slow-spreading one, with a maximum width of about 600 km. Using available paleogeographic constraints, we propose that the Sistan Ocean opened in a transtensional setting controlled by the contrasting slab dynamics between the Iranian and the Afghan transects of the Neotethys subduction zone.

Declaration of Competing Interest

The authors declare that they have no known competing financial interests or personal relationships that could have appeared to influence the work reported in this paper.

Acknowledgements

We feel indebted to the Geological Survey of Iran, and especially to Dr. Shahidi, to the geologists and all the staff (drivers, cooks, and chief of camp) for their kindness, constant support and for enabling us to visit the region since 2014. This work was financially supported by the CNRS-INSU programs, by ISTeP lab of Sorbonne University and by the over-head of the project "Zooming in Between Plates" (Marie Curie International Training Network of the European Union's Seventh Framework Program FP7/2007/2013/ under REA grant agreement no. 604713). We would like to warmly thank Eric Delairis who produced the thin sections studied; Omar Boudouma for his help during SEM sessions; Michael Fialin and Nicolas Rividi for their technical support during microprobe analyses, and Andrew Kylander-Clark for support with LASS analyses. Main thanks to Eric Barrier for taking the time to discuss tectonic reconstructions. G.B. was financially supported (2019-2020) by the NSF partnership for international research and education EFIRE (OIA 1545903), with additional funding from UCSB and NSF for LASS analyses. Bradley Hacker is warmly thanked for his overall support.

Appendix A. Logs of the Sefidabeh basin and the Neh Complex

Appendix B. Analytical methods

B.1. Mineral chemistry

The electron microprobes used for this study were Cameca SX-5 and SX-100 at Camparis (Sorbonne Université, 4 place Jussieu, 75,005 Paris, France). Point measurements were made in classical analytical conditions (15 kV acceleration voltage and 10 nA beam current allowing ~2 μm beam size in wavelength-dispersive spectroscopy mode) using diopside (Ca, Mg, Si), $MnTiO_3$ (Mn, Ti), orthoclase (K, Al), Fe_2O_3 (Fe), albite (Na) and Cr_2O_3 (Cr) as standards for calibration of elements indicated in parentheses. Elemental mapping has been carried out with identical voltage and an increased current (100 nA) with a counting time of 100 ms per point. Analyses were calibrated with the manufacturer's software using standards as point analyses (Pouchou and Pichoir, 1991). All analysis was sorted based on their structural formulae calculated with Fe^{3+} estimates using the method of Droop (1987) for garnet and clinopyroxene, and the method exposed in Leake (1997) for amphibole. We considered all iron as ferric in epidote and lawsonite, and as ferrous in mica.

B.2. RAMAN spectroscopy and mineral determination

RAMAN spectroscopy on polished thin sections was used to identify the serpentine and the carbonate minerals. Following Schwartz et al, (2013), the spectral regions investigated to characterize serpentine species are from 150 to 1150 cm^{-1} and from 3600 to 3720 cm^{-1} because they include the lattice vibrational modes and the OH stretching mode region. The nature of carbonate material was determined using the spectral region between 600 and 800 cm^{-1} as indicated in Kontoyannis and Vagenas (2000).

B.3. Thermometric methods used

B.3.1. Raman spectroscopy on carbonaceous material: Tmax estimation

The Raman spectra of carbonaceous materials (RSCM) between 1100 and 1800 cm^{-1} can exhibit a characteristic graphitic band at ~1580 cm^{-1} and four defect bands at ~1200 (D4), ~1350 (D1), ~1500 (D3) and ~1620 (D2) cm^{-1}. The increase of temperature during diagenesis and metamorphism induces a progressive and irreversible loss of the defect bands, thus for a temperature > 655 °C, all the organic matter is changed into pure graphite. Nowadays, several calibrated methods using Raman spectra allow to quantify the maximum temperature (Tm) reached by the carbonaceous materials (CM) between 150 °C and 655 °C with an intrinsic error of ± 50 °C (Beyssac et al., 2002; Lahfid et al., 2010; Kouketsu et al., 2014). In this study, we used for Tm ≥ 330 °C the calibration from Beyssac et al. (2002) and the calibration from Lahfid et al. (2010) for Tm < 330 °C.

Raman spectra were collected with a Raman microspectrometer (Renishaw inVia located at the ENS and at the IMPMC, both in Paris, France) on conventional petrographic thin sections. Textural position of the CM was carefully checked and the focus was made beneath the surface of a transparent adjacent grain to limit some potential parasitic effects. Analysis was performed in the center of the carbonaceous particles, using argon laser beam (514 nm, Spectra-Physics) equipped with a LEICA 50 × magnification objective (0.5 numerical aperture) and using a circular polarization of the laser. The Raman scattered light was dispersed by wavelength using a holographic grating with 1800 lines/mm and detected by a CCD camera. The spectra were recorded in the 700 to 2000 cm^{-1} range (first-order spectrum). For each sample between 11 and 20 coherent Raman spectra were obtained.

B.3.2. Ti in biotite: empirical thermometry

For metapelitic rocks saturated in Al, in Ti, and in Si (aluminosilicate, rutile or ilmenite and quartz-bearing rock) and for biotite with XMg ≥ 0.275 and 0.04 < Ti < 0.6 apfu, the incorporation of Ti in octahedral sites of biotite depends on temperature. Henry (2005) proposed an empirical function linking Ti in biotite and temperature as defined in equation (A) with an uncertainty of ± 24 °C. This relationship can be used between 0.3 and 0.6 GPa and 480 to 800 °C. Presence of CM in the rock is recommended to use this geothermometer because CM buffers the oxygen and limits the formation of Fe^{3+}.

$$T = \left(\frac{\ln(Ti) - a - c(XMg)3}{b}\right)0.333 \quad (A)$$

Where T is temperature in °C, Ti is the Ti content of the analysed biotite in apfu, XMg of the analysed biotite and a, b and c three adjustment coefficients respectively defined as:

a = −2.3594, b = 4.6482 10^{-9} and c = −1.7283.

B.4. Thermobarometric methods used

B.4.1. Plagioclase-amphibole

Holland and Blundy (1994) proposed an edenite-richterite thermometer (edenite + albite = richterite + anorthite), based on the exchange (Na Si)-(Ca Al) between amphibole and plagioclase as described in the equation B. This method can be used over a broad range of bulk rocks composition (with or without quartz), in a range of 400 to 1000 °C and 0.1 to 1.5 GPa with an uncertainty around ± 40 °C.

$$T = \frac{78.44 + Yab - an - 33.6\,XM4Na - (66.8 - 2.92P)XM2Al + 78.5XT1Al + 9.4XANa}{0.071 - R\ln\left(\frac{27\,XM4Na\,XT1Si\,Xplan}{64\,XM4Ca\,XT1Al\,Xplab}\right)} \quad (B)$$

Where the $Y_{ab\text{-}an}$ term is given by: for Xab > 0.5 then $Y_{ab\text{-}an}$ = 3 kJ otherwise $Y_{ab\text{-}an}$ = 12.0 ($2X_{ab}$ − 1) + 3 kJ, T is the temperature in Kelvin, P is the pressure in kbar and the $X^{\Phi i}$ terms denote the molar fraction of species (or component) i in phase (or crystallographic site) Φ.

Molina et al. (2015) proposed a barometer using the Al-Si partitioning between plagioclase and Ca-amphibole as described in equation (C). This method can be used over a broad range of bulk rocks composition (with or without quartz) but only with amphibole containing>0.02 apfu of Ti and>0.05 apfu of Al_{VI}, in a range of 650 to 1050 °C and 0.15 to 0.23 GPa with an uncertainty ≤±0.2 GPa.

$$P = \frac{8.3144\,T\ln Dpl/amphAl/Si - 8.7\,T + 23\,337\,XT1Al + 7\,579\,Xab - 11\,302}{-274} \quad (C)$$

Where $Dpl/amph_{Al/Si}$ = (Xpl_{Al}/Xpl_{Si})/($Xamph_{Al}/Xamph_{Si}$): molar plagioclase/amphibole Al-Si partition coefficient, T is the temperature in Kelvin, P is the pressure in kbar and the $X^{\Phi i}$ terms denote the molar fraction of species (or component) i in phase (or crystallographic site) Φ.

Using both B and C equations for Ca-amphibole and plagioclase bearing metamorphic rocks, P-T conditions can be estimated between 650 and 1000 °C and 0.1 to 1.5 GPa with an uncertainty of ± 40 °C and ± 0.2 GPa.

B.4.2. Ti-Al amphiboles

In meta-basaltic rocks saturated in Ti, Al, and Ti content of Ca-amphibole can be used to estimate semi-quantitatively P-T conditions (Ernst and Liu, 1998). This method was tested for natural and experimental samples on a range of temperature between 400 and 1100 °C and a range of pressure between 0 and 2.2 GPa but the best fit between this method and independent P-T estimations were obtained for low-grade metamorphism. Amphibole isopleths do not seem to be affected by small variations in bulk rocks composition. During cooling, the exsolution in amphibole of rutile, titanite or ilmenite which are Ti bearing phases can lead to an underestimation of the Ti content of the amphibole and must be considered.

B.4.3. GB and GBAQ: empirical thermobarometry

Wu (2017) proposed a garnet–biotite–aluminosilicate–quartz (GBAQ) geobarometer which can be used for a broad garnet and biotite composition and under P–T conditions from 450 to 950 °C and from 0.1 to 1.7 GPa with a random error inferred to be around ± 0.18 GPa. This geobarometer needs to be used the type of aluminosilicate bearing in the rock and an estimated temperature which is obtained by the geothermometer garnet-biotite (GB) from Holdaway (2000). In this method, the temperature is calculated with an estimated uncertainty of ±25 °C, using the Fe-Mg partition coefficient between garnet and biotite and an estimation of pressure. GBAQ geobarometer and GB geothermometer can be simultaneously applied to iteratively estimate metamorphic P–T conditions. These methods are applied only for low value of ferric iron in biotite (around 11 ± 3 mol%) which can be buffered by ilmenite and/or graphite in the rocks. For samples without aluminosilicate, only GB geothermometer was used.

B.4.4. Thermodynamic modelling

Pseudosections were calculated using Perple_X (6.8.6 version, Connolly, 2005, 1990). with the internally consistent thermodynamic dataset and equation of state of H_2O used come from Holland and Powell (2011), the useful solution models and the bulk rocks composition here obtained after crushing, dissolution and ICP-OES iCap 6500 analysis performed in Nancy CRPG (results on Supplementary Table 4). For metabasite sample (15b-15c), the system used was Na_2O–CaO–K_2O–FeO–MgO–Al_2O_3–SiO_2–H_2O–TiO_2 and the solution models considered were: amphibole, augite, and melt with thermodynamic properties from Green et al. (2016), garnet, orthopyroxene, white mica, biotite, chlorite, and ilmenite with thermodynamic properties from White et al. (2014), Holland and Powell (2011) for epidote, White et al. (2002) for titanite and Holland and Powell (2003) for feldspar. The amount of water was chosen at 1 wt%. All the iron was considered as ferrous. For metapelitic samples (14-29a and 16–72) the system used was Na_2O–CaO–K_2O–FeO–MgO–MnO–Al_2O_3–SiO_2–H_2O–TiO_2 and the solution models considered were: garnet, chloritoid, staurolite, white mica, biotite, chlorite, ilmenite and melt with thermodynamic properties from White et al. (2014), Holland and Powell (2011) for epidote and Holland and Powell (2003) for feldspar. The amount of water was chosen at 2.5 wt% for sample 14–29a and 2 wt% for sample 16–72. All the iron was considered as ferrous. By minimizing Gibbs free energy, the software calculates for each desired P-T conditions the stable mineralogical assemblage and the composition of each solid solution. These models were compared to the natural mineral compositions obtained by microprobe analysis to estimate the P-T conditions of the mineral assemblages of our samples.

B.5. Geochronology methods

B.5.1. Ar-Ar

Samples were carefully chosen for dating so that: they bear minerals with enough K to be dated with the Ar–Ar method (white mica, biotite or amphibole) and these minerals constitute a well-understood paragenesis in the rock. Selected samples were crushed and sieved; single grains were handpicked under binocular microscope and cleaned in ultrasonic bath with acetone and distilled water. They were packaged in Al foils and irradiated for 40 h in the core of the Triga Mark II nuclear reactor of Pavia (Italia) with several aliquots of the Taylor Creek sanidine standard (28.34 ± 0. 28 Ma; Renne et al., 1998) as flux monitor. Argon isotopic interferences on K and Ca were determined by irradiation of KF and CaF_2 pure salt. Argon analyses were performed at Géosciences Montpellier (France) with an analytical device that consists of: (a) an IR-CO_2 laser of 100 kHz used at 5–15% during 60 s, (b) a lenses system for beam focusing, (c) a steel chamber, kept at 10^{-8}–10^{-9} bar, with a drilled copper plate, (d) an inlet line for purification of gases including two Zr–Al getters, (e) a multi-collector mass spectrometer (Argus VI from Thermo-Fisher). A custom-made software controls the laser intensity, the timing of extraction/purification and the data acquisition. To measure the Ar background within the sys-

tem, one blank analysis was performed every three sample analyses. ArArCalc© v2.5.2 was used for data reduction and plotting. The one-sigma errors reported on plateau ages, isochron and total gas ages include the error on the irradiation factor J. Atmospheric ^{40}Ar was estimated using a value of the initial $^{40}Ar/^{36}Ar$ of 295.5.

B.5.2. U-Pb in titanite

In situ U-Pb analyses of titanites were performed by laser ablation split-stream inductively coupled plasma mass spectrometry (LASS ICP-MS, Kylander-Clark et al., 2013) at the University of California, Santa Barbara. Samples were ablated using a Photon Machines 193 nm ArF ultraviolet laser with a laser fluence of ~1 $J.cm^{-2}$, and U-Pb isotopes and trace elements were analysed simultaneously on the same 35 μm spots, using a Nu Instrument Plasma 3D multi-collector inductively coupled plasma mass spectrometer (MC-ICP-MS) and an Agilent 7700X quadrupole inductively coupled plasma mass spectrometer (Q-ICP-MS), respectively. The laser was fired twice at 50% power to remove surface contamination and this material was allowed to wash out for 15 s. Samples were then ablated at 4 Hz for 15 s with a laser energy of 1 $J.cm^{-2}$. Analyses of unknowns were bracketed by analyses of matrix-matched titanite standard MKED (1518.87 ± 0.31 Ma isotope dilution thermal ionization mass spectrometry date; Spandler et al., 2016), which was used as a primary standard for U-Pb analyses. Secondary titanite standards BLR (1047.1 ± 0.4 Ma concordia date; Aleinikoff et al., 2007), FC (28.395 ± 0.049 Ma Concordia date; Schmitz and Bowring, 2001) and Y17 (388.6 ± 0.5 Ma isotope dilution thermal ionization mass spectrometry data; Spencer et al., 2013) were included to monitor accuracy and internal error. We obtained ^{207}Pb-corrected $^{206}Pb/^{238}Pb$ ages (using Stacey-Kramers common Pb correction in IsoplotR; Vermeesch, 2018) of 1033.41 ± 3.43 Ma for BLR (n = 17), 27.99 ± 0.14 for FC (n = 10), and 391.94 ± 1.71 Ma for Y17 (n = 11). These ages are accurate to within 1.3%, 1.4% and 0.8% of standard values, respectively.

All unknowns were additionally bracketed by analyses of international glass standard NIST612, that was used as a primary standard for trace elements (Pearce et al., 1997), using ^{44}Ca as the internal standard element (assuming 19.2 wt% Ca). The spectra were reduced using Iolite v2.5 (Paton et al., 2011), error correlations were recalculated after Schmitz and Schoene (2007), and discordia ages were calculated using IsoplotR (Vermeesch, 2018).

Appendix C. Mineral chemistry

Microprobe analysis are available in SM 2.

C.1. Ophiolitic rocks

Microprobe analyses were performed in serpentinized peridotite and gabbro (Supplementary Table 3). In gabbros, clinopyroxene compositions are close to augite, while amphibole compositions range from actinolite to tschermakite but are mainly Mg-hornblende; plagioclase is > 88 mol% albite. Serpentinized peridotites contain enstatite, amphibole (mostly tremolite or edenite, but with some Mg-hornblende) and olivine close to the forsterite endmember.

C.2. Birjand metasediments

Results for three metachert samples (Fig. 13a) show that blue amphibole is riebeckite ($Na_B \geq 1.5$, $(Na + K)_B < 0.5$; XMg < 0.5; $Fe^{3+}/(Fe^{3+}+Al) > 0.5$; Si between 7.5 and 8). White micas are phengitic with Si between 3.05 and 3.6 and XMg between 0.35 and 0.6. Garnet is manganese-rich (≥38% of spessartine endmember). Clinopyroxene from sample 15b–19 corresponds to omphacite. Chlorite is close to the clinochlore end-member (≥75%) with Si between 2.75 and 3.15 and XMg from 0.4 to 0.85. The only primary minereals are quartz and feldspar which is pure albite in sample 15b–19.

The studied metagabbroic clasts show that clinopyroxene lies between the aegyrine-augite and omphacite fields. Plagioclase is pure albite. Chlorite is clinochlore with Si between 2.85 and 3.175 and XMg from 0.45 to 0.9. Serpentine from the adjacent metaophicalcite (sample 16–21b), determined through Raman spectroscopy corresponds to lizardite. Likewise, the nature of the carbonate matrix of the ophicalcite (16-21b) was determined to be calcite.

C.3. Amphibolite

Microprobe analyses were performed on twelve amphibolites and one metasediment (14–07; Fig. 13b). Amphibole is calcic and corresponds to Mg-hornblende, except for some crystals trending towards the tschermakite or tremolite end-members. XMg ranges between 0.4 and 0.85. While the composition is fairly homogeneous in each sample, a wide range of compositions is observed from one sample to the other yet without clear spatial correlations between samples from the NE (Sahlabad) to the S (Barak). Feldspar is dominantly plagioclase, most commonly around 65% albite, yet spanning the full range of compositions (from 94% anorthite to 98% albite). Four samples contain minor amounts of K-feldspar.

Pyroxene is diopsidic in the four analysed samples (14-11b, 14–20, 14-26a, and 17–18), except in sample 14–20 where it is richer in Al and Na and poorer in Ca (i.e., with an augitic composition close to that of sample 16–01c). Garnet (sample 14–11b) is intermediate between grossular and andradite. White mica is phengitic close to the muscovite pole, with Si varying between 3.1 and 3.2 in the metasediment (with XMg ~ 0.6). In amphibolites, Si varies from 3.2 to 3.4 and XMg from 0.45 to 0.85. Biotite (14–18) has a XMg of 0.65 and Si of 2.8. Epidote is close to the ferric endmember. Chlorite is close to clinochlore composition.

Trace element composition of titanites, in particular the Zr content, was obtained via laser ablation split-stream inductively coupled plasma mass spectrometry. Mean values of the Zr content range between 110 and 185 ppm (14–09: 154 ppm, for a 114–216 range; 14–18: 111 ppm, 42–192 range; 16–42: 158 ppm, 35–460 ppm range; 17–18: 184 ppm, 80–339 ppm range).

C.4. Metamorphic rocks of the Lut Block

Biotite hasa XMg ranging between 0.35 and 0.5 and Si between 2.5 and 2.9 (Fig. 13c), with homogeneous composition in each of the three studied samples. Other minerals correspond to endmemeber compositions of albite, muscovite, almandine (sample 16–74). Chlorites are clinochlore. Andalusite is partially replaced by sillimanite. Andalusite is stable with garnet (for 16–74, Fig. 12i), and biotite, whereas sillimanite appears in equilibrium with muscovite, and biotite. The two texturally distinct biotite generations have the same composition however.

C.5. Metamorphic rocks of the Lut Block: Deh-Salm Complex

Measurements were performed for three micaschists (16–54, 55, 57), one migmatite (14–29) and one amphibolite (16–56; Fig. 11d; supplementary Table 2). Biotite shows XMg values between 0.35 and 0.45, and Si between 2.55 and 2.9, except for samples 16–57 and partly 16–54 (XMg ~ 0.55). Chemical mapping (sample 14–29a) confirms the textural difference observed between biotite crystals: biotite associated with garnet has XMg ≥ 0.4, whereas biotite replacing garnet has XMg < 0.4. Garnet from sample 14–29a are almandine-rich, and homogeneous, except for a small rim exhibiting Mn-enrichment. Feldspar is

mainly Na-rich plagioclase, with 50% to 100% albite end-member. Sample 16–57 also contains K-feldspar. Plagioclase in amphibolite (16–56) exhibit a wide range of compositions between 42% and 96% of albite end-member.

White mica is phengite close to the muscovite pole. Si varies between 3 and 3.2, with rare values up to 3.4 and XMg ranges between 0.35 and 0.65. In sample 14–29a, white mica with the highest Si contents (>3.05) is associated with garnet, kyanite, and biotite (XMg > 0.4), whereas others are associated with retrograde sillimanite and biotite (XMg < 0.4). Amphibole from sample 16–56 is Mg-hornblende with a XMg between 0.5 and 0.7.

Appendix D. Supplementary material

Supplementary Figure 1. Representative sediments of the Neh Complex stratigraphic succession. **Supplementary Figure 2.** Representative sediments of the Sefidabeh stratigraphic succession. **Supplementary Table 1.** GPS coordinates and mineralogy of the studied samples. **Supplementary Figure 3.** Compositional plots of minerals: **a)** for the ophiolitic rocks; **b)** for the Birjand metasediments; **c)** for the amphibolite-facies sole; **d)** for the micaschist close to the Neh Complex; **e)** for the Deh-Salm metamorphic rocks. Microprobe analysis are given in supplementary material 2. **Supplementary Table 2.** GPS coordinates of the studied outcrops. **Supplementary Table 3.** Raman results and mineral microprobe analysis for each metamorphic rock type. **Supplementary Table 4.** Bulk composition and mineral assemblage for each pseudosection. Supplementary data to this article can be found online at https://doi.org/10.1016/j.gr.2022.04.004.

References

Agard, P., Jolivet, L., Vrielynck, B., Burov, E., Monié, P., 2007. Plate acceleration: The obduction trigger? Earth Planet. Sci. Lett. 258, 428–441. https://doi.org/10.1016/j.epsl.2007.04.002.

Agard, P., Monié, P., Gerber, W., Omrani, J., Molinaro, M., Meyer, B., Labrousse, L., Vrielynck, B., Jolivet, L., Yamato, P., 2006. Transient, synobduction exhumation of Zagros blueschists inferred from P-T, deformation, time, and kinematic constraints: Implications for Neotethyan wedge dynamics: Transient exhumation processes in Zagros. J. Geophys. Res.: Solid Earth 111. https://doi.org/10.1029/2005JB004103.

Agard, P., Omrani, J., Jolivet, L., Whitechurch, H., Vrielynck, B., Spakman, W., Monié, P., Meyer, B., Wortel, R., 2011. Zagros orogeny: a subduction-dominated process. Geol. Mag. 148, 692–725. https://doi.org/10.1017/S001675681100046X.

Agard, P., Plunder, A., Angiboust, S., Bonnet, G., Ruh, J., 2018. The subduction plate interface: rock record and mechanical coupling (from long to short timescales). Lithos 320–321, 537–566. https://doi.org/10.1016/j.lithos.2018.09.029.

Agard, P., Prigent, C., Soret, M., Dubacq, B., Guillot, S., Deldicque, D., 2020. Slabitization: Mechanisms controlling subduction development and viscous coupling. Earth Sci. Rev. 208, 103259. https://doi.org/10.1016/j.earscirev.2020.103259.

Agard, P., Yamato, P., Soret, M., Prigent, C., Guillot, S., Plunder, A., Dubacq, B., Chauvet, A., Monié, P., 2016. Plate interface rheological switches during subduction infancy: Control on slab penetration and metamorphic sole formation. Earth Planet. Sci. Lett. 451, 208–220. https://doi.org/10.1016/j.epsl.2016.06.054.

Ajirlu, M.S., Moazzen, M., Hajialioghli, R., 2016. Tectonic evolution of the Zagros Orogen in the realm of the Neotethys between the Central Iran and Arabian Plates: An ophiolite perspective. Central Europ. Geol. 59, 1–27. https://doi.org/10.1556/24.59.2016.001.

Aleinikoff, J.N., Wintsch, R.P., Tollo, R.P., Unruh, D.M., Fanning, C.M., Schmitz, M.D., 2007. Ages and origins of rocks of the Killingworth dome, south-central Connecticut: Implications for the tectonic evolution of southern New England. Am. J. Sci. 307, 63–118. https://doi.org/10.2475/01.2007.04.

Angiboust, S., Agard, P., De Hoog, J.C.M., Omrani, J., Plunder, A., 2013. Insights on deep, accretionary subduction processes from the Sistan ophiolitic "mélange" (Eastern Iran). Lithos 156–159, 139–158. https://doi.org/10.1016/j.lithos.2012.11.007.

Arjmandzadeh, R., Karimpour, M.H., Mazaheri, S.A., Santos, J.F., Medina, J.M., Homam, S.M., 2011. Sr-Nd isotope geochemistry and petrogenesis of the Chah-Shaljami granitoids (Lut Block, Eastern Iran). J. Asian Earth Sci. 41, 283–296. https://doi.org/10.1016/j.jseaes.2011.02.014.

Azizi, H., Stern, R.J., 2019. Jurassic igneous rocks of the central Sanandaj-Sirjan zone (Iran) mark a propagating continental rift, not a magmatic arc. Terra Nova 31, 415–423. https://doi.org/10.1111/ter.12404.

Babazadeh, S.A., De Wever, P., 2004. Early Cretaceous radiolarian assemblages from radiolarites in the Sistan Suture (eastern Iran). Geodiversitas 26, 185–206.

Barrier, E., Vrielynck, B., Brouillet, J.-F., Brunet, M.-F., 2018. Paleotetconic reconstruction of the Central Tethyan realm. Atlas of 20 maps.

Berberian, F., Berberian, M., 1981. Tectono-plutonic episodes in Iran. Zagros Hindu Kush Himalaya Geodynamic Evolution, 5–32.

Berberian, M., Jackson, J.A., Qorashi, M., Talebian, M., Khatib, M., Priestley, K., 2000. The 1994 Sefidabeh earthquakes in eastern Iran: blind thrusting and bedding-plane slip on a growing anticline, and active tectonics of the Sistan suture zone. Geophys. J. Int. 142, 283–299.

Berberian, M., King, G.C.P., 1981. Towards a paleogeography and tectonic evolution of Iran. Can. J. Earth Sci. 18, 210–265. https://doi.org/10.1139/e81-019.

Besse, J., Torcq, F., Gallet, Y., Ricou, L.E., Krystyn, L., Saidi, A., 1998. Late Permian to Late Triassic palaeomagnetic data from Iran: constraints on the migration of the Iranian block through the Tethyan Ocean and initial destruction of Pangaea. Geophys. J. Int. 135, 77–92. https://doi.org/10.1046/j.1365-246X.1998.00603.x.

Beyssac, O., Goffé, B., Chopin, C., Rouzaud, J.N., 2002. Raman spectra of carbonaceous material in metasediments: a new geothermometer: Raman spectroscopy of carbonaceous material. J. Metamorph. Geol. 20, 859–871. https://doi.org/10.1046/j.1525-1314.2002.00408.x.

Bonnet, G., Agard, P., Angiboust, S., Fournier, M., Omrani, J., 2019. No large earthquakes in fully exposed subducted seamount. Geology 47, 407–410. https://doi.org/10.1130/G45564.1.

Bonnet, G., Agard, P., Angiboust, S., Monié, P., Jentzer, M., Omrani, J., Whitechurch, H., Fournier, M., 2018. Tectonic slicing and mixing processes along the subduction interface: The Sistan example (Eastern Iran). Lithos 310–311, 269–287. https://doi.org/10.1016/j.lithos.2018.04.016.

Bonnet, G., Agard, P., Whitechurch, H., Fournier, M., Angiboust, S., Caron, B., Omrani, J., 2020. Fossil seamount in southeast Zagros records intraoceanic arc to back-arc transition: New constraints for the evolution of the Neotethys. Gondwana Res. 81, 423–444. https://doi.org/10.1016/j.gr.2019.10.019.

Boudier, F., Ceuleneer, G., Nicolas, A., 1988. Shear zones, thrusts and related magmatism in the Oman ophiolite: Initiation of thrusting on an oceanic ridge. Tectonophysics 151, 275–296. https://doi.org/10.1016/0040-1951(88)90249-1.

Bröcker, M., Fotoohi Rad, G., Abbaslu, F., Rodionov, N., 2014. Geochronology of high-grade metamorphic rocks from the Anjul area, Lut block, eastern Iran. J. Asian Earth Sci. 82, 151–162. https://doi.org/10.1016/j.jseaes.2013.12.021.

Bröcker, M., Fotoohi Rad, G., Burgess, R., Theunissen, S., Paderin, I., Rodionov, N., Salimi, Z., 2013. New age constraints for the geodynamic evolution of the Sistan Suture Zone, eastern Iran. Lithos 170–171, 17–34. https://doi.org/10.1016/j.lithos.2013.02.012.

Bröcker, M., Omrani, H., Berndt, J., Moslempour, M.E., 2021. Unravelling metamorphic ages of suture zone rocks from the Sabzevar and Makran areas (Iran): Robust age constraints for the larger Arabia-Eurasian collision zone jmg.12603 J. Metamorph. Geol. https://doi.org/10.1111/jmg.12603.

Brunet, M.-F., Korotaev, M.V., Ershov, A.V., Nikishin, A.M., 2003. The South Caspian Basin: a review of its evolution from subsidence modelling. Sed. Geol. 156, 119–148. https://doi.org/10.1016/S0037-0738(02)00285-3.

Burg, J.-P., 2018. Geology of the onshore Makran accretionary wedge: Synthesis and tectonic interpretation. Earth Sci. Rev. 185, 1210–1231. https://doi.org/10.1016/j.earscirev.2018.09.011.

Camp, V.E., Griffis, R.J., 1982. Character, genesis and tectonic setting of igneous rocks in the Sistan suture zone, eastern Iran. Lithos 15, 221–239.

Cannat, M., Sauter, D., Escartin, J., Lavier, L., Picazo, S., 2009. Oceanic corrugated surfaces and the strength of the axial lithosphere at slow spreading ridges. Earth Planet. Sci. Lett. 288, 174–183. https://doi.org/10.1016/j.epsl.2009.09.020.

Chen, S., Wu, D., Liu, G., Sun, R., 2017. Raman spectral characteristics of magmatic-contact metamorphic coals from Huainan Coalfield, China. Spectrochim. Acta. A. Mol. Biomol. Spectrosc. 171, 31–39. https://doi.org/10.1016/j.saa.2016.07.032.

Connolly, J.A.D., 1990. Multivariable phase diagrams: an algorithm based on generalized thermodynamics. Am. J. Sci. 290, 666–718.

Connolly, J.A.D., 2005. Computation of phase equilibria by linear programming: A tool for geodynamic modeling and its application to subduction zone decarbonation. Earth Planet. Sci. Lett. 236, 524–541. https://doi.org/10.1016/j.epsl.2005.04.033.

Corfield, R.I., Searle, M.P., Pedersen, R.B., 2001. Tectonic Setting, Origin, and Obduction History of the Spontang Ophiolite, Ladakh Himalaya, NW India. J. Geol. 109, 715–736. https://doi.org/10.1086/323191.

Davies, J.H., 2013. Global map of solid Earth surface heat flow: Global Surface Heat Flow Map. Geochem. Geophys. Geosyst. 14, 4608–4622. https://doi.org/10.1002/ggge.20271.

Davoudzadeh, M., Soffel, H., Schmidt, K., 1981. On the rotation of the Central-East-Iran microplate. Neues Jahrbuch für Geologie und Paläontologie - Abhandlungen, 180–192.

Delaloye, M., Desmons, J., 1980. Ophiolites and mélange terranes in Iran: a geochronological study and its paleotectonic implications. Tectonophysics 68, 83–111.

DeMets, C., Gordon, R.G., Argus, D.F., 2010. Geologically current plate motions. Geophys. J. Int. 181, 1–80. https://doi.org/10.1111/j.1365-246X.2009.04491.x.

Dercourt, J., Zonenshain, L.P., Ricou, L.-E., Kazmin, V.G., Le Pichon, X., Knipper, A.L., Grandjacquet, C., Sbortshikov, I.M., Geyssant, J., Lepvrier, C., et al., 1986. Geological evolution of the Tethys belt from the Atlantic to the Pamirs since the Lias. Tectonophysics 123, 241–315.

Droop, G.T.R., 1987. A general equation for estimating Fe 3+ concentrations in ferromagnesian silicates and oxides from microprobe analyses, using stoichiometric criteria. Mineral. Mag. 51, 431–435.

Dubacq, B., Soret, M., Jewison, E., Agard, P., 2019. Early subduction dynamics recorded by the metamorphic sole of the Mt. Albert ophiolitic complex (Gaspé, Quebec). Lithos 334–335, 161–179. https://doi.org/10.1016/j.lithos.2019.03.019.
Ernst, W.G., Liu, J., 1998. Experimental phase-equilibrium study of Al- and Ti-contents of calcic amphibole in MORB; a semiquantitative thermobarometer. Am. Mineral. 83, 952–969. https://doi.org/10.2138/am-1998-9-1004.
Escartín, J., Mével, C., Petersen, S., Bonnemains, D., Cannat, M., Andreani, M., Augustin, N., Bezos, A., Chavagnac, V., Choi, Y., Godard, M., Haaga, K., Hamelin, C., Ildefonse, B., Jamieson, J., John, B., Leleu, T., MacLeod, C.J., Massot-Campos, M., Nomikou, P., Olive, J.A., Paquet, M., Rommevaux, C., Rothenbeck, M., Steinfuhrer, A., Tominaga, M., Triebe, L., Campos, R., Gracias, N., Garcia, R., 2017. Tectonic structure, evolution, and the nature of oceanic core complexes and their detachment fault zones (13°20′N and 13°30′N, Mid Atlantic Ridge): 13°N MAR CORRUGATED OCEANIC DETACHMENTS. Geochem. Geophys. Geosyst. 18, 1451–1482. https://doi.org/10.1002/2016GC006775.
Eshagh, M., Tenzer, R., Eshagh, Mehrdad, 2019. Elastic thickness of the Iranian lithosphere from gravity and seismic data. Tectonophysics, 228186. https://doi.org/10.1016/j.tecto.2019.228186.
Esmaeily, D., Nédélec, A., Valizadeh, M.V., Moore, F., Cotten, J., 2005. Petrology of the Jurassic Shah-Kuh granite (eastern Iran), with reference to tin mineralization. J. Asian Earth Sci. 25, 961–980. https://doi.org/10.1016/j.jseaes.2004.09.003.
Farahat, E.S., 2011. Geotectonic significance of Neoproterozoic amphibolites from the Central Eastern Desert of Egypt: A possible dismembered sub-ophiolitic metamorphic sole. Lithos 125, 781–794. https://doi.org/10.1016/j.lithos.2011.04.009.
Festa, A., Pini, G.A., Ogata, K., Dilek, Y., 2019. Diagnostic features and field-criteria in recognition of tectonic, sedimentary and diapiric mélanges in orogenic belts and exhumed subduction-accretion complexes. Gondwana Res. https://doi.org/10.1016/j.gr.2019.01.003.
Fotoohi Rad, G.R., Droop, G.T.R., Amini, S., Moazzen, M., 2005. Eclogites and blueschists of the Sistan Suture Zone, eastern Iran: A comparison of P-T histories from a subduction mélange. Lithos 84, 1–24. https://doi.org/10.1016/j.lithos.2005.01.007.
Fotoohi Rad, G.R., Droop, G.T.R., Burgess, R., 2009. Early Cretaceous exhumation of high-pressure metamorphic rocks of the Sistan Suture Zone, eastern Iran. Geol. J. 44, 104–116. https://doi.org/10.1002/gj.1135.
Gaggero, L., Marroni, M., Pandolfi, L., Buzzi, L., 2009. Modeling the oceanic lithosphere obduction: Constraints from the metamorphic sole of Mirdita ophiolites (northern Albania). Ofioliti 34, 17–42.
Gaina, C., van Hinsbergen, D.J.J., Spakman, W., 2015. Tectonic interactions between India and Arabia since the Jurassic reconstructed from marine geophysics, ophiolite geology, and seismic tomography: India-Arabia Tectonic Interactions. Tectonics 34, 875–906. https://doi.org/10.1002/2014TC003780.
Ghazi, A.M., Hassanipak, A.A., Mahoney, J.J., Duncan, R.A., 2004. Geochemical characteristics, 40Ar–39Ar ages and original tectonic setting of the Band-e-Zeyarat/Dar Anar ophiolite, Makran accretionary prism, S.E. Iran. Tectonophysics 393, 175–196. https://doi.org/10.1016/j.tecto.2004.07.035.
Ghazi, J.M., Moazzen, M., Rahgoshay, M., Shafaii Moghadam, H., 2012. Geochemical characteristics of basaltic rocks from the Nain ophiolite (Central Iran); constraints on mantle wedge source evolution in an oceanic back arc basin and a geodynamical model. Tectonophysics 574–575, 92–104. https://doi.org/10.1016/j.tecto.2011.10.001.
Gnos, E., Immenhauser, A., Peters, T.J., 1997. Late Cretaceous/early Tertiary convergence between the Indian and Arabian plates recorded in ophiolites and related sediments. Tectonophysics 271, 1–19. https://doi.org/10.1016/S0040-1951(96)00249-1.
Green, E.C.R., White, R.W., Diener, J.F.A., Powell, R., Holland, T.J.B., Palin, R.M., 2016. Activity-composition relations for the calculation of partial melting equilibria in metabasic rocks. J. Metamorph. Geol. 34, 845–869. https://doi.org/10.1111/jmg.12211.
Guilmette, C., Smit, M.A., van Hinsbergen, D.J.J., Gürer, D., Corfu, F., Charette, B., Maffione, M., Rabeau, O., Savard, D., 2018. Forced subduction initiation recorded in the sole and crust of the Semail Ophiolite of Oman. Nat. Geosci. 11, 688–695. https://doi.org/10.1038/s41561-018-0209-2.
Harris, R.A., 1998. Origin and tectonic evolution of the metamorphic sole beneath the Brooks Range ophiolite, Alaska. Spec. Pap.-Geol. Soc. Am., 293–312
Hässig, M., Rolland, Y., Sosson, M., Galoyan, G., Sahakyan, L., Topuz, G., Çelik, Ö.F., Avagyan, A., Müller, C., 2013. Linking the NE Anatolian and Lesser Caucasus ophiolites: evidence for large-scale obduction of oceanic crust and implications for the formation of the Lesser Caucasus-Pontides Arc. Geodin. Acta 26, 311–330. https://doi.org/10.1080/09853111.2013.877236.
Hayden, L.A., Watson, E.B., Wark, D.A., 2008. A thermobarometer for sphene (titanite). Contrib. Miner. Petrol. 155, 529–540. https://doi.org/10.1007/s00410-007-0256-y.
Henry, D.J., 2005. The Ti-saturation surface for low-to-medium pressure metapelitic biotites: Implications for geothermometry and Ti-substitution mechanisms. Am. Mineral. 90, 316–328. https://doi.org/10.2138/am.2005.1498.
Holdaway, M.J., 2000. Application of new experimental and garnet Margules data to the garnet-biotite geothermometer. Am. Mineral. 85, 881–892. https://doi.org/10.2138/am-2000-0701.
Holland, T., Blundy, J., 1994. Non-ideal interactions in calcic amphiboles and their bearing on amphibole-plagioclase thermometry. Contrib. Miner. Petrol. 116, 433–447.
Holland, T., Powell, R., 2003. Activity composition relations for phases in petrological calculations: an asymmetric multicomponent formulation. Contrib. Miner. Petrol. 145, 492–501. https://doi.org/10.1007/s00410-003-0464-z.
Holland, T.J.B., Powell, R., 2011. An improved and extended internally consistent thermodynamic dataset for phases of petrological interest, involving a new equation of state for solids: Thermodynamic dataset for phases of petrological interest. J. Metamorph. Geol. 29, 333–383. https://doi.org/10.1111/j.1525-1314.2010.00923.x.
Hunziker, D., Burg, J.-P., Bouilhol, P., von Quadt, A., 2015. Jurassic rifting at the Eurasian Tethys margin: Geochemical and geochronological constraints from granitoids of North Makran, southeastern Iran. Tectonics 34, 571–593. https://doi.org/10.1002/2014TC003768.
Hunziker, D., Burg, J.-P., Moulas, E., Reusser, E., Omrani, J., 2017. Formation and preservation of fresh lawsonite: Geothermobarometry of the North Makran Blueschists, southeast Iran. J. Metamorph. Geol. 35, 871–895. https://doi.org/10.1111/jmg.12259.
Jentzer, M., Fournier, M., Agard, P., Omrani, J., Khatib, M.M., Whitechurch, H., 2017. Neogene to Present paleostress field in Eastern Iran (Sistan belt) and implications for regional geodynamics: Paleostress Field in Eastern Iran. Tectonics 36, 321–339. https://doi.org/10.1002/2016TC004275.
Jentzer, M., Whitechurch, H., Agard, P., Ulrich, M., Caron, B., Zarrinkoub, M.H., Kohansal, R., Miguet, L., Omrani, J., Fournier, M., 2020. Late Cretaceous calc-alkaline and adakitic magmatism in the Sistan suture zone (Eastern Iran): Implications for subduction polarity and regional tectonics. J. Asian Earth Sci., 104588 https://doi.org/10.1016/j.jseaes.2020.104588.
Kazemi, Z., Ghasemi, H., Tilhac, R., Griffin, W., Moghadam, H.S., O'Reilly, S., Mousivand, F., 2019. Late Cretaceous subduction-related magmatism on the southern edge of Sabzevar basin, NE Iran. J. Geol. Soc. 176, 530–552.
Khalatbari Jafari, M., Babaie, H.A., Gani, M., 2013. Geochemical evidence for Late Cretaceous marginal arc-to-backarc transition in the Sabzevar ophiolitic extrusive sequence, northeast Iran. J. Asian Earth Sci. 70–71, 209–230. https://doi.org/10.1016/j.jseaes.2013.03.015.
Kontoyannis, C.G., Vagenas, N.V., 2000. Calcium carbonate phase analysis using XRD and FT-Raman spectroscopy. The Analyst 125, 251–255. https://doi.org/10.1039/a908609i.
Kouketsu, Y., Mizukami, T., Mori, H., Endo, S., Aoya, M., Hara, H., Nakamura, D., Wallis, S., 2014. A new approach to develop the Raman carbonaceous material geothermometer for low-grade metamorphism using peak width: Raman CM geothermometer using FWHM. Isl. Arc 23, 33–50. https://doi.org/10.1111/iar.12057.
Kurzawa, T., Bröcker, M., Fotoohi Rad, G., Berndt, J., Lisker, F., 2017. Cretaceous high-pressure metamorphism and low pressure overprint in the Sistan Suture Zone, eastern Iran: Additional temperature estimates for eclogites, geological significance of U-Pb zircon ages and Rb-Sr constraints on the timing of exhumation. J. Asian Earth Sci. 147, 332–344. https://doi.org/10.1016/j.jseaes.2017.07.051.
Kylander-Clark, A.R.C., Hacker, B.R., Cottle, J.M., 2013. Laser-ablation split-stream ICP petrochronology. Chem. Geol. 345, 99–112. https://doi.org/10.1016/j.chemgeo.2013.02.019.
Lahfid, A., Beyssac, O., Deville, E., Negro, F., Chopin, C., Goffé, B., 2010. Evolution of the Raman spectrum of carbonaceous material in low-grade metasediments of the Glarus Alps (Switzerland): RSCM in low-grade metasediments. Terra Nova 22, 354–360. https://doi.org/10.1111/j.1365-3121.2010.00956.x.
Leake, B.E., Woolley, A.R., Arps, C.E.S., Birch, W.D., Hawthorne, F.C., Kato, A., Kisch, H.J., Krivovichev, V.G., Linthout, K., Laird, J., Mandarino, J.A., Maresch, W.V., 1997. Nomenclature of amphiboles: report of the subcommittee on amphiboles of the international mineralogical association, commission on new minerals and mineral names 28.
Lindenberg, H.G., Groler, K., 1984. Post-paleozoic stratigraphy, structure and orogenetic evolution of the southern Sabzevar zone and the Taknar block. Neues Jahrb. Für Geol. Paläontol.-Abh. 287–326.
Lucazeau, F., 2019. Analysis and mapping of an updated terrestrial heat flow dataset. Geochem. Geophys. Geosyst. https://doi.org/10.1029/2019GC008389.
Mahmood, K., Boudier, F., Gnos, E., Monié, P., Nicolas, A., 1995. 40Ar/39Ar dating of the emplacement of the Muslim Bagh ophiolite, Pakistan. Tectonophysics 250, 169–181. https://doi.org/10.1016/0040-1951(95)00017-5.
Mahmoudi, S., Masoudi, F., Corfu, F., Mehrabi, B., 2010. Magmatic and metamorphic history of the Deh-Salm metamorphic Complex, Eastern Lut block, (Eastern Iran), from U-Pb geochronology. Int. J. Earth Sci. 99, 1153–1165. https://doi.org/10.1007/s00531-009-0465-x.
Masoudi, F., Mehrabi, B., Mahmoudi, S., 2006. Garnet (Almandine-Spessartine) Growth Zoning and Its Application to Constrain Metamorphic History in Dehsalm Complex. Iran 17, 11.
Mattei, M., Cifelli, F., Muttoni, G., Rashid, H., 2015. Post-Cimmerian (Jurassic-Cenozoic) paleogeography and vertical axis tectonic rotations of Central Iran and the Alborz Mountains. J. Asian Earth Sci. 102, 92–101. https://doi.org/10.1016/j.jseaes.2014.09.038.
Mattei, M., Cifelli, F., Muttoni, G., Zanchi, A., Berra, F., Mossavvari, F., Eshraghi, S.A., 2012. Neogene block rotation in central Iran: Evidence from paleomagnetic data. Geol. Soc. Am. Bull. 14.
Matthews, K.J., Seton, M., Müller, R.D., 2012. A global-scale plate reorganization event at 105–100Ma. Earth Planet. Sci. Lett. 355–356, 283–298. https://doi.org/10.1016/j.epsl.2012.08.023.
Mazhari, S.A., Klötzli, U., Safari, M., 2019. Petrological investigation of Late Cretaceous magmatism in Kaboodan area, NE Iran: Evidence for an active

continental arc at Sabzevar zone. Lithos 348–349, 105183. https://doi.org/10.1016/j.lithos.2019.105183.
McCall, G.J.H., 1997. The geotectonic history of the Makran and adjacent areas of southern Iran. J. Asian Earth Sci. 15, 517–531.
McCall, G.J.H., 2002. A summary of the geology of the Iranian Makran. Geol. Soc. Lond. Spec. Publ. 195, 147–204. https://doi.org/10.1144/GSL.SP.2002.195.01.10.
McQuarrie, N., van Hinsbergen, D.J.J., 2013. Retrodeforming the Arabia-Eurasia collision zone: Age of collision versus magnitude of continental subduction. Geology 41, 315–318. https://doi.org/10.1130/G33591.1.
Moazzen, M., Modjarrad, M., Zarrinkoub, M., 2006. Mineral chemistry, petrogenesis and P-T conditions of formation of harzburgitic peridotites from south of Birjand, Eastern Iran. J. Asian Earth Sci. https://doi.org/10.1016/j.jseaes.2005.07.009.
Moghadam, H.S., Corfu, F., Chiaradia, M., Stern, R.J., Ghorbani, G., 2014. Sabzevar Ophiolite, NE Iran: Progress from embryonic oceanic lithosphere into magmatic arc constrained by new isotopic and geochemical data. Lithos 210–211, 224–241. https://doi.org/10.1016/j.lithos.2014.10.004.
Moghadam, H.S., Stern, R.J., 2011. Geodynamic evolution of Upper Cretaceous Zagros ophiolites: formation of oceanic lithosphere above a nascent subduction zone. Geol. Mag. 148, 762–801. https://doi.org/10.1017/S0016756811000410.
Moghadam, H.S., Stern, R.J., 2015. Ophiolites of Iran: Keys to understanding the tectonic evolution of SW Asia: (II) Mesozoic ophiolites. J. Asian Earth Sci. 100, 31–59. https://doi.org/10.1016/j.jseaes.2014.12.016.
Moghadam, H.S., Stern, R.J., Chiaradia, M., Rahgoshay, M., 2013. Geochemistry and tectonic evolution of the Late Cretaceous Gogher–Baft ophiolite, central Iran 15.
Moghadam, H.S., Whitechurch, H., Rahgoshay, M., Monsef, I., 2009. Significance of Nain-Baft ophiolitic belt (Iran): Short-lived, transtensional Cretaceous back-arc oceanic basins over the Tethyan subduction zone. Comptes Rendus Geosci. 341, 1016–1028. https://doi.org/10.1016/j.crte.2009.06.011.
Mohammadi, A., Burg, J.-P., Bouilhol, P., Ruh, J., 2016. U-Pb geochronology and geochemistry of Zahedan and Shah Kuh plutons, southeast Iran: Implication for closure of the South Sistan suture zone. Lithos 248–251, 293–308. https://doi.org/10.1016/j.lithos.2016.02.003.
Molina, J.F., Moreno, J.A., Castro, A., Rodríguez, C., Fershtater, G.B., 2015. Calcic amphibole thermobarometry in metamorphic and igneous rocks: New calibrations based on plagioclase/amphibole Al-Si partitioning and amphibole/liquid Mg partitioning. Lithos 232, 286–305. https://doi.org/10.1016/j.lithos.2015.06.027.
Montenat, C., 2009. The Mesozoic of Afghanistan. GeoArabia 14, 64.
Mousavi, N., Ebbing, J., 2018. Basement characterization and crustal structure beneath the Arabia-Eurasia collision (Iran): A combined gravity and magnetic study. Tectonophysics 731–732, 155–171. https://doi.org/10.1016/j.tecto.2018.03.018.
Nasrabady, M., Rossetti, F., Theye, T., Vignaroli, G., 2011. Metamorphic history and geodynamic significance of the Early Cretaceous Sabzevar granulites (Sabzevar structural zone, NE Iran). Solid Earth 2, 219–243. https://doi.org/10.5194/se-2-219-2011.
Omidianfar, S., Monsef, I., Rahgoshay, M., Zheng, J., Cousens, B., 2020. The middle Eocene high-K magmatism in Eastern Iran Magmatic Belt: constraints from U-Pb zircon geochronology and Sr-Nd isotopic ratios. Int. Geol. Rev. 1–18. https://doi.org/10.1080/00206814.2020.1716272.
Omrani, H., 2017. Geodynamic evolution of the Sabzevar zone, northern central Iranian micro-continent. Miner Petrol 19. https://doi.org/10.1007/s00710-017-0505-3.
Omrani, J., Agard, P., Whitechurch, H., Benoit, M., Prouteau, G., Jolivet, L., 2008. Arc-magmatism and subduction history beneath the Zagros Mountains, Iran: A new report of adakites and geodynamic consequences. Lithos 106, 380–398. https://doi.org/10.1016/j.lithos.2008.09.008.
Ozsvárt, P., Bahramnejad, E., Bagheri, S., Sharifi, M., 2020. New Albian (Cretaceous) radiolarian age constraints for the Dumak ophiolitic mélange from the Shuru area, Eastern Iran. Cretaceous Res., 104451 https://doi.org/10.1016/j.cretres.2020.104451.
Pang, K.-N., Chung, S.-L., Zarrinkoub, M.H., Khatib, M.M., Mohammadi, S.S., Chiu, H.-Y., Chu, C.-H., Lee, H.-Y., Lo, C.-H., 2013. Eocene-Oligocene post-collisional magmatism in the Lut-Sistan region, eastern Iran: Magma genesis and tectonic implications. Lithos 180–181, 234–251. https://doi.org/10.1016/j.lithos.2013.05.009.
Pang, K.-N., Chung, S.-L., Zarrinkoub, M.H., Mohammadi, S.S., Yang, H.-M., Chu, C.-H., Lee, H.-Y., Lo, C.-H., 2012. Age, geochemical characteristics and petrogenesis of Late Cenozoic intraplate alkali basalts in the Lut-Sistan region, eastern Iran. Chem. Geol. 306–307, 40–53. https://doi.org/10.1016/j.chemgeo.2012.02.020.
Paton, C., Hellstrom, J., Paul, B., Woodhead, J., Hergt, J., 2011. Iolite: Freeware for the visualisation and processing of mass spectrometric data. J. Anal. At. Spectrom. 26, 2508. https://doi.org/10.1039/c1ja10172b.
Pearce, N.J.G., Perkins, W.T., Westgate, J.A., Gorton, M.P., Jackson, S.E., Neal, C.R., Chenery, S.P., 1997. A Compilation of New and Published Major and Trace Element Data for NIST SRM 610 and NIST SRM 612 Glass Reference Materials. Geostand. Geoanal. Res. 21, 115–144. https://doi.org/10.1111/j.1751-908X.1997.tb00538.x.
Picazo, S., Cannat, M., Delacour, A., Escartin, J., Rouméjon, S., Silantyev, S., 2012. Deformation associated with the denudation of mantle-derived rocks at the Mid-Atlantic Ridge 13?-15?N: The role of magmatic injections and hydrothermal alteration: Denudation of ultramafic rocks. Geochem. Geophys. Geosyst. 13. https://doi.org/10.1029/2012GC004121.
Pirnia, T., 2020. Cretaceous tectonic evolution of the Neo-Tethys in Central Iran: Evidence from petrology and age of the Nain-Ashin ophiolitic basalts. Geosci. Front., 25
Plunder, A., Agard, P., Chopin, C., Soret, M., Okay, A.I., Whitechurch, H., 2016. Metamorphic sole formation, emplacement and blueschist facies overprint: early subduction dynamics witnessed by western Turkey ophiolites. Terra Nova 28, 329–339. https://doi.org/10.1111/ter.12225.
Pouchou, J.-L., Pichoir, F., 1991. Quantitative Analysis of Homogeneous or Stratified Microvolumes Applying the Model "PAP". Electron Probe Quantitation, 31–75.
Renne, P.R., Swisher, C.C., Deino, A.L., Karner, D.B., Owens, T.L., DePaolo, D.J., 1998. Intercalibration of standards, absolute ages and uncertainties in 40Ar/39Ar dating. Chem. Geol. 145, 117–152. https://doi.org/10.1016/S0009-2541(97)00159-9.
Richards, J.P., Sholeh, A., 2016. Chapter 7 The Tethyan Tectonic History and Cu-Au Metallogeny of Iran 20.
Rioux, M., Garber, J., Bauer, A., Bowring, S., Searle, M., Kelemen, P., Hacker, B., 2016. Synchronous formation of the metamorphic sole and igneous crust of the Semail ophiolite: New constraints on the tectonic evolution during ophiolite formation from high-precision U-Pb zircon geochronology. Earth Planet. Sci. Lett. 451, 185–195. https://doi.org/10.1016/j.epsl.2016.06.051.
Robert, A.M.M., Letouzey, J., Kavoosi, M.A., Sherkati, S., Müller, C., Vergés, J., Aghababaei, A., 2014. Structural evolution of the Kopeh Dagh fold-and-thrust belt (NE Iran) and interactions with the South Caspian Sea Basin and Amu Darya Basin. Mar. Pet. Geol. 57, 68–87. https://doi.org/10.1016/j.marpetgeo.2014.05.002.
Rodriguez, M., Arnould, M., Coltice, N., Soret, M., 2021. Long-term evolution of a plume-induced subduction in the Neotethys realm. Earth Planet. Sci. Lett. 561, 116798. https://doi.org/10.1016/j.epsl.2021.116798.
Rodriguez, M., Huchon, P., Chamot-Rooke, N., Fournier, M., Delescluse, M., Smit, J., Plunder, A., Calvès, G., Ninkabou, D., Pubellier, M., François, T., Agard, P., Gorini, C., 2020. Successive shifts of the India-Africa transform plate boundary during the Late Cretaceous-Paleogene interval: Implications for ophiolite emplacement along transforms. J. Asian Earth Sci. 191, 104225. https://doi.org/10.1016/j.jseaes.2019.104225.
Rolland, Y., Galoyan, G., Bosch, D., Sosson, M., Corsini, M., Fornari, M., Verati, C., 2009. Jurassic back-arc and Cretaceous hot-spot series In the Armenian ophiolites — Implications for the obduction process. Lithos 112, 163–187. https://doi.org/10.1016/j.lithos.2009.02.006.
Rossetti, F., Nasrabady, M., Theye, T., Gerdes, A., Monié, P., Lucci, F., Vignaroli, G., 2014. Adakite differentiation and emplacement in a subduction channel: The late Paleocene Sabzevar magmatism (NE Iran). Geol. Soc. America Bull., 27
Rossetti, F., Nasrabady, M., Vignaroli, G., Theye, T., Gerdes, A., Razavi, M.H., Vaziri, H. M., 2010. Early Cretaceous migmatitic mafic granulites from the Sabzevar range (NE Iran): implications for the closure of the Mesozoic peri-Tethyan oceans in central Iran. Terra Nova 22, 26–34. https://doi.org/10.1111/j.1365-3121.2009.00912.x.
Saccani, E., Delavari, M., Beccaluva, L., Amini, S., 2010. Petrological and geochemical constraints on the origin of the Nehbandan ophiolitic complex (eastern Iran): Implication for the evolution of the Sistan Ocean. Lithos 117, 209–228. https://doi.org/10.1016/j.lithos.2010.02.016.
Saccani, E., Delavari, M., Dolati, A., Marroni, M., Pandolfi, L., Chiari, M., Barbero, E., 2018. New insights into the geodynamics of Neo-Tethys in the Makran area: Evidence from age and petrology of ophiolites from the Coloured Mélange Complex (SE Iran). Gondwana Res. 62, 306–327. https://doi.org/10.1016/j.gr.2017.07.013.
Schmitz, M.D., Bowring, S.A., 2001. U-Pb zircon and titanite systematics of the Fish Canyon Tuff: an assessment of high-precision U-Pb geochronology and its application to young volcanic rocks. Geochim. Cosmochim. Acta 65, 2571–2587. https://doi.org/10.1016/S0016-7037(01)00616-0.
Schmitz, M.D., Schoene, B., 2007. Derivation of isotope ratios, errors, and error correlations for U-Pb geochronology using 205 Pb- 235 U-(233 U)-spiked isotope dilution thermal ionization mass spectrometric data: U-PB isotope ratio derivation. Geochem. Geophys. Geosyst. 8, n/a-n/a. https://doi.org/10.1029/2006GC001492.
Schwartz, S., Guillot, S., Reynard, B., Lafay, R., Debret, B., Nicollet, C., Lanari, P., Auzende, A.L., 2013. Pressure–temperature estimates of the lizardite/antigorite transition in high pressure serpentinites. Lithos 178, 197–210. https://doi.org/10.1016/j.lithos.2012.11.023.
Sengor, A.M.C., Altiner, D., Cin, A., Ustaomer, T., Hsu, K.J., 1988. Origin and assembly of the Tethyside orogenic collage at the expense of Gondwana Land. Geological Society, London, Special Publications 37, 119–181. https://doi.org/10.1144/GSL.SP.1988.037.01.09.
Sepidbar, F., Frederico, L., Habib, B., Mohamed Zaki, K., Peng, J., 2020. Geochemistry and tectonic significance of the Fannuj-Maskutan SSZ-type ophiolite (Inner Makran, SE Iran). Int. Geol. Rev. 29. https://doi.org/10.1080/00206814.2020.1753118.
Seton, M., Müller, R.D., Zahirovic, S., Gaina, C., Torsvik, T., Shephard, G., Talsma, A., Gurnis, M., Turner, M., Maus, S., Chandler, M., 2012. Global continental and ocean basin reconstructions since 200Ma. Earth Sci. Rev. 113, 212–270. https://doi.org/10.1016/j.earscirev.2012.03.002.
Sharkovski, M., Susov, M., Krivyakin, B., 1984. Geology of the Anarak area (Central Iran). Explanatory text of the Anarak quadrangle map.
Shirdashtzadeh, N., Kachovich, S., Aitchison, J.C., Samadi, R., 2015. Mid-Cretaceous radiolarian faunas from the Ashin Ophiolite (western Central-East Iranian Microcontinent). Cretac. Res. 56, 110–118. https://doi.org/10.1016/j.cretres.2015.04.003.

Shirdashtzadeh, N., Torabi, G., Morishita, T., 2020. Evolution of lithospheric mantle in the north of Nain-Baft oceanic crust (Neo-Tethyan ophiolite of Ashin, Central Iran). Isl. Arc 29. https://doi.org/10.1111/iar.12342.
Siehl, A., 2017. Structural setting and evolution of the Afghan orogenic segment – a review. Geological Society, London, Special Publications 427, 57–88. https://doi.org/10.1144/SP427.8.
Soffel, H.C., Davoudzadeh, M., Rolf, C., Schmidt, S., 1996. New palaeomagnetic data from Central Iran and a Triassic palaeoreconstruction. Geol. Rundsch. 85, 293–302. https://doi.org/10.1007/s005310050075.
Soffel, H.C., Förster, H.G., 1984. Polar Wander Path of the Central-East-Iran Microplate Including New Results. Neues Jahrbuch für Geologie und Paläontologie - Abhandlungen 168, 165–172. https://doi.org/10.1127/njgpa/168/1984/165.
Soret, M., Agard, P., Dubacq, B., Plunder, A., Yamato, P., 2017. Petrological evidence for stepwise accretion of metamorphic soles during subduction infancy (Semail ophiolite, Oman and UAE). J. Metamorph. Geol. https://doi.org/10.1111/jmg.12267.
Spandler, C., Hammerli, J., Sha, P., Hilbert-Wolf, H., Hu, Y., Roberts, E., Schmitz, M., 2016. MKED1: A new titanite standard for in situ analysis of Sm–Nd isotopes and U-Pb geochronology. Chem. Geol. 425, 110–126. https://doi.org/10.1016/j.chemgeo.2016.01.002.
Spencer, K.J., Hacker, B.R., Kylander-Clark, A.R.C., Andersen, T.B., Cottle, J.M., Stearns, M.A., Poletti, J.E., Seward, G.G.E., 2013. Campaign-style titanite U-Pb dating by laser-ablation ICP: Implications for crustal flow, phase transformations and titanite closure. Chem. Geol. 341, 84–101. https://doi.org/10.1016/j.chemgeo.2012.11.012.
Stampfli, G.M., Borel, G.D., 2002. A plate tectonic model for the Paleozoic and Mesozoic constrained by dynamic plate boundaries and restored synthetic oceanic isochrons. Earth Planet. Sci. Lett. 196, 17–33. https://doi.org/10.1016/S0012-821X(01)00588-X.
Stipp, M., Stünitz, H., Heilbronner, R., Schmid, S.M., 2002. The eastern Tonale fault zone: a 'natural laboratory' for crystal plastic deformation of quartz over a temperature range from 250 to 700°C. J. Struct. Geol. 24, 1861–1884. https://doi.org/10.1016/S0191-8141(02)00035-4.
Stöcklin, J., 1974. Possible ancient continental margins in Iran. Geol. Continental Margins, 873–887.
Tirrul, R., Bell, I.R., Griffis, R.J., Camp, V.E., 1983. The Sistan suture zone of eastern Iran. Geol. Soc. Am. Bull. 94, 134–150.
Torsvik, T.H., Cocks, L.R.M., 2017. In: Earth History and Palaeogeography. Cambridge University Press, Cambridge. https://doi.org/10.1017/9781316225523.
Verdel, C., Wernicke, B.P., Hassanzadeh, J., Guest, B., 2011. A Paleogene extensional arc flare-up in Iran: iranian volcanism. Tectonics 30. https://doi.org/10.1029/2010TC002809.
Vermeesch, P., 2018. IsoplotR: A free and open toolbox for geochronology. Geosci. Front. 9, 1479–1493. https://doi.org/10.1016/j.gsf.2018.04.001.
Wakabayashi, J., Dilek, Y., 2003. What constitutes 'emplacement' of an ophiolite?: Mechanisms and relationship to subduction initiation and formation of metamorphic soles. Geological Society, London, Special Publications 218, 427–447. https://doi.org/10.1144/GSL.SP.2003.218.01.22.
Walker, R.T., Gans, P., Allen, M.B., Jackson, J., Khatib, M., Marsh, N., Zarrinkoub, M., 2009. Late Cenozoic volcanism and rates of active faulting in eastern Iran. Geophys. J. Int. 177, 783–805. https://doi.org/10.1111/j.1365-246X.2008.04024.x.
Walker, R.T., Khatib, M.M., 2006. Active faulting in the Birjand region of NE Iran: active faulting at Birjand in NE Iran. Tectonics 25. https://doi.org/10.1029/2005TC001871.
White, R.W., Powell, R., Clarke, G.L., 2002. The interpretation of reaction textures in Fe-rich metapelitic granulites of the Musgrave Block, central Australia: constraints from mineral equilibria calculations in the system K2O-FeO-MgO-Al2O3-SiO2-H2O-TiO2-Fe2O3: Reaction textures, musgrave block granulites. J. Metamorph. Geol. 20, 41–55. https://doi.org/10.1046/j.0263-4929.2001.00349.x.
White, R.W., Powell, R., Holland, T.J.B., Johnson, T.E., Green, E.C.R., 2014. New mineral activity-composition relations for thermodynamic calculations in metapelitic systems. J. Metamorph. Geol. 32, 261–286. https://doi.org/10.1111/jmg.12071.
Whitney, D.L., Evans, B.W., 2010. Abbreviations for names of rock-forming minerals. Am. Mineral. 95, 185–187. https://doi.org/10.2138/am.2010.3371.
Wu, C.-M., 2017. Calibration of the garnet-biotite-Al 2 SiO 5 -quartz geobarometer for metapelites. J. Metamorph. Geol. 35, 983–998. https://doi.org/10.1111/jmg.12264.
Zarrinkoub, Mohammad Hossein, Pang, K.-N., Chung, S.-L., Khatib, M.M., Mohammadi, S.S., Chiu, H.-Y., Lee, H.-Y., 2012. Zircon U-Pb age and geochemical constraints on the origin of the Birjand ophiolite, Sistan suture zone, eastern Iran. Lithos 154, 392–405. https://doi.org/10.1016/j.lithos.2012.08.007.
Angiboust, S., Agard, P., Glodny, J., Omrani, J., Oncken, O., 2016. Zagros blueschists: Episodic underplating and long-lived cooling of a subduction zone. Earth and Planetary Science Letters 443, 48–58. https://doi.org/10.1016/j.epsl.2016.03.017.
Moghadam, H.S., Stern, R.J., Rahgoshay, M., 2010. The Dehshir ophiolite (central Iran): Geochemical constraints on the origin and evolution of the Inner Zagros ophiolite belt. Geological Society of America Bulletin 122, 1516–1547. https://doi.org/10.1130/B30066.1.
Paul, A., Hatzfeld, D., Kaviani, A., Tatar, M., Péquegnat, C., 2010. Seismic imaging of the lithospheric structure of the Zagros mountain belt (Iran). Geological Society, London, Special Publications 330, 5–18. https://doi.org/10.1144/SP330.2.
Masoodi, M., Yassaghi, A., Nogole Sadat, M.A.A., Neubauer, F., Bernroider, M., Friedl, G., Genser, J., Houshmandzadeh, A., 2013. Cimmerian evolution of the Central Iranian basement: Evidence from metamorphic units of the Kashmar-Kerman Tectonic Zone. Tectonophysics 588, 189–208. https://doi.org/10.1016/j.tecto.2012.12.012.

Michael Jentzer is a geologist from Sorbonne University in Paris, where he obtained his Ph.D. in 2021. Michael's background is in petrology, tectonics and geodynamics. He couples the interpretation of tectonics observations, magmatic data, metamorphic data radiochronological ages, and literature to constrain the geological evolution of orogen. During his Ph.D., he studied the structure and the evolution of the Sistan orogen in the Tethyan realm. His previous works include the study of metamorphic processes in the Betic cordillera.

Philippe Agard is Professor at Sorbonne Université in Paris, and fellow of Academia Europaea and Institut Universitaire de France. He received his doctoral degree from the Ecole Normale Superieure and UPMC. His field-based approach (e.g., in the Alps, Iran, Oman, China) combines metamorphic petrology and tectonics to investigate regional-scale geodynamics and processes like subduction, obduction or strain (de)localization. His present interests include unravelling the structure and rheology of the subduction plate interface, understanding the initiation of deep viscous coupling in subduction zones and the dynamics of ophiolite emplacement.

Guillaume Bonnet is a postdoctoral researcher at Sorbonne University, Paris (France). He graduated in Earth Sciences at École Normale Supérieure de Paris and Sorbonne University, and he obtained his PhD from Sorbonne University in 2018. He then worked as a postdoctoral fellow at the University of California, Santa Barbara (USA). He is interested in the geological record of subduction in exhumed high-pressure terranes (e.g. seamounts and hyperextended margins), that he addresses from the field and petrological perspectives. He has a particular interest in U-Th-Pb petrochronology of accessory minerals by LA-ICP-MS. Field areas include Iran (Sistan, Zagros), California (Franciscan complex) and the European Alps.

Patrick Monié Patrick Monié is a CNRS researcher at the Geosciences Department of the University of Montpellier in France. He is the head manager of the Montpellier Noble Gas Laboratory, an entity of the national network RéGEF (Réseau Géochimique et Expérimental Français) which provides access to equipment and expertise in the fields of geochemistry and isotope geochronology. He is a graduate of the University of Montpellier and has more than 40 years of experience in 40Ar/39Ar geochronology, combining step-heating and in situ laser probe techniques, allowing a better understanding of 40Ar/39Ar ages in different geological contexts, in particular that of high-pressure rocks. More recently, he has developed the dating of clay minerals from fault gouges and geothermal fields using a quartz tube encapsulation technique, in collaboration with various clay mineral specialists. At the same time, he developed the thermochronological (U-Th-Sm)/He method on apatite and zircon coupled with REE analyses on ICPMS. He is mainly interested in the application of these techniques to the problem of rock exhumation in mountain belts. Recently, he has participated in several projects focused on the alpine chain in different Mediterranean regions (Greece, Morocco, Spain, Pyrenees, Alps). P. Monié has collaborated with many geoscientists worldwide and has participated in the publication of numerous papers.

Marc Fournier is a Professor of geology at Sorbonne University, Paris, France. He holds a PhD in Earth Sciences from Ecole Normale Supérieure, Paris. His doctoral research involved field studies in Sakhalin and in Japan, and experimental modelling of back-arc extension in relation with the tectonics of Asia. His research interests include tectonics, plate kinematics and geodynamics. He is involved in field surveys in Oman, Yemen, Iran and Siberia, and in the Alps and Corsica. He has supervised several oceanographic cruise in the Gulf of Aden and the northwest Indian Ocean in order to investigate the structure of the conjugate continental margins, the kinematics of the Arabia-India-Somalia triple junction, and the evolution of the Arabia-India plate boundary. More recently, he has worked on fossil earthquakes in subduction zones from the example of the ophiolites of Alpine Corsica and the Siah Kuh subducted seamount in Iran.

Hubert Whitechurch is Emeritus Professor at the Earth and Environmental Institute of the University of Strasbourg (ITES-UMR 7063). His research focused on the structure and petrology of Tethyan ophiolite complexes (Syria, Turkey, Iran, Oman) and related arc or back-arc magmatism, in relation to the tectonic evolution of the Tethyan orogen. He carried out numerous marine missions (geophysics, diving and IODP drilling) on the oceanic ridges of the Atlantic, Indian and Lau Basin (Pacific) oceanic ridges and on the Kerguelen Plateau. He collaborated with many researchers through numerous cooperation programs which enabled the publication of a significant number of scientific papers and supervisions of PhD thesis on these research topics. He held many senior positions at the University.

Jafar Omrani is a head of laboratories of the Geological Survey of Iran. He holds a PhD in Earth Sciences from Sorbonne Université (Paris, France) in 2008. His doctoral research involved field studies in Zagros, and petrological investigations. His research interests include petrology, tectonics, resources and geodynamics.

Mohammad Hossein Zarrinkoub is a Professor of Geology in Birjand University (Iran). He holds a PhD in Earth Sciences from Tarbiat Moallem (kharazmi) University (Teheran, Iran) in 2000. His doctoral research involved petrology and geochemistry of ophiolitic complexes in south of Birjand (Iran). His research interests include petrology, geochemistry, radiochronological dating, resources and geodynamics.

Mohammad Mahdi Khatib is a Professor of Geology in Birjand University (Iran). He holds a PhD in Earth Sciences from Shahid Beheshti University (Teheran, Iran) in 1999. His doctoral research involved geometry of termination of strike-slip faults with the case of the Nehbandan fault zone (Iran). His research interests include tectonics, active faulting, paleostress determination and field studies.

Reza Kohansal obtained his degree in petrology Ph.D. (2016) at Shahid Beheshti University. His thesis was on geodynamic of the Sabzevar ophiolite, NE Iran. His main interests are on geology, geochemistry, petrology, petrogenesis, isotopic fields for paleogeography and geodynamic domains. He is working at the Geological Survey of Iran, having worked for 25 years in the Petrology Department for geological mapping. He has prepared maps with various scales in different zones of Iran. He is also a petrology supervisor and consultant for geological maps on the organization's projects.

Damien Do Couto is an assistant professor at the Institut des Sciences de la Terre de Paris (ISTeP), Sorbonne Université, France, since 2017. Graduated from the Université d'Orléans (France), he got his PhD degree in 2014 at Université Pierre & Marie Curie (former Sorbonne Université). He has focused on sedimentary and tectonic processes involved in sedimentary basins with the use of field (sedimentology, structural geology) and subsurface data (seismic reflection, drilling, gravimetry). He has also devoted work in analysing the response of sedimentary basins to geodynamic events, such as tectonics or eustatism, affecting the architecture and distribution of sedimentary rocks. More recently, he has developed a particular interest in the assessment of geo-energy resources at subsurface. He is an Associate Editor of the Journal of Marine and Petroleum Geology. He has been involved as author in numerous published papers, special publications and book chapters.

Camille Godbillot is a PhD candidate at Sorbonne Université (Paris, France). She holds a MSc in Lithospheric processes, Basin architecture and Paleoclimate reconstructions (Sorbonne Université, 2018). Throughout her different internship experiences, she specialized in the use of the geochemical composition of rocks as a means of inferring the conditions in which they formed. She has had the opportunity to experiment with multiple substrates, including metamorphic rocks and biogenic material. Her current PhD project aims at using the carbon and oxygen isotopic composition of Pleistocene calcite biominerals as recorders of past atmospheric CO2 concentrations.

Dia Ninkabou is a geologist from Sorbonne University in Paris, where he obtained his Ph.D. in 2021 (under a CIFRE Grant). Dia's background is in seismic stratigraphy and geodynamics. He couples the interpretation of regional seismic surveys, seismic tomography, and literature data to constrain the geological evolution of sedimentary basins. During his Ph.D., he studied the evolution of the Tethyan seaway in the Middle-East and Southern-Asia, with a focus on the Makran accretionary prism. His previous works include the study of Mediterranean and Brazilian passive margins on 2D and 3D seismic data. His research interests include seismic geomorphology, Tethyan paleogeography, and subduction dynamics.